

# Solar Fuel Synthesis via Photoelectrochemistry: Understanding and Controlling Interfaces

Author: Yumin He

Persistent link: <http://hdl.handle.net/2345/bc-ir:108570>

This work is posted on [eScholarship@BC](#),  
Boston College University Libraries.

---

Boston College Electronic Thesis or Dissertation, 2019

Copyright is held by the author, with all rights reserved, unless otherwise noted.

SOLAR FUEL SYNTHESIS VIA  
PHOTOELECTROCHEMISTRY:  
UNDERSTANDING AND  
CONTROLLING INTERFACES

Yumin He

A dissertation  
submitted to the Faculty of  
the department of Chemistry  
in partial fulfillment  
of the requirements for the degree of  
Doctor of Philosophy

Boston College  
Morrissey College of Arts and Sciences  
Graduate School

August, 2019



**SOLAR FUEL SYNTHESIS VIA PHOTOELECTROCHEMISTRY:  
UNDERSTANDING AND CONTROLLING INTERFACES**

Yumin He

Advisor: Dunwei Wang, Ph.D.

Solar fuel synthesis via photoelectrochemistry represents a promising strategy to achieve solar energy conversion and storage. The improvement of photoelectrochemical water splitting performance lies in choosing suitable photoelectrode materials, followed by strategic optimization of their properties. Among those properties, the interface between the semiconductors and electrolyte is of paramount importance, yet it is still not well understood. In my dissertation, I will mainly focus on understanding and controlling those interfaces, with two study platforms.

The first study platform is tantalum nitride ( $\text{Ta}_3\text{N}_5$ ), which is an attractive photoanode material with good optoelectronic properties. However, it suffers from low photovoltage despite of the high theoretical expectation and rapid performance decay when it is used for water oxidation. With the help of various characterization methods, it was found that water or hydroxyl group adsorption on the surface as well as the self-limited surface oxidation during water oxidation led to the positive shift of band edge positions and Fermi level, accompanied with increase of charge transfer resistance on the surface. In consequence, decrease of photovoltage and photocurrent was observed.

Two different strategies were developed. The first was to fully isolate  $\text{Ta}_3\text{N}_5$  from

water with the deposition of uniform protection layer through atomic layer deposition. The second strategy utilized the reaction between  $Ta_3N_5$  and co-catalyst instead of water, which led to the formation of a photo-induced interface that favored the desired chemistry instead of side reactions.

The second study platform is a Si buried junction protected by GaN. By tuning the loading amount of Pt nanoparticles on GaN surface, both the photocurrent density and photovoltage of the photocathode was improved. With detailed spectroscopic study, it was implied that both charge transfer kinetics and interfacial energetics could be influenced by the loading of Pt on the surface.

## TABLE OF CONTENTS

<b>Table of Contents .....</b>	<b>iii</b>
<b>Table of Abbreviations .....</b>	<b>vii</b>
<b>Acknowledgements .....</b>	<b>x</b>
<b>Chapter 1 Thin film photoelectrodes for solar water splitting .....</b>	<b>1</b>
<b>1.1 Demand for solar energy storage.....</b>	<b>1</b>
<b>1.2 Principles of photoelectrochemical water splitting .....</b>	<b>2</b>
<b>1.3 Definition of thin-film photoelectrodes .....</b>	<b>9</b>
<b>1.4 Thin film synthesis .....</b>	<b>11</b>
1.4.1 Physical vapor deposition (PVD) .....	12
1.4.2 Chemical deposition .....	13
1.4.3 (Photo)electrochemical deposition .....	16
<b>1.5 Common problems and corresponded strategies for representative thin-film semiconductors .....</b>	<b>18</b>
1.5.1 Poor light absorption.....	20
1.5.2 Bulk recombination .....	26
1.5.3 Surface recombination .....	32
1.5.4 Mismatch of energetics.....	38
1.5.5 Instability.....	43
1.5.6 Other issues.....	51

<b>1.6</b>	<b>Thin film protection layer .....</b>	<b>54</b>
1.6.1	Physical barrier protection layer .....	54
1.6.2	Kinetic protection layer .....	56
<b>1.7</b>	<b>Thin film catalysts.....</b>	<b>58</b>
1.7.1	The role of catalysts on photoelectrodes.....	59
1.7.2	The effect of catalysts on the light absorption.....	71
<b>1.8</b>	<b>Summary.....</b>	<b>76</b>
<b>1.9</b>	<b>Reference .....</b>	<b>78</b>
<b>Chapter 2</b>	<b>What limits the performance of tantalum nitride for solar water splitting? .....</b>	<b>85</b>
<b>2.1</b>	<b>Tantalum nitride photoanode as a prototypical platform for water oxidation ....</b>	<b>85</b>
<b>2.2</b>	<b>Materials and methods .....</b>	<b>88</b>
2.2.1	Material synthesis .....	88
2.2.2	PEC measurement.....	90
2.2.3	Material characterization .....	92
<b>2.3</b>	<b>Results and discussions.....</b>	<b>94</b>
2.3.1	Material characterization and PEC performance .....	94
2.3.2	X-ray core-level spectroscopy studies .....	96
2.3.3	Energetics evolution due to surface reaction .....	99
2.3.4	Recovery of the initial performance degradation by water oxidation catalysts.....	107
2.3.5	Strategies for improving tantalum nitride.....	108
<b>2.4</b>	<b>Summary.....</b>	<b>111</b>
<b>2.5</b>	<b>Reference .....</b>	<b>111</b>
<b>Chapter 3</b>	<b>Photo-induced performance enhancement of tantalum nitride for solar water oxidation .....</b>	<b>114</b>

<b>3.1</b>	<b>Tantalum nitride as a platform for interfacial study between semiconductors and catalysts</b> .....	<b>114</b>
<b>3.2</b>	<b>Materials and methods</b> .....	<b>116</b>
3.2.1	Material synthesis .....	116
3.2.2	EC measurement.....	118
3.2.3	Material characterization .....	119
<b>3.3</b>	<b>Results and discussions</b> .....	<b>120</b>
3.3.1	Material characterization and PEC performance .....	120
3.3.2	Explore possible hypotheses for the performance enhancement .....	123
3.3.3	Evolution of interfacial kinetics and energetics.....	129
3.3.4	Probe the photo-induced interface .....	133
3.3.5	Mechanism for the photo-induced interface .....	135
<b>3.4</b>	<b>Summary</b> .....	<b>137</b>
<b>3.5</b>	<b>Reference</b> .....	<b>137</b>
<b>Chapter 4</b>	<b>Dependence of interface energetics and kinetics on catalyst loading in a photoelectrochemical system</b> .....	<b>140</b>
<b>4.1</b>	<b>Interfacial study in a complex PEC system</b> .....	<b>140</b>
<b>4.2</b>	<b>Materials and methods</b> .....	<b>141</b>
4.2.1	Material synthesis .....	141
4.2.2	PEC measurement.....	143
4.2.3	Material characterization .....	144
<b>4.3</b>	<b>Results and discussions</b> .....	<b>145</b>
4.3.1	Controlling Pt loading amount and the corresponding PEC performance.....	145
4.3.2	Dependence of interface kinetics and energetics on Pt loading amount.....	149
4.3.3	Discussions of the photoelectrode electrolyte interface in a PEC system .....	153

4.3.4	Control experiments on Si photocathode without GaN .....	156
4.4	<b>Summary</b> .....	<b>158</b>
4.5	<b>Reference</b> .....	<b>159</b>
	<b>Publication list</b> .....	<b>161</b>

## TABLE OF ABBREVIATIONS

**ALD:** atomic layer deposition

**APCVD:** atmospheric pressure chemical vapor deposition

**CBD:** chemical bath deposition

**CVD:** chemical vapor deposition

**DBR:** distributed Bragg reflector

**DFT:** density functional theory

**DHC:** dinuclear heterogeneous catalyst

**DWE:** dual-working-electrode

**E<sub>CB</sub>:** conduction band minimum

**ED:** electrochemical deposition

**E<sub>F</sub>:** Fermi level

**E<sub>F,n</sub>:** quasi Fermi level of electrons

**E<sub>F,p</sub>:** quasi Fermi level of holes

**E<sub>g</sub>:** band gap

**E<sub>VB</sub>:** valence band maximum

**FF:** fill factor

**FRA:** frequency response analyzer

**HER:** hydrogen evolution reaction

**IMPS:** intensity modulated photocurrent spectroscopy

**$J_{ph}$ :** photocurrent density

**$K_{rec}$ :** charge recombination rate constant

**$K_{tran}$ :** charge transfer rate constant

**$L_{min}$ :** minority carrier diffusion length

**LSV:** linear sweep voltammetry

**MOCVD:** metal-organic chemical vapor deposition

**$N_d$ :** donor density

**NT:** nanotube

**NW:** nanowire

**OCP:** open circuit potential

**OER:** oxygen evolution reaction

**PAA:** porous anodic alumina

**PAMBE:** plasma-assisted molecular beam epitaxy

**PCET:** proton-coupled electron transfer

**PEC:** photoelectrochemistry

**PECVD:** plasma-enhanced chemical vapor deposition

**PED:** photoelectrochemical deposition

**PEIS:** photoelectrochemical impedance spectroscopy

**$P_{in}$ :** input light intensity

**PS-EC-AFM:** potential-sensing electrochemical atomic force microscopy

**PVD:** Physical vapor deposition

**RBS:** Rutherford backscattering spectrometry

**RHE:** reversible hydrogen electrode

**SAC:** single-atom catalyst

**SCE:** saturated calomel electrode

**SCLI:** semiconductor/liquid interface

**SEM:** scanning electron microscopy

**SS:** surface state

**STH:** solar to hydrogen efficiency

**TAS:** transient absorption spectroscopy

**TE:** charge transfer efficiency

**TEM:** transmission electron microscopy

**TEY:** total electron yield

**TRL:** technology readiness levels

**UPS:** ultraviolet photoelectron spectroscopy

**USP:** ultrasonic spray pyrolysis

**UV-Vis:** ultraviolet-visible absorption spectra

$V_{bb}$ : potential drop in the band bending

$V_{fb}$ : flat band potential

$V_{on}$ : turn-on potential

$V_{ph}$ : photovoltage

$W_{sc}$ : width of space charge region

**XAS:** X-ray absorption spectroscopy

**XPS:** X-ray photoelectron spectroscopy

**XRD:** X-ray diffraction patterns

## ACKNOWLEDGEMENTS

First of all, I would like to thank my advisor Prof. Dunwei Wang, for his continuous guidance during my graduate study. By attending his courses, I learnt the fundamental knowledge of (photo)electrochemistry and solid-state chemistry, which serve as the cornerstones for my research projects. With the frequent discussions of experimental results between us, he was always able to consolidate our goals and paved the way to fruitful outcomes. When the frustration came, he was there to offer the motivation. He is critical but encouraging. The most important thing I learnt from him, however, is the philosophy for the scientific research: knowing how to identify the critical questions within the context and find the ways to answer them. I will still hold this principle in my future career.

I also would like to acknowledge my committee: Prof. Chia-Kuang (Frank) Tsung, Prof. Udayan Mohanty and Prof. Matthias Waagele. Prof. Tsung gave me the opportunity to join the Chemistry Department at Boston College. His *Physical Chemistry* class in the first semester started my graduate study. He was also generous in helping me when I was looking for the postdoc positions. I appreciated Prof. Mohanty for showing me his broad knowledge in the *Solid State Chemistry* and *Physical Chemistry* class. Prof. Tsung and Prof. Mohanty were my oral exam committee as well, offering me helpful

advice for my PhD study. Prof. Waegele really impressed me for his insightful understandings in the surface chemistry, which benefit me tremendously.

Next, I would like to thank my lab mates in the past five years. Dr. Xiahui Yao was my first mentor when I joined the group. He taught me a lot about the instrumentation as well as the knowledge of the battery field. Dr. Chun Du was my second mentor, who brought me into the field of solar fuels. Her patience for explanation as well as optimism in doing experiments made me feel much easier when I switched my research direction. I also want to thank Dr. James Thorne, Prof. Peiyan Ma, Dr. Shasha Zhu, Dr. Qingmei Cheng, Dr. Wei Li, Prof. Wenjun Fa, Dr. Rong Chen, Mengdi Liu, Da He, Dr. Qi Dong, Yanyan Zhao, Chaochao Lang, Jeremy Espano, Xizi Zhang, Erik Liu and Tianyue Gao for working together on different projects. In addition, I really appreciate Prof. Jin Xie, Prof. Pengcheng Dai, Prof. Ji-Wook Jang, Prof. Song Li, Prof. Weiqiang Fan, Prof. Hongye Bai, Prof. Bingqing Zhang, Jingru Luo, Haochuan Zhang and Xin Ba for insightful discussions.

I also want to acknowledge my collaborators: Dr. Jinghua Guo and Dr. Chenghao Wu at Advanced Light Source; Prof. Thomas W. Hamann at Michigan State University; Prof. Zetian Mi, Srinivas Vanka and Dr. Yongjie Wang at University of Michigan; Prof. Pratap M. Rao, Binod Giri and Prof. Ronald Grimm at Worcester Polytechnic Institute; Dr. Francesca Maria Toma and Dr. Guosong Zeng at Lawrence Berkeley National Laboratory; Prof. Craig L. Hill and Daniel L. Collins-Wildman at Emory University; Prof. Dong Ha Kim and Dr. Yoon Hee Jang at Ewha Womans University; Dr. Todd Deutsch, Dr. James Young and Rachel Mow at National Renewable Energy Laboratory; Prof. Kenneth Burch and Erin Sutton at Boston College.

Additionally, I want to acknowledge all the administrative and technical staffs in the Chemistry Department, Physics Department and the Integrated Sciences Cleanroom and Nanofabrication Facility at Boston College. Particularly, I want to thank Stephen Shepard for his responsible and patient support.

Last, I want to acknowledge my parents for their understanding and support for my graduate study abroad. Most importantly, I would like to thank Jingru Luo for her concern and love, for sharing the wonderful time and going through the difficulties together.

## CHAPTER 1 THIN FILM PHOTOELECTRODES FOR SOLAR WATER SPLITTING

### 1.1 DEMAND FOR SOLAR ENERGY STORAGE

Since the first Industrial Revolution, the development of human society has been highly dependent on fossil fuels. However, as the industry scaled up, the side effects of consuming fossil fuels emerged, such as the global warming. In order to achieve environment-friendly and sustainable development, it becomes critical to utilize the renewable energy sources. As the most abundant renewable energy sources, solar radiation produced annual energy of approximately 3,850,000 EJ, which is almost four orders of magnitude higher than the yearly energy consumption of human beings. However, the utilization of solar energy in terawatt scale still remains challenging due to the intermittent nature of sunlight, leading to the urgent demand for efficient and cost-effective energy storage devices.<sup>1</sup> For example, due to the cost of lithium-ion batteries has fallen rapidly, electric grid combining station batteries and photovoltaics shows its practical feasibility as one of the energy storage solutions.

Among various approaches, technologies that can utilize solar energy to drive thermodynamically uphill reactions are attractive, since they provide a simple pathway to achieve both solar energy conversion and storage simultaneously.<sup>2</sup> Water splitting to produce hydrogen gas and carbon dioxide reduction to produce hydrocarbons are

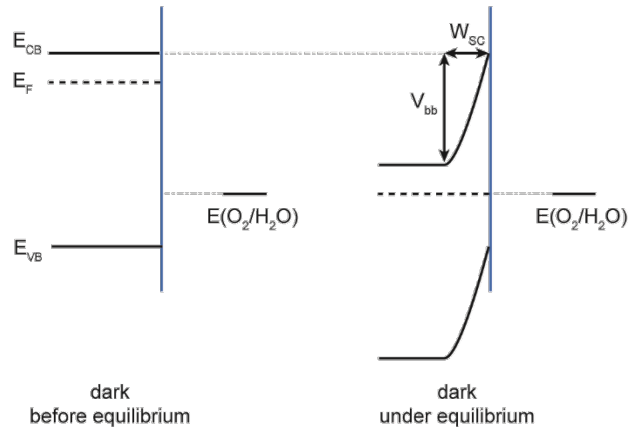
representative ones. The resultant products, namely solar fuels, can be redistributed to fit in the infrastructure of energy consumption, such as direct usage as fuels or subjected to industrial synthesis. The approach is usually named artificial photosynthesis, mimicking the natural photosynthesis in green plants. Photoelectrochemical (PEC) water splitting is one of the most promising strategies to produce  $H_2$  as solar fuels based on a recent techno-economic analysis. First reported in 1968 by Boddy and popularized in 1972 by Honda and Fujishima, such an approach has been studied by researchers since then, creating a broad field.<sup>3,4</sup> In the past a few decades, numerous efforts have been devoted to make the PEC route practical, along with discovery of exciting scientific knowledge. In the following section, some basic principles of PEC water splitting will be introduced. Furthermore, recent progress of using thin-film photoelectrodes in PEC water splitting will be discussed in details.

## **1.2 PRINCIPLES OF PHOTOELECTROCHEMICAL WATER SPLITTING**

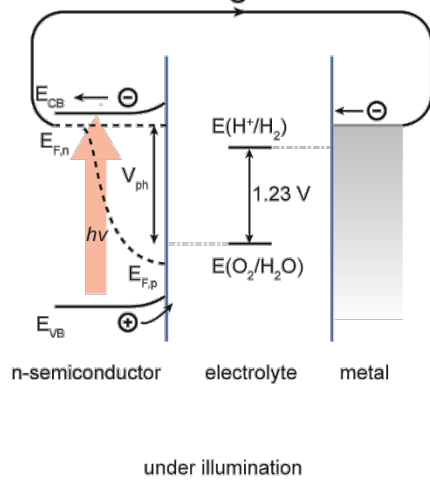
The basic principles of PEC water splitting are based on the behaviors of semiconductor-liquid junctions.<sup>5</sup> The process can be described in Figure 1.1, taking a n-type semiconductor as the example. When the semiconductor is immersed into the electrolyte without illumination, the equilibrium between the semiconductor and redox species in the electrolyte (e.g.,  $O_2/H_2O$ ) leads to the depletion of majority carriers in the semiconductor near the surface and results in the band bending (Figure 1.1 (a)), in which the potential drop is defined as  $V_{bb}$ . Such a region is called space charge region and its width is defined as  $W_{sc}$ . In the space charge region, there are positive charges left behind, while

excess of negative charges is accumulated in the Helmholtz layer in the electrolyte side near the semiconductor surface. As a result, an electric field is created in the space charge region, which can help to separate the photo-generated charges under illumination. Particularly, the minority charge carriers (e.g., holes for n-type semiconductors) will transport to the semiconductor surface under the electric field to complete the desired reaction (e.g., water oxidation).

(a)



(b)



(c)

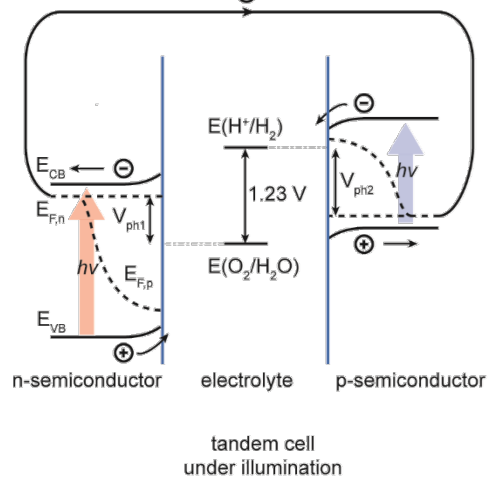


**Figure 1.1** (a) Schematic shows the band diagram of a n-type semiconductor before and after equilibrium with the water oxidation potential under dark. (b) Schematic shows the band diagram of a n-type semiconductor connected with

a metal counter electrode under illumination for overall water splitting.  $E_{CB}$ : conduction band minimum,  $E_{VB}$ : valence band minimum,  $E_{F,n}$ : quasi-Fermi level of electrons,  $E_{F,p}$ : quasi-Fermi level of holes. (c) Schematic shows the band diagram of a n-type semiconductor connected with p-type semiconductor in tandem configuration under illumination for overall water splitting.  $V_{ph1}$ : photovoltage from n-type photoanode,  $V_{ph2}$ : photovoltage from p-type photocathode. The overall photovoltage  $V_{ph}=V_{ph1}+V_{ph2}$ .

To enable unassisted water splitting through the PEC approach, the photovoltage ( $V_{ph}$ ) generated from the semiconductor/liquid junction needs to satisfy the thermodynamic energy of splitting water molecules to hydrogen and oxygen molecules ( $\Delta G^0 = 237.1$  kJ/mol, corresponding to  $\Delta E^0 = 1.23$  V per electron) and additional kinetic barriers for the reaction.<sup>2</sup> The value of  $V_{ph}$  depends on the difference between the initial Fermi level ( $E_F$ ) and the equilibrium potential of redox species, as shown in Figure 1.1(b). However, it is difficult to meet the energy requirement using a single semiconductor. Typically, multiple light absorbers will be connected together, as shown in Figure 1.1(c), so that wider range of solar spectrum can be utilized and the  $V_{ph}$ 's can be added up. When the circuit is closed under illumination, the hydrogen fuels are produced. The solar to hydrogen efficiency (STH) is defined as:

$$STH = \frac{J_{ph} \times 1.23 V}{P_{in}} \quad (1.1)$$

In the equation (1.1),  $J_{ph}$  is the photocurrent density out of the PEC device, measuring the rate of photo-generated holes consumed by the water oxidation reaction.  $P_{in}$  is the light intensity on the PEC device. Since  $P_{in}$  is usually a constant, the value of  $J_{ph}$  determines the value of STH. For a certain semiconductor, its ability to absorb light in certain wavelength is well defined by the absorption coefficients ( $\alpha$ ). Theoretically, the photogenerated charges across the semiconductor/liquid junction come from two parts. One is generated within the space charge region, which can be separated and transported

efficiently. Another is generated in the bulk of semiconductor, and the farthest position where the photogenerated charges can diffuse into the space charge region for efficient separation is determined by the minority carrier diffusion length ( $L_{min}$ ). Since the width of space charge layer depends on the degree of band bending, which is affected by the applied potential, the photocurrent density under monochromatic illumination can be calculated using Gärtner equation<sup>6</sup>:

$$J_G = I_0 \left[ 1 - \frac{\exp(-\alpha W_{sc})}{1 + \alpha L_{min}} \right] \quad (1.2)$$

$$W_{sc} = \sqrt{\frac{2\epsilon\epsilon_0 V_{bb}}{qN_d}} = \sqrt{\frac{2\epsilon\epsilon_0 (V - V_{fb})}{qN_d}} \quad (1.3)$$

In equation (1.2),  $J_G$  is the photocurrent density calculated from the Gärtner equation.  $I_0$  is the photon flux illuminated on the semiconductor. Equation (1.3) describes the dependence of  $W_{sc}$  on the  $V_{bb}$  as well as other properties of a given semiconductor.  $N_d$  is the donor density,  $\epsilon$  is the dielectric constant of the semiconductor and  $\epsilon_0$  is the vacuum permittivity, which is a constant. In the case when the applied potential only shifts the Fermi level (so-called band edge pinning conditions),  $V_{bb}$  equals  $V - V_{fb}$ , in which  $V_{fb}$  is the flat-band potential.  $V_{fb}$  is defined as the potential where band bending is zero, which is the Fermi level in Figure 1.1(a) before the equilibrium. The relationship between photocurrent density and applied potential based on Gärtner equation is shown as the dotted line in Figure 1.2.

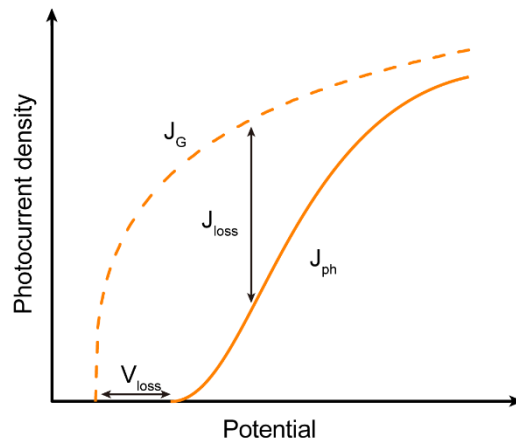


**Figure 1.2** The curves of photocurrent density versus applied potential for a n-type semiconductor in the electrolyte under illumination. The dotted line is calculated based on equation (1.2), while the solid line is calculated based on equation (1.4).

However, what is usually observed under the experimental conditions is different from the predicted photocurrent density using Gärtner equation as shown in Figure 1.2. That is because the key assumptions required for Gärtner equation are (1) all photogenerated holes in the bulk and within the space charge region are transported to the surface without loss; (2) all surface-reaching holes are transferred rapidly across the interface. This means there is no charge recombination in the space charge region and at the semiconductor/electrolyte interface. But such an assumption is difficult to reach for the water splitting reactions. The limitations can be considered from two aspects. In the kinetics perspective, water reduction and oxidation feature sluggish reaction kinetics, affecting the charge transfer rate constant ( $k_{\text{tran}}$ ) across the semiconductor/electrolyte interface.<sup>7</sup> From the energetics perspective, surface states (e.g., surface adsorbed species, dangling bonds and electronic states) at the semiconductor/electrolyte interface serve as the recombination centers for electrons and holes.<sup>8</sup> Due to the slow charge transfer rate constant across the interface, holes accumulate at the surface, altering the potential drop

across the Helmholtz layer.<sup>7</sup> At the same applied potential, instead of the band edge pinning conditions where the applied potential only leads to the change of band bending, such an effect (defined as the Fermi level pinning) leads to the decrease of band bending (thus smaller  $V_{bb}$ ). Weaker band bending leads to worse charge separation ability, resulting in higher surface charge recombination rate constant ( $k_{rec}$ ). The effect of surface charge recombination and Fermi level pinning is described in Figure 1.3. As a consequence, the photocurrent density based on Gärtner equation ( $J_G$ ) can be modified as:<sup>7</sup>

$$J_{ph} = J_G \frac{k_{tran}}{k_{rec} + k_{tran}} \quad (1.4)$$

As shown in Figure 1.2, significant photovoltage and photocurrent loss can be observed due to the slow minority charge carrier transfer and enhanced surface charge recombination as well as Fermi level pinning.

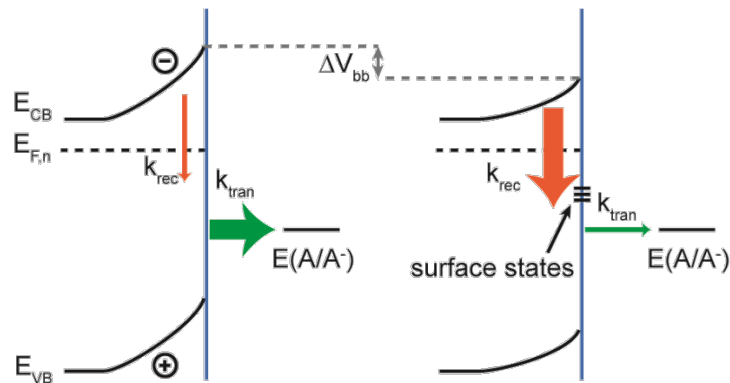


**Figure 1.3** The schematic shows the charge transfer and recombination in a n-type semiconductor with the redox species ( $A/A^{\cdot}$ ) in the electrolyte under illumination. The size of arrows represents the qualitative value of  $k_{tran}$  and  $k_{rec}$ . When  $k_{tran}$  decreases and surface states exist (from the left to the right), surface recombination becomes severe and the band bending decreases ( $\Delta V_{bb}$ ) even at the same applied potential.

Based on aforementioned discussions, the key factors govern the properties and performance of a semiconductor-based water splitting system can be summarized as follows:

- (1) Light absorption abilities of the semiconductor. The band gap ( $E_g$ ) determines how broad is the absorption spectrum, and the light absorption coefficient determines how efficient is the light absorption at each wavelength. Overall, it provides the upper limit of photocurrent density one can obtain from a semiconductor with a certain thickness.
- (2) Electronic properties of the semiconductor. The band edge positions and the Fermi level determine the photovoltage output, which is the thermodynamic requirement and the driving force. Other electronic properties are also important such as the minority diffusion length and the width of space charge region, limiting the amount of minority carriers reaching the surface.
- (3) Interfacial properties between the semiconductor and electrolyte. How fast the charge can be transferred to complete the desired chemistry and how significant is the surface charge recombination set additional limits for the photocurrent density. Whether there are surface states at the interface impacts the potential distribution in the space charge region and Helmholtz layer, further affecting the surface energetics.

Those key factors provide guidelines for choosing the suitable materials and optimization directions of the whole water splitting systems. In the following sections, thin-film materials will be used as the study platforms to illustrate the PEC water splitting systems in details.

### 1.3 DEFINITION OF THIN-FILM PHOTOELECTRODES

The dilemma between efficiencies and costs is a critical challenge that has prevented solar fuels from being developed into a practical technology for large-scale solar energy harvesting and storage. That is, highly efficient or low-cost solar fuel synthesis has been demonstrated separately but not together. At the heart of the dilemma are issues connected to materials which can be used to harvest solar energy and carry out the desired chemical reactions. Such an understanding has underpinned the significant research efforts in materials innovations for solar fuel synthesis. Indeed, a wide spectrum of materials in terms of compositions, morphologies and structures, among other factors, has been proposed and tested, with varying degrees of successes in solving the cost-efficiency dilemma. Thin-film materials whose thicknesses are below a few microns, mostly in the tens of nanometers range, are unique for a number of reasons. First, they represent a form factor that can be readily studied for materials' fundamental properties, especially charge behaviors such as excitation, separation, transport and transfer. For instance, most thin films can be readily fashioned into an electrode for the assessment of the electrochemical and photoelectrochemical behaviors, which report on the charge properties of the materials. While better performance may be measured on other morphologies (*vide infra*), particularly those with nanometer scale features, thin films are often much simpler to study for insights that can guide future efforts aimed at optimizing structures for further improvements. In other words, thin film materials represent a good model platform for fundamental understanding of solar fuel materials.

Second, a rich knowledge base on thin film materials has been generated by decades of intense research on semiconductors. A great deal has been learned about how

to synthesize them; a battery of experimental techniques has been developed to readily study them; strategies on how to combine different layers of components with complementary functionalities into a single material have been proposed and proven highly effective. The last point is especially valuable for the purpose of solar fuel synthesis because it is widely recognized that a single composition is unlikely to meet all the needs, including light absorption, charge separation, catalysis and passivation. The best hope to realize these functionalities is to construct an integrated system that includes multiple components, each optimized for one or more specific purposes. For example, semiconductors with suitable bandgaps and electronic properties may be used to maximize light absorption and charge separation; heterogeneous and/or molecular catalysts can be introduced on top of the semiconducting light absorber for fast and highly specific charge transfer; additional protection may be necessary for durability. While such a strategy may be implemented in a variety of forms, thin films have been proven the most straightforward thanks to the rich knowledge base on their syntheses. More important, what is learned on thin film materials may be readily transferred for the construction of more complex structures for optimum performance such as various nanostructures.

In the following sections, each component of a thin-film photoelectrode will be discussed, including the light absorbers (which are limited to semiconductors for ease of discussions), protection layers and catalyst layers. A general introduction of the synthetic methods of thin films will be discussed first, and then move on to discussions of light absorbers based on their common problems and corresponded strategies. Corrosion protection strategies are next discussed, followed by thin film catalyst layers.

## 1.4 THIN FILM SYNTHESIS

A variety of synthetic methods have been developed to produce thin films. Generally, they may be categorized into three major groups based on the nature of the reactions utilized, namely physical vapor deposition, chemical deposition and electrochemical deposition (Figure 1.4). The principles of each method are presented below with selected examples. It is noted that in a complex thin film, which may include multiple layers, each layer may be prepared by a different method. Such a consideration is particularly relevant for the topic discussed here as successful solar fuel reactions often dictate the combination of materials with distinctly different, yet complementary, properties (Figure 1.4). The flexibility of using different methods to synthesize different components holds great promise for realizing the desired functionalities.

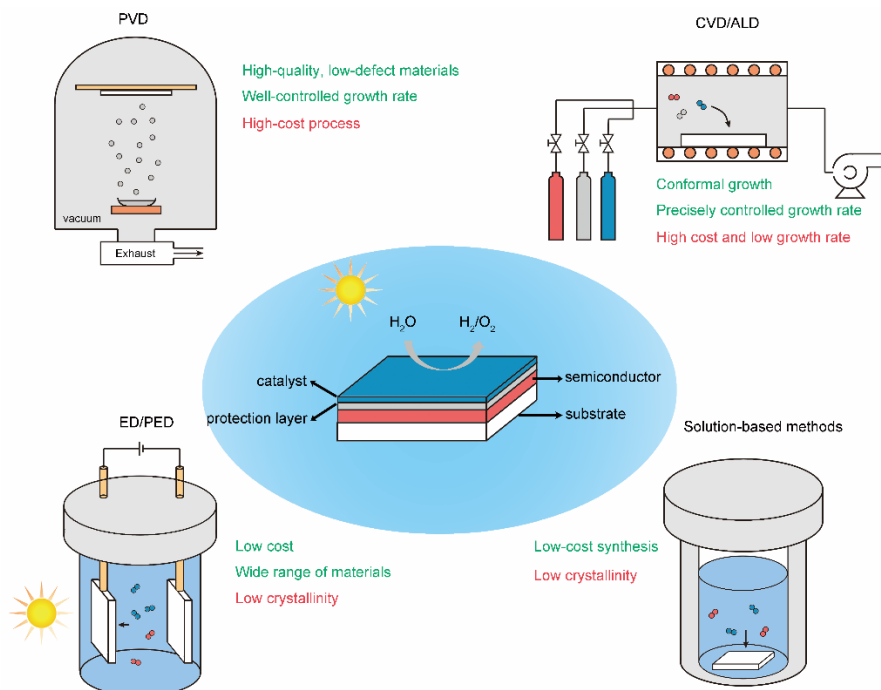


**Figure 1.4** Schematics showing the common deposition methods for thin-film materials. The advantages and disadvantages of each method are shown in green and red texts, respectively.

### 1.4.1 Physical vapor deposition (PVD)

Physical vapor deposition refers to synthesis methods which vaporize target materials with physical means for subsequent deposition on the receiving substrates. A key distinguishing feature of PVD is the lack of chemical reactions. The methods to introduce target materials include plasma (sputtering, molecular beam epitaxy), electron beam (e-beam evaporation, molecular beam epitaxy), heat (thermal evaporation, molecular beam epitaxy) and laser (pulse laser deposition). In comparison with other thin film growth techniques, PVD features advantages such as versatile, reproducible and relatively easy to implement. The resulting materials are often of the highest quality in terms of purity and quality. For these reasons, PVD has been widely used to synthesize nearly every type of semiconductors reported to date. Just within the context of solar fuel synthesis, a large number of examples exist, where high performance photoelectrodes were prepared by PVD. For instance, Cu(InGa)Se<sub>2</sub> photocathode was obtained by the co-evaporation of In, Ga, Cu and Se targets onto Mo-coated glass substrates.<sup>9</sup> Materials with similar compositions have also been achieved by molecular beam epitaxy (MBE), with the substrate temperature first increased to 300 °C and then fixed at 550 °C.<sup>10</sup> Ta<sub>3</sub>N<sub>5</sub> has been reported to be synthesized by sputtering TaO<sub>x</sub> thin-films onto Ta metal substrates, followed by a facile nitridation process.<sup>11</sup> InGaN nanowires have been reported to grow on Si substrates using In/Ga metal and N<sub>2</sub> plasma at 600 °C using MBE.<sup>12</sup> In addition to photoactive materials as noted above, PVD has been used for the deposition of protective layers and/or catalysts. For example, TiO<sub>2</sub> protection layer can be deposited on Si surface by sputtering Ti target in a reactive oxygen atmosphere.<sup>13</sup> To minimize surface oxidation of Si during the process, a thin layer of Ti (5 nm) was first

sputtered to protect the surface. Metal layers (AuGe/Ni/Au and Pt) was e-beam evaporated on the surface of GaAs photocathode to protect it from photocorrosion.<sup>14</sup> Of these examples, the most broadly implemented may be Pt deposition via sputtering as an effective catalyst to improve the hydrogen evolution reaction (HER) performance of photocathodes.<sup>15</sup> The limitation of PVD is mainly the high cost due to high-vacuum chamber assemblies, which introduce extra fabrication cost compared with solution-based methods.

### 1.4.2 Chemical deposition

The most obvious difference between chemical deposition and PVD is the involvement of chemical precursors and/or chemical reactions during the deposition. Depending on the media within which the deposition is carried out, chemical deposition may be divided into subcategories. When the deposition is mainly performed via vapor-phase processes, we have chemical vapor deposition (CVD) or atomic layer deposition (ALD). For the ease of precursor delivery, volatile materials such as organometallic compounds are most often used as the precursors. The key difference between CVD and ALD lies in that the latter typically features self-limiting surface chemical reactions. CVD has been widely employed to synthesize thin film semiconductors, including metal oxides. For example, Kay *et al.* reported the synthesis of cauliflower-type hematite ( $\alpha$ -Fe<sub>2</sub>O<sub>3</sub>) thin films from Fe(CO)<sub>5</sub> and tetraethoxysilane (TEOS) on a FTO-coated glass substrate at 415 °C.<sup>16</sup> GaAs-based photoelectrodes have been synthesized by the metal-organic CVD (MOCVD) method at 800 °C, using trimethyl gallium, trimethyl aluminium and arsine (AsH<sub>3</sub>) as the precursors for Ga, Al and As, respectively.<sup>14, 17, 18</sup> Amorphous silicon (a-

Si) was deposited via a plasma-enhanced CVD (PECVD) method, in which silane ( $\text{SiH}_4$ ) was used as the precursor for silicon, and phosphine ( $\text{PH}_3$ ) and trimethyl boron ( $\text{B}(\text{CH}_3)_3$ ) were used for n- and p-type doping, respectively.<sup>19</sup>

Different from CVD, the self-limiting surface reaction nature of ALD gives rise to the ability to precisely control the growth thickness by a layer-by-layer deposition process. Consequently, it has been widely used to deposit thin-film semiconductors, protective layers and catalysts. For example, thin-film hematite has been deposited on high-aspect ratio substrates such as  $\text{TiSi}_2$  nanonets and Si nanowires with  $\text{Fe}(\text{O}^t\text{Bu})_6$  and  $\text{H}_2\text{O}$  as the Fe and O precursors, respectively.<sup>20, 21</sup> ALD-grown  $\text{TiO}_2$  has been explored as an effective protection layer on both photoanode and photocathode materials. It was found that the crystallinity of  $\text{TiO}_2$  is sensitive to many factors, including the type of precursors used. When titanium isopropoxide ( $\text{Ti}(\text{i-PrO})_4$ ) was used as the precursor, crystalline  $\text{TiO}_2$  was deposited at 275 °C onto  $\text{Cu}_2\text{O}$ , which served as a protection layer.<sup>22</sup> When tetrakis(dimethylamido)-titanium (TDMAT) was used as the precursor, amorphous  $\text{TiO}_2$  was deposited at 150 °C onto  $\text{BiVO}_4$  that also served as a protection layer.<sup>23</sup> ALD was also used to deposit thin films of catalysts. For example, NiO has been deposited on the surface of  $\text{BiVO}_4$  at 260 °C using bis(2,2,6,6-tetramethylheptane-3,5-dionato)nickel(II) ( $\text{Ni}(\text{thd})_2$ ) and  $\text{H}_2\text{O}$  as the precursors.<sup>24</sup> Interestingly, the as-grown NiO is also a p-type semiconductor. In addition to serving as an oxygen evolution reaction (OER) catalyst, it was discovered to further improve the performance of the system by forming a p-n junction with  $\text{BiVO}_4$ .

An advantage offered by CVD and ALD is the control over the purity of the target materials, thanks to the gas-phase nature of the precursor delivery. The low pressures at

which the deposition is carried out also ensure reasonably long mean free path of the precursor species in the reactor, suggesting that most film growth is not diffusion limited. This feature, however, makes the implementation relatively difficult, increasing the processing cost. Such a challenge may be addressed by relaxing the requirements for vacuum and carrying out the deposition either directly in a solution or in ambient air. The most popularly encountered examples include chemical bath deposition (CBD) and electrochemical deposition. Due to the broad implementations of electrochemical deposition, this method will be introduced as a subcategory next.

Various metal oxides, such as hematite,  $\text{WO}_3$  and  $\text{BiVO}_4$ , have been successfully synthesized by solution methods. For instance, nanostructured hematite thin films were synthesized by immersing a FTO glass into the mixture of  $\text{FeCl}_3$  and  $\text{NaNO}_3$  at  $100\text{ }^\circ\text{C}$ , followed by post-annealing in air.<sup>25</sup>  $\text{WO}_3$  thin films were prepared by first mixing the tungsten precursor with  $\text{H}_2\text{O}_2$ , 2-propanol and poly(ethylene glycol) and then drop-casting the solution onto a FTO glass substrate, followed by post-annealing in air to convert the film to  $\text{WO}_3$ .<sup>26</sup> Non-oxide semiconductors have been synthesized by solution-based methods, as well. For example,  $\text{Cu}_2\text{ZnSnS}_4$  was obtained by spin coating a homogenous hybrid ink containing thiourea,  $\text{Sn}^{2+}$ ,  $\text{Cu}^{2+}$  and Zn nanoparticles in 2-methoxyethanol onto molybdenum-covered glass substrates, followed by air drying (at  $200\text{ }^\circ\text{C}$ ) and sulfurization processes in  $\text{H}_2\text{S}$  atmosphere at  $560\text{ }^\circ\text{C}$ .<sup>27</sup> Note that a post-growth annealing treatment is involved in all examples listed here either to achieve the desired crystallinity or compositions because the synthesis conditions are often not sufficient for the desired materials in a single step, as limited by the solution nature of the precursors or the reactions or both.

In addition to semiconductors, protective layers and catalysts have been synthesized by solution-based methods. For example, Liu *et al.* reported the synthesis of a ferrihydrite protection layer on the surface of Ta<sub>3</sub>N<sub>5</sub> by immersing the substrates into a solution containing Fe(NO<sub>3</sub>)<sub>3</sub> and NaNO<sub>3</sub> at 100 °C.<sup>28</sup> Further decoration of Co<sub>3</sub>O<sub>4</sub> nanoparticles as OER catalysts was achieved hydrothermally by sealing the substrate with a precursor solution containing Co(CH<sub>3</sub>COO)<sub>2</sub> and NH<sub>4</sub>OH in an autoclave at 120 °C. Nickel-iron layered double hydroxide (NiFe-LDH) has been deposited on the surface of Ta<sub>3</sub>N<sub>5</sub> nanorods as a protection layer via a two-step hydrothermal reaction at 120 °C and 150 °C, respectively.<sup>29</sup> Thin films (5-10 nm) of Ni:FeOOH were deposited on various semiconductors (e.g., WO<sub>3</sub>/BiVO<sub>4</sub>, hematite, TiO<sub>2</sub> and Si) via a hydrothermal method at 100 °C to serve as an efficient water oxidation catalyst.<sup>30</sup>

### 1.4.3 (Photo)electrochemical deposition

The uniqueness of electrochemical deposition (ED) and photoelectrochemical deposition (PED) method lies in the usage of an external bias and sometimes illumination. On the one hand, it introduced more parameters, such as potential and current, to tune the composition, morphology and the corresponding performance of the deposited materials. On the other hand, the utilization of light to facilitate the deposition in the case photoelectrochemical processes not only reduces energy input for the synthesis, it also improves the interface between the target materials (e.g., catalysts) and the receiving substrates for better charge transfer. Another benefit is the selectivity – catalysts will be deposited only where they are needed (e.g., where the photogenerated holes are for OER reaction). The detailed mechanisms and examples of electrochemically deposited

semiconductors and catalysts have been reviewed recently.<sup>31</sup> For instance, nickel molybdenum (Ni-Mo) catalyst has been electrodeposited under dark or light illumination on various photocathode materials to serve as efficient HER catalysts. Digdaya *et al.* reported an amorphous SiC photocathode coated with Ni-Mo, which was potentiostatically deposited at -1.0 V vs. Ag/AgCl under standard AM 1.5 illumination from mixed solution of nickel sulfate, boric acid and sodium molybdate.<sup>32</sup> Similar deposition was also reported by Pan *et al.* on Cu<sub>2</sub>O photocathodes, but with constant current of -1.5 mA/cm<sup>2</sup> during deposition and nickel sulfamate as the nickel precursor.<sup>33</sup> In addition, various OER catalysts (e.g., transition metal (oxy)hydroxide) have been widely used on photoanode materials via ED/PED. For example, Liu *et al.* reported amorphous cobalt-iron hydroxide nanosheet catalysts with efficient OER activities in alkaline environment.<sup>34</sup> Such catalysts were deposited on BiVO<sub>4</sub> photoanodes at a constant potential of -1.42 V vs. Hg/Hg<sub>2</sub>SO<sub>4</sub> from the electrolyte containing equivalent amount of Co(NO<sub>3</sub>)<sub>2</sub> and Fe(NO<sub>3</sub>)<sub>2</sub>. Kim *et al.* showed that FeOOH and NiOOH deposited on the BiVO<sub>4</sub> photoanode sequentially by PED method improved its turn-on potential ( $V_{on}$ ) and photocurrent density ( $J_{ph}$ ) at the same time.<sup>35</sup> A wide spectrum of semiconducting materials and catalysts has been successfully prepared by (photo)electrochemical methods, making the technique a facile tool for the synthesis of nearly all photoactive materials for solar fuel applications.

## 1.5 COMMON PROBLEMS AND CORRESPONDED STRATEGIES FOR REPRESENTATIVE THIN-FILM SEMICONDUCTORS

As one of the most exciting research areas during the past decade, solar fuel synthesis has attracted enormous attention. As such, nearly all photoactive materials have been exploited for the purpose of solar fuel synthesis. Comprehensive reviews on such efforts can be found here.<sup>36-38</sup> In this section, the emphasis is placed on the common issues that limit the performance of a given material for solar-to-chemical energy conversion. Representative strategies in addressing these issues on prototypical materials are presented. Since there is rarely a semiconductor that can meet all the common issues, most of study for photoelectrode materials have focused on solving one or multiple limitations of a certain material with other promising properties. Organizing the content by undesired properties and corresponded solving strategies can clearly show the research efforts on developing thin-film materials for solar fuel synthesis.

As shown in Figure 1.5, solar fuel synthesis on a solid-state material involves several key steps, including charge excitation, separation, transport and transfer. Of them, charge excitation is ensured by the optoelectronic properties of the materials. For semiconductors, the gap in the energy bands acts as a key enabling factor. Similar functionalities may be achieved following other mechanisms such as the plasmonic effect, the quantum confinement effect, or other similar effects on emerging materials (e.g., 2D materials). An important issue that needs research attention here is the energy of photons that can be absorbed and how they match the solar spectrum. As has been shown by the classical Shockley-Queisser analysis, the optimum absorption edge for a single absorber would be 1.34 eV for solar-to-electricity conversion. For the purpose of

solar fuel synthesis, the free energy gain of the target reactions imposes another constraint to the consideration, and the optimum absorption edge would be 1.6 eV if the reaction is water splitting.<sup>39</sup> Few materials match this absorption perfectly. A handful examples whose absorption edges are close to this desired value present new challenges such as mismatch of the band edge positions and stability. We will discuss strategies aimed at addressing these issues in Section 1.5.4 and 1.5.5.

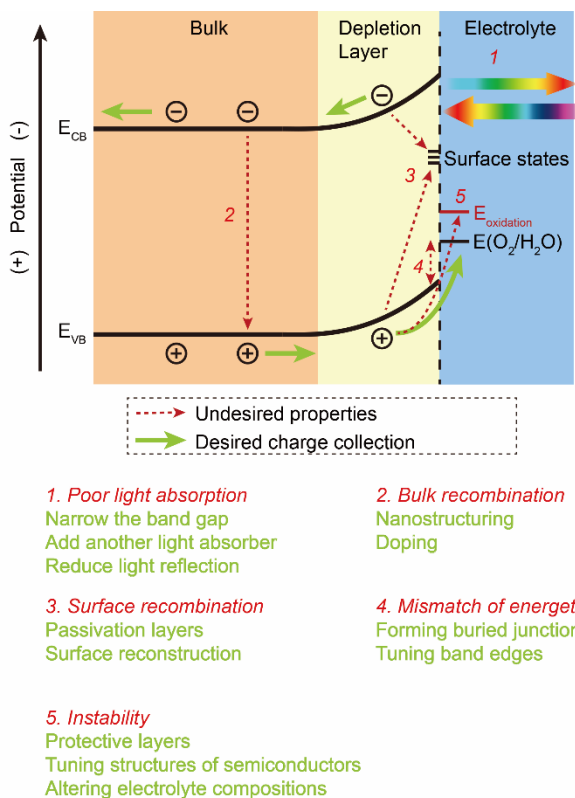


**Figure 1.5** The Schematic shows the charge excitation, separation, transport and transfer process (green arrows) in an n-type semiconductor in contact with aqueous electrolyte.  $E_{CB}$ : potential of conduction band minimum;  $E_{VB}$ : potential of valence band maximum;  $E_{oxidation}$ : potential of self-oxidation for the semiconductor;  $E(O_2/H_2O)$ : potential of water oxidation. The undesired properties including poor light absorption, bulk/surface recombination, mismatch of energetics and instability are indicated by the red arrows, with the corresponded strategies listed below as green texts.

The next step in solar fuel synthesis is charge separation and transport. Ideally, the only competing processes of this step would be radiative recombination, the result of

which would be photons that may be reabsorbed. In reality, however, recombination by a variety of other mechanisms constitutes the biggest loss in solar-to-electricity conversion. Efforts developed to address this issue arguably represent the biggest portion of materials-related research on solar fuels. We devote the bulk of subsection 1.5.2 on these efforts.

After the charges emerge to the surface, how they are utilized would be the next issue to be addressed. The desired processes would be facile forward charge transfer for solar fuel synthesis. Competing processes, aside from surface recombination that may be regarded as a solid-state process, include corrosion (parasitic chemical reactions that damage the photoelectrode itself) and side reactions (parasitic reactions that compete with solar fuel formation). Moreover, the energetics at the solid/liquid interface is of critical importance. There are a handful of materials that are highly efficient in absorbing light, separating and transporting charges but feature significant mismatch of the energetics with desired solar fuel synthesis reactions. That is, the charges are simply not energetic enough to carry out the reactions as desired. We will discuss these issues in Section 1.5.3.

## **1.5.1 Poor light absorption**

### **1.5.1.1 Narrow the band gaps or add another light absorber to enhance light absorption**

A common issue that limits the performance of materials with good optoelectronic properties (such as high light absorption coefficient, facile charge separation and transport) is the narrow absorption region relative to the overall solar spectrum. Two

general strategies have been developed to address this issue, including narrowing the band gap and adding another light absorber. For instance, the utilization of TiO<sub>2</sub> for practical water splitting is limited mainly by its wide band gap (3.2 eV for the anatase phase), even though it exhibits high incident photo-to-electron efficiencies and good chemical stability. The wide band gap means it can only absorb light in the deep UV region. It was hypothesized that the band gap might be narrowed through methods such as self-doping of Ti<sup>3+</sup> and/or oxygen vacancies by chemical reduction or ion doping.<sup>40</sup> To this end, Yang *et al.* reported core-shell nanostructured “black” rutile TiO<sub>2</sub>, which was synthesized by first forming a reduced shell of TiO<sub>2-x</sub> with TiO<sub>2</sub> nanoparticles and then post annealing in H<sub>2</sub>S to dope S into the shell of the nanoparticles.<sup>41</sup> Diffuse reflectance spectrum indicated that the band gap of the treated TiO<sub>2</sub> was 1.3 eV narrower than pristine rutile TiO<sub>2</sub>. After assembled into photoelectrodes by spin coating, the S-doped rutile TiO<sub>2</sub> showed 30-fold increase of photocurrent density at 1.23 V vs. reversible hydrogen electrode (RHE; All the potentials in this Chapter are versus RHE if no specific reference electrode is referred to). and negative shift of turn-on potential by 280 mV compared with pristine rutile TiO<sub>2</sub> in 1 M NaOH electrolyte. It is noted that whether the broadened absorption is actually due to the shift of the band edge positions would require additional research.

A better accepted example in tuning the band structures by varying the compositions is found in nitride semiconductors. For instance, GaN features a direct band gap of 3.4 eV, with the conduction band and valence band edges straddling the water splitting potentials. As a photoelectrode, early turn-on potentials and good fill factor have been obtained. Notwithstanding, its practical applications for solar water

splitting are limited due to the wide band gap. To further actualize the promises held by this material, researchers have tried to incorporate In during the synthesis, which was shown to reduce the band gap from 3.4 eV (pure GaN) and to 0.65 eV (pure InN).<sup>42</sup> Significantly, the change of the band gap between the two extremes is continuous, depending on the In concentrations in GaN. When used for water splitting applications, a key challenge is the stability of the material. In one example of such efforts, In<sub>0.21</sub>Ga<sub>0.79</sub>N films ( $E_g=2.3$  eV) with an average thickness of 1  $\mu\text{m}$  were synthesized on sapphire substrates by MOCVD.<sup>43</sup> After tested in 1 M HCl at 1.5 V vs. SCE under illumination, In and Ga elements were found in the electrolyte, confirming the material is being etched during the test. In another example, AlOtaibi *et al.* reported the synthesis of InGaN/GaN core/shell nanowire arrays (L=400-500 nm) on Si substrate.<sup>12</sup> With a band gap of 2.38 eV, the integrated photoanode reached 23 mA/cm<sup>2</sup> current density at 1 V vs. Ag/AgCl in a 1 M HBr electrolyte under AM1.5G illumination. Interestingly, the morphology and composition of the nanowires were confirmed to remain the same even after 24 hours PEC measurements. The superior stability may be explained by the MBE growth itself, which leads to nitrides of N-termination. It has been shown by Kibria *et al.* that such a termination offers better stability than Ga termination, which is expected for MOCVD-grown materials.<sup>44</sup>

To tune the band structures by changing the compositions of materials using methods such as MBE has been shown as a promising method to enhance light absorption by narrowing down the band gaps of semiconductors. By controlling the suitable compositions, the light absorption range can be extended from ultraviolet part to near-infrared region, covering the visible light spectrum. However, new issues are introduced

by such approaches. For instance, to achieve low-defect and high-quality materials, high-vacuum techniques are usually necessary, greatly raising the cost of the synthesis process. Low-cost alternative synthesis methods, such as solution-based ones, tend to yield materials of inadequate quality that are characterized by low solar-to-chemical-energy efficiencies. How to balance the efficiency and cost will continue to be a key focus for efforts focused on tailoring materials optoelectronic properties by changing their compositions.

Another strategy to broaden the range of light absorption is to complement the wide band gap material with narrow band gap absorbers. A large number of examples have been reported toward this direction. For example, Mayer *et al.* reported a dual-absorber photoanode consisting of Si nanowires (Si NWs) and  $\alpha$ -Fe<sub>2</sub>O<sub>3</sub>.<sup>21</sup> Thin films of  $\alpha$ -Fe<sub>2</sub>O<sub>3</sub> were deposited by ALD on the surface of high-aspect-ratio Si NWs with conformal coverage. Owing to the larger  $E_g$  (2.1 eV) of  $\alpha$ -Fe<sub>2</sub>O<sub>3</sub> compared with the one of Si ( $E_g$ =1.1 eV), incident photons with longer wavelength ( $600 \text{ nm} < \lambda < 1100 \text{ nm}$ ) were transparent for  $\alpha$ -Fe<sub>2</sub>O<sub>3</sub> and absorbed by the underlying Si. As a result, the utilization of overall solar spectrum was improved. In addition, the appropriate band alignment between n-Si and  $\alpha$ -Fe<sub>2</sub>O<sub>3</sub> created an appreciable band-bending depth, providing additional photovoltages and guaranteed electron injection from  $\alpha$ -Fe<sub>2</sub>O<sub>3</sub> to Si. As expected, the dual-absorber photoanode showed a more cathodic turn-on potential (0.6 V) and a higher photocurrent density in a 1.0 M NaOH electrolyte compared with the performance of planar  $\alpha$ -Fe<sub>2</sub>O<sub>3</sub> thin film grown on the FTO-coated glass substrate. Similarly, Hwang *et al.* reported a photoanode consisting of n-type Si NWs and thin films (35 nm) of n-TiO<sub>2</sub> on the surface.<sup>45</sup> The construction of n/n junction between n-Si and n-

TiO<sub>2</sub> not only improved the charge separation due to the band bending at the junction, but also introduced a potential barrier at the interface that blocked the holes back to the TiO<sub>2</sub> layer and reduced the loss of holes. In theory, the strategy of combining materials of complementary light absorption would enable broad light absorption for high performance; in practice, however, how to build a low-defect and intimate interface between different materials remains as a challenge.

### **1.5.1.2 Reduce reflection to avoid light absorption losses**

As has been shown in research on solar cells, optical loss due to reflection contributes significantly to the low performance of planar semiconductor materials when used for solar energy harvesting applications. Several strategies have been developed to meet this challenge. In the first approach, light absorption was shown to be enhanced by constructing nanostructures on the surface. For example, Garnett *et al.* discovered that by carefully controlling the diameter and density of Si nanowires, the path length of incident solar irradiation was enhanced by up to a factor of 73 when compared with Si thin films of the same thickness, thanks to the strong light trapping effect by the nanowire morphologies.<sup>46</sup> Maiolo *et al.* reported Si microwires synthesized through a vapor-liquid-solid method with Au as the catalyst.<sup>47</sup> With a length between 10 and 30  $\mu\text{m}$ , these Si wires showed enhanced photocurrent density and photovoltage in a 1,1'-dimethylferrocene ( $\text{Me}_2\text{Fc}$ )<sup>+0</sup> redox system in CH<sub>3</sub>OH when compared with planar samples. Dai *et al.* reported Si nanowire (NW) arrays synthesized through a Ag seeds assisted etching process.<sup>48</sup> In comparison with planar silicon, the Si NWs showed broadband anti-reflection properties with an optical reflectance of  $\sim 0\%$ , while the planar one reflected 19% of sunlight at the Si-water interface.

In another approach, designing suitable substrates underneath the semiconducting light absorber was also shown to enhance light absorption through recycling incident photons. For instance, Qiu *et al.* reported a mesoporous BiVO<sub>4</sub> deposited on a pre-designed nanocone substrate.<sup>49</sup> The light absorption was enhanced due to light trapping through multiple light scattering in the nanocone structure. Simulations of the electromagnetic wave distribution at  $\lambda=500$  nm for Mo:BiVO<sub>4</sub> on the nanocone substrate and a flat FTO-coated glass substrate indicated that the incident light was diffracted and redistributed in the nanocone area, owing to the match of the incident light wavelength and the distance between neighboring nanocone arrays. The results were also supported by enhanced absorption by BiVO<sub>4</sub> deposited on the nanocone substrate in UV-vis absorption spectrum. Similarly, Shi *et al.* reported the introduction of a distributed Bragg reflector (DBR) layer to improve the performance of a tandem cell device consisting of BiVO<sub>4</sub>/WO<sub>3</sub> photoanode and DSSC.<sup>50</sup> The DBR layer was placed on the back side of FTO glass for the BiVO<sub>4</sub>/WO<sub>3</sub> photoanode and served as the conductive counter electrode for the DSSC. The DBR layer consisting of multiple layers of materials with high- and low-refractive indices would reflect short-wavelength photons ( $\lambda < 500$  nm) while transmitting long-wavelength photons, leading to photon recycling by the BiVO<sub>4</sub> photoanode. A STH of 7.1% was achieved, corresponding to a  $J_{ph}$  of 5.75 mA/cm<sup>2</sup>, which was 1.1 mA/cm<sup>2</sup> higher than the one without DBR layers.

The strategies to reduce the light absorption can be widely implemented into different semiconductor materials. For instance, the light trapping effect and anti-reflection properties through nanostructuring have been achieved on various semiconductor platforms including Si, metal oxides and metal nitrides, etc. with carefully

controlled dimensions and structures. In addition, it can serve the purpose more than reducing the light reflection, such as enhancing the surface area for more catalytic sites and reducing charge recombination (more details in Section 1.5.2.1). At the same time, some issues may also occur due to enlarged contact area between semiconductors and electrolytes, such as more severe surface charge recombination. Future strategies need to make balance between the benefits and drawbacks.

## **1.5.2 Bulk recombination**

### **1.5.2.1 Nanostructuring to match the short diffusion length**

In one scenario, the recombination of photo-generated charges would take place due to the mismatched diffusion length of charge carriers with the light penetration depth. For instance, hematite features a light penetration depth of 46 nm at wavelength of 450 nm,<sup>51</sup> but its hole diffusion length is reported to be 2-4 nm,<sup>52</sup> meaning that most photogenerated holes would recombine with electrons before they are transferred to the semiconductor-electrolyte interface. To address this issue, nanostructuring has been applied to reduce the distance of charge transfer from bulk to surface while still ensuring sufficient light absorption, resulting in improved charge collection efficiency. One better-known example of this strategy is the cauliflower-type silicon-doped hematite thin film synthesized by atmospheric pressure chemical vapor deposition (APCVD) from  $\text{Fe}(\text{CO})_5$  and tetraethoxysilane on FTO-coated glass at 415 °C, reported by Kay *et al.* in 2006.<sup>16</sup> Its photocurrent density in 1 M NaOH at 1.23 V under AM 1.5 light illumination (100 mW/cm<sup>2</sup>) could reach 2.3 mA/cm<sup>2</sup>, which can be further improved to 2.7 mA/cm<sup>2</sup> with the addition of  $\text{Co}^{2+}$  catalysts.

Another example was found in electrodeposited Cu<sub>2</sub>O, whose electron diffusion length (20 to 100 nm)<sup>53</sup> is shorter than the light penetration depth (several μm at 2.4 eV)<sup>54</sup> by a large margin. Increasing the aspect ratios of nanostructured Cu<sub>2</sub>O has proven a promising method to address this issue. For example, Luo *et al.* synthesized Cu<sub>2</sub>O nanowire arrays via anodization and post annealing treatments.<sup>55</sup> Cu(OH)<sub>2</sub> nanowire was first formed by anodization; it was then converted to Cu<sub>2</sub>O during the post annealing in Ar atmosphere at 600 °C, featuring diameters of 100-300 nm and lengths of 3-5 μm. Additional electrodeposited Cu<sub>2</sub>O was introduced to cover the exposed Cu substrate, which was shown to significantly reduce charge recombination due to the contact between the Cu substrate and the protection layer (Al-doped ZnO). With further decoration of TiO<sub>2</sub> and RuO<sub>x</sub> (as the HER catalyst), the Cu<sub>2</sub>O nanowire photoelectrode achieved -10 mA/cm<sup>2</sup> photocurrent density at -0.3 V and a turn-on potential of 0.48 V in 0.5 M Na<sub>2</sub>SO<sub>4</sub> buffered at pH 5. By comparison, planar Cu<sub>2</sub>O films showed -7.8 mA/cm<sup>2</sup> photocurrent density at the same applied potential, indicating the effectiveness of the nanostructuring strategy.

Along the line of using nanostructures to help solve the mismatch between charge diffusion and optical depth, directly growing thin film light absorbers on nanostructures is yet another idea that has been exploited in the literature. For example, Lin *et al.* reported thin-film hematite (25 nm) grown on TiSi<sub>2</sub> nanonets by atomic layer deposition (ALD) using Fe<sub>2</sub>(O<sup>t</sup>Bu)<sub>6</sub> and H<sub>2</sub>O as precursors.<sup>20</sup> The TiSi<sub>2</sub> nanonet substrate not only provided a high surface area for better charge collection, but also served as a highly conductive charge collector. As a result, the nanonet-based hematite photoelectrodes achieved 1.6 mA/cm<sup>2</sup> photocurrent density at 1.23 V in 1 M NaOH, which was three

times higher than the planar thin film with the same thickness. To this end, Qiu *et al.*'s work of depositing mesoporous BiVO<sub>4</sub> on nanocone substrates may be regarded as similar.<sup>49</sup> Besides the ability to enhance the light absorption as mentioned previously, the nanocone structure reduced the charge transport distance in the photoelectrode, increasing charge collection efficiencies. Consequently, for the BiVO<sub>4</sub> nanoporous film of the same thickness on nanocone substrate and flat FTO glass substrate, the former showed a much higher photocurrent density (4.18 mA/cm<sup>2</sup>) at 1.23 V in pH 7 phosphate buffer than the latter (2.10 mA/cm<sup>2</sup>). With the introduction of Fe(Ni)OOH OER catalyst, the photocurrent density was further improved to 5.82 mA/cm<sup>2</sup>.

Another way of growing light absorbing nanostructures is to take advantage of templates with preformed nanoscale features. For instance, Ta<sub>3</sub>N<sub>5</sub> nanorods were prepared using an anodization method with porous anodic alumina (PAA) as the template in a H<sub>3</sub>BO<sub>3</sub> solution under high applied DC voltages (600-650 V), followed by high-temperature annealing in NH<sub>3</sub>.<sup>29, 56, 57</sup> Using this method, Li *et al.* reported that a 600 nm thick nanorod arrays showed enhanced photocurrent density at 1.23 V in 0.5 M Na<sub>2</sub>SO<sub>4</sub> (by 2.2 times at pH 13) with IrO<sub>2</sub> as a catalyst when compared with planar thin films of the same thickness and catalysts.<sup>56</sup> The improvement was attributed to the decreased distance for the photo-generated holes to reach the Ta<sub>3</sub>N<sub>5</sub> surface in the nanorod configuration. As far as Ta<sub>3</sub>N<sub>5</sub> is concerned, although nanostructures have been shown effective in improving the performance, the hole diffusion distance still remains a debate. On the one hand, Ziani *et al.* reported carrier lifetimes ranging from 3.1 to 8.7 ps in Ta<sub>3</sub>N<sub>5</sub> thin films based on transient spectroscopy measurements. These values would corresponded to a diffusion length between 3 and 9 nm.<sup>58</sup> On the other hand, Respinis *et*

*al.* reported a carrier lifetime of 1.6 ms based on time-resolved microwave conductivity measurements, corresponding to a diffusion length of 18,000 nm.<sup>59</sup> Further studies are necessary to reconcile the apparent discrepancies.

The advantages of nanostructuring have been discussed in Section 1.5.1.2. It is a versatile strategy for semiconductors suffering from short diffusion lengths. In addition, it may introduce more benefits at the same time, such as enhancing light absorption and increasing catalytic surface areas. However, large surface areas introduced by nanostructuring may also lead to side effects such as more defect states and more severe surface charge recombination.

### **1.5.2.2 Doping to enhance charge transport**

In the literature, it has been commonly referred to that high carrier concentration would improve charge collection. As will be summarized in this subsection, a number of efforts have been applied to increase charge carrier concentrations through approaches such as doping. However, how these approaches work has been poorly discussed. For instance, for an n-type semiconductor (e.g., metal oxide photoanode), dopants that are introduced to increase electron concentrations would decrease hole concentrations under equilibrium conditions according to the mass law. As such, these approaches may be regarded as decreasing bulk recombination thanks to the decrease of the minority carrier concentrations. A more common way of understanding the effect was often referred to in the literature as increasing the majority carrier concentration to improve the transport of photogenerated electrons (in the case of an n-type photoanode); as such, the utilization of photogenerated holes is improved, as well, due to reduced bulk recombination. These two views are actually consistent, just from different angles. A good example in this sub-

category is found in hematite, which usually features relatively low majority carrier concentrations ( $<10^{18} \text{ cm}^{-3}$ ).<sup>51</sup> Doping has been popularly sought as an effective method to change the situation. An added benefit of doing so is the shift of the equilibrium Fermi levels of electrons (toward the more negative direction), so as to increase the splitting between the Fermi level and the water oxidation potentials and, hence, the degree of band bending for better charge separation.

For instance,  $\text{Pt}^{4+}$ , in the form of chloroplatinic acid, was added into the  $\text{FeCl}_3$ -containing solutions during the synthesis of  $\beta\text{-FeOOH}$  thin film on FTO coated glass at  $100 \text{ }^\circ\text{C}$ , followed by a two-step annealing process at  $550 \text{ }^\circ\text{C}$  and  $800 \text{ }^\circ\text{C}$  to form Pt-doped hematite.<sup>60</sup> With an optimized thickness (500 nm) of the hematite thin film and a Pt/Fe ratio of 5%, the photoelectrode exhibited 74% enhancement of photocurrent density at 1.23 V in comparison with the undoped one. The Mott-Schottky analysis showed the donor density increased by one order of magnitude, supporting the role of  $\text{Pt}^{4+}$  as a dopant into hematite, which improved its electrical conductivity. Along the same line, Li *et al.* treated hydrothermally synthesized  $\text{WO}_3$  nanoflakes with chemical etching and reduction by poly(vinyl pyrrolidone) and ascorbic acid, respectively,<sup>61</sup> resulting in porous  $\text{WO}_3$  nanoflakes with increased surface oxygen vacancies (due to the reduction of  $\text{W}^{6+}$  to  $\text{W}^{5+}$ ). The high oxygen vacancies not only increased the carrier concentrations, but also narrowed the band gap by 0.1 eV. Consequently, the water oxidation performance at 1.23 V in 1 M  $\text{H}_2\text{SO}_4$  increased from  $0.62 \text{ mA/cm}^2$  for pristine  $\text{WO}_3$  nanoflakes to  $1.10 \text{ mA/cm}^2$  for the etch-reduced  $\text{WO}_3$  nanoflakes.

$\text{Mo}^{6+}$  and  $\text{W}^{6+}$  have been shown to be the most significant dopant for  $\text{BiVO}_4$ , which can substitute  $\text{V}^{5+}$  to increase the carrier concentrations. For example, Berglund *et*

*al.* reported Mo and W doped BiVO<sub>4</sub> by e-beam evaporation of Bi, V, Mo and W.<sup>62</sup> Both W and Mo doped BiVO<sub>4</sub> showed higher photocurrent density at 1.23V than bare BiVO<sub>4</sub>, while W/Mo co-doped BiVO<sub>4</sub> showed the highest value in pH 6.8 phosphate buffer solutions. In a different system, Han *et al.* introduced a gradient dopant profile to amorphous SiC to improve charge collection.<sup>63</sup> A 10 nm p-type amorphous SiC was first deposited via boron doping in a PECVD growth, followed by another 40 nm p-type amorphous SiC with a reduced dopant concentration and 40 nm intrinsic amorphous SiC. Due to the increased thickness of the depletion region between p-type and intrinsic SiC, the drift charge transport was enhanced in comparison to the diffusion-controlled process in intrinsic SiC, leading to an anodic shift of the turn-on potentials (~200 mV). When coupled with a Si photovoltaic module, the photocathode achieved the photocurrent density of -5.1 mA/cm<sup>2</sup> at 0 V in 0.1 M sulfamic acid with pH 3.75 under 1 sun illumination. The last example connects this line of research with those focused on improving photovoltaics through controlling the energetics within the buried junctions.

Doping is as a promising strategy to enhance the charge transport. On one hand, such a method has been well-developed in semiconductor fabrication industries, which can provide a rich knowledge base. On the other hand, various dopant elements have been explored, offering many options to modify semiconductors. However, there are still challenges remained when the doping strategy is applied, such as the uniformity of dopants.

### 1.5.3 Surface recombination

Even for pristine semiconductors, their surfaces are rich in electronic states whether in vacuum or in contact with a metal electrode. In addition to the types of states that would be abundant in bulk (e.g., due to dopants and/or impurities), surfaces feature unique defects such as dangling bonds and structural imperfections, which often introduce electronic states within the bandgap. These states are the origins for severe recombination at or near the surface. Significant research efforts have been devoted to understanding and addressing these recombination processes as they play important roles in defining the properties of the overall device. The situation is significantly more pronounced for photoelectrodes in photoelectrochemical applications because the surfaces are now in contact with a liquid where chemical reactions take place. Besides the usual suspects that would introduce surface states, chemisorbed species that are either reactants, intermediates or products act as centers to promote charge recombination. Below strategies that have been attempted to study and deal with this issue will be discussed.

#### 1.5.3.1 Use electron/hole scavengers to study the extent of surface recombination

Among the various techniques to study the surface recombination, using electron/hole scavengers has been widely applied as an important step. Taking hole scavengers as the example, they are usually reagents that can be more easily oxidized compared with water, which in principle can eliminate the surface charge recombination. To better reflect the effect, the photocurrent density ( $J_{ph}$ ) can be expressed via a simplified charge transfer process<sup>64</sup>:

$$J_{ph} = J_{abs} \times \eta_{sep} \times \eta_{inj} \quad (1.5)$$

In equation (1.5,  $J_{abs}$  is the photon absorption rate;  $\eta_{sep}$  is the separation efficiency, representing the fraction of holes reaching the electrode/electrolyte interface without recombining with electrons in the bulk;  $\eta_{inj}$  is the charge injection efficiency, representing the fraction of holes for desired oxidation reaction (e.g., water oxidation or scavenger oxidation) without recombining with electrons at the surface. When the hole scavenger is present,  $\eta_{inj}$  should be 100%. With the assumption that the existence of hole scavenger doesn't affect  $J_{abs}$  and  $\eta_{sep}$ ,  $\eta_{inj}$  for water oxidation can be derived from the ratio of  $J_{ph}$  for water oxidation and hole scavenger oxidation. Furthermore, the  $J_{abs}$  can be estimated from the light absorption spectrum of photoelectrodes. The measured  $J_{ph}$  for hole scavenger oxidation can be used to calculate  $\eta_{sep}$ , helping to understand the extent of bulk recombination.

For instance, Zhong *et al.* used  $H_2O_2$  as the hole scavenger to test  $BiVO_4$  photoanodes and compared it with the performance in the same electrolyte but without  $H_2O_2$ .<sup>65</sup> The  $\eta_{inj}$  for water oxidation was less than 60% at 1.2 V, which was improved significantly to near 100% after the deposition of Co-Pi. This demonstrated the effectiveness of Co-Pi to enhance the charge injection efficiency for water oxidation and reduce the surface charge recombination. Similarly, Liu *et al.* compared the performance of bare  $Ta_3N_5$  and  $Ta_3N_5$  with  $Co_3O_4$  nanoparticles using  $H_2O_2$  as the hole scavenger.<sup>28</sup> The  $\eta_{inj}$  for water oxidation increased from less than 20% to 70% at 1.23 V after the deposition of  $Co_3O_4$ , supporting the enhanced charge injection from photoanodes to water. In addition to studying the effect of passivation layer, the hole scavenger was also used to compare the extent of surface/bulk recombination in photoelectrodes prepared from different synthesis methods. For instance, Dotan *et al.* reported that hematite

photoanodes prepared via ultrasonic spray pyrolysis (USP) and APCVD showed different water oxidation performance.<sup>64</sup> With the help of H<sub>2</sub>O<sub>2</sub> as the hole scavenger, higher values of  $\eta_{sep}$  and  $\eta_{inj}$  for water oxidation were obtained for hematite synthesized by APCVD, indicating less bulk and surface recombination as well as better performance.

Using scavengers is a convenience yet powerful tool to understand the charge transfer behaviours in photoelectrodes. However, it also features some limitations. The  $\eta_{inj}$  derived here only represented the overall charge transfer from photoelectrodes to the electrolyte. It's hard to distinguish whether the change of  $\eta_{inj}$  is due to the change of reaction kinetics or surface charge recombination, especially when some passivation layers and catalysts are present. In addition, it is critical to choose suitable scavengers in order to obtain reasonable values of  $\eta_{inj}$ . For instance, Gao *et al.* found that the  $\eta_{inj}$  of CuWO<sub>4</sub> photoanodes for water oxidation was underestimated when H<sub>2</sub>O<sub>2</sub> was used as the hole scavenger.<sup>66</sup> The reason was the electron injection from the radical intermediate of H<sub>2</sub>O<sub>2</sub> oxidation to the conduction band of CuWO<sub>4</sub>, which made the expected 2-hole process becoming 1-hole process and led to current multiplications. Overall, more details about charge transfer behaviours can be revealed when more characterization tools such as photoelectrochemical impedance spectroscopy, intensity modulated photocurrent spectroscopy and so on are combined. More study about other techniques will be presented in section 1.7.1.

### **1.5.3.2 Passivation layers**

The most straightforward strategy may be to deposit a passivation layer on the surface of semiconductor. For instance, thin layer of metal oxides including Al<sub>2</sub>O<sub>3</sub>, In<sub>2</sub>O<sub>3</sub> and Ga<sub>2</sub>O<sub>3</sub> has been deposited on ultrathin hematite (27-30 nm) photoanode via a urea hydrolysis

CBD method.<sup>67</sup> The idea was to replace the hematite|water interface with a hematite|oxide|water one. By doing so, researchers expect to reduce surface recombination unique to the hematite|water interface. The most direct evidence has been the reduction of Fermi level pinning effect due to surface states, which is manifested by the increase of the photovoltage and, hence, a reduction of the turn-on potentials. Among those tested, Ga<sub>2</sub>O<sub>3</sub> has proven highly effective, which negatively shifted the turn-on potential by 400 mV. The improvement was attributed to the matching crystal structures between Ga<sub>2</sub>O<sub>3</sub> and hematite (<2.5% mismatch), resulting in low strains at the interface.

As will be further discussed later in section 1.7.1, the role played by the so-called “passivation layer” can be complex. A simple reduction in the turn-on potentials may be explained by at least three distinct mechanisms, including better catalysis, greater photovoltage or reduced recombination. These three mechanisms themselves are intricately interconnected, as well. For instance, better catalysis generally means faster forward charge transfer and, hence, reduced recombination; greater photovoltage implies better charge separation, which is typically a result of lower recombination. For this portion of discussions, these different functionalities are defined as follows. When the surface modification forms a buried junction with the photoelectrode to yield better charge separation, it is regarded as mainly improving the photovoltage; when the surface layer chiefly removes surface states to reduce recombination, it is considered as a passivation layer; when the surface materials speed up forward electron transfer, it is treated as a catalyst. Within this context, effective catalysts have been widely exploited to improve the performance of photoelectrodes, especially for the sluggish water oxidation reactions. For example, dual-layered FeOOH/NiOOH was deposited on

mesoporous  $\text{BiVO}_4$  surface by photo-assisted electrodeposition in sequence.<sup>35</sup> When  $\text{BiVO}_4$  decorated with dual-layered catalysts was compared with the bare one and the one with only  $\text{FeOOH}$  or  $\text{NiOOH}$ , in terms of the performance for water oxidation and sulfite oxidation, the one with dual-layered catalysts showed the earliest turn-on potentials and the highest water oxidation photocurrent densities. The effectiveness of combining  $\text{FeOOH}$  and  $\text{NiOOH}$  was attributed to the better interface formed between  $\text{BiVO}_4$  and  $\text{FeOOH}$  to reduce charge recombination, as well as more negative potential drop within the Helmholtz layer at the  $\text{NiOOH}$ /electrolyte interface (for more negative turn-on potentials) and better water oxidation kinetics. More examples will be discussed in the section 1.7 and the role of catalysts on semiconductor surfaces will be discussed in greater detail there.

Overall, using passivation layers to reduce surface recombination has been widely applied to improve the performance of photoelectrodes. Such a strategy offers a variety of materials' choices to serve as passivation layers, which makes it versatile for different types of study platforms. In addition, the deposition of passivation layer may also shed light on solving other limitations of photoelectrodes. For instance, metal oxides passivation layers can also serve as protective layers to enhance the stability. Catalytic passivation layer, on the other hand, may improve the kinetics of desired reactions. At the same time, however, it also requires deep understanding for the origins of surface recombination in order to choose suitable passivation layer. In addition, the deposition of extra layer on semiconductors may have the chance to introduce unexpected interfacial states, affecting charge transfer behaviors.

### 1.5.3.3 Surface reconstruction

Another strategy to deal with surface recombination is to change the crystal structure at the surface. For instance, Jang *et al.* reported a regrowth method to improve the performance of bare hematite.<sup>25</sup> By repeating the solution-based synthesis of FeOOH and post-annealing procedures in air, the authors found the photovoltage generated by bare hematite photoelectrode could be increased by 27%. During the re-growth, the surface structures of hematite were dissolved, and the newly grown structures favor the  $\langle 110 \rangle$  directions, which reduced the short-range structure disorder on the surface. In another study, NaBH<sub>4</sub> was used as the H<sub>2</sub> source to treat the hydrothermally synthesized hematite at 500 °C.<sup>68</sup> Such a treatment mainly introduced oxygen vacancies on the surface of hematite, which was supported by the decrease of pre-peak intensities in the surface-sensitive soft X-ray O K-edge XAS spectra in combination with the unchanged peak intensities in the bulk-sensitive hard X-ray Fe K-edge XAS spectra. The authors argued that the optimized oxygen vacancy content on the surface improved the conductivity of hematite and reduced the hole-electron recombination. As a result, the photocurrent density at 1.23 V increased from 0.88 mA/cm<sup>2</sup> for pristine hematite to 2.28 mA/cm<sup>2</sup> for the H<sub>2</sub>-treated hematite.

As is true in other complex systems, changes intended for the improvement of one aspect of the system may inadvertently impact another aspect negatively. For instance, increasing oxygen vacancies could be an effective strategy to increase carrier concentrations in WO<sub>3</sub> (e.g., Section 1.5.2.2), but they may also induce surface recombination. In an effort to achieve the positive effect of oxygen vacancies while minimizing its negative impacts, Zhang *et al.* reported a synthesis procedure combining

H<sub>2</sub> annealing and O<sub>3</sub> treatment, in which case H<sub>2</sub> annealing was shown to increase oxygen vacancies in the bulk of WO<sub>3</sub> while the subsequent O<sub>3</sub> treatment decreased oxygen vacancies on the surface.<sup>69</sup> The Mott-Schottky analysis supported the increase of donor densities after H<sub>2</sub> treatments, which remained after O<sub>3</sub> treatment. The lowest peak intensities in photoluminescence spectra for H<sub>2</sub>/O<sub>3</sub> treated samples indicated effective suppression of surface charge recombination, supporting the effect of reducing surface oxygen vacancies. As a result, the H<sub>2</sub>/O<sub>3</sub> treated photoelectrode showed a cathodic shift of turn-on potential (0.15 V) and increased photocurrent densities at 1.23 V in comparison to the samples that were just treated by H<sub>2</sub>.

Compared with depositing passivation layer to reduce surface recombination, surface reconstruction avoids the formation of additional interface, lowering the risk of generating more interfacial defects. However, such a strategy is material-specific and the knowledge obtained from one case study needs to be justified before being transferred to other study platforms.

#### **1.5.4 Mismatch of energetics**

For successful solar-to-chemical conversion reactions, it is of critical importance to match the energetics of the photoelectrode with the desired chemical reactions. In the case of significant mismatches, the photo-generated charges collected from the photoelectrode would not be energetic enough to drive the chemistry in the electrolyte. For instance, while CdSe is efficient in absorbing light and separating charges, photo-generated holes in this material would feature electronic energies too negative for H<sub>2</sub>O oxidation.<sup>70</sup> As such, examples of using this material for H<sub>2</sub>O oxidation applications are

rare. Instead, sacrificial electron donors are often involved when CdSe is studied in the context of solar fuel synthesis. A more common issue that concerns energetic mismatch is the relatively low photovoltages. Si is a good example. In vacuum, the potential of valence band maximum ( $E_{VB}$ ) of Si would be too negative for  $H_2O$  oxidation; yet, due to the existence and/or formation of native oxides on the surface, Si photoanodes have been successfully used for PEC  $H_2O$  oxidation, albeit with a low photovoltage as featured by the late turn-on potentials (Figure 1.6a).<sup>71</sup> Two general strategies have been tested to address this issue, forming buried junctions or tuning the band edge positions.

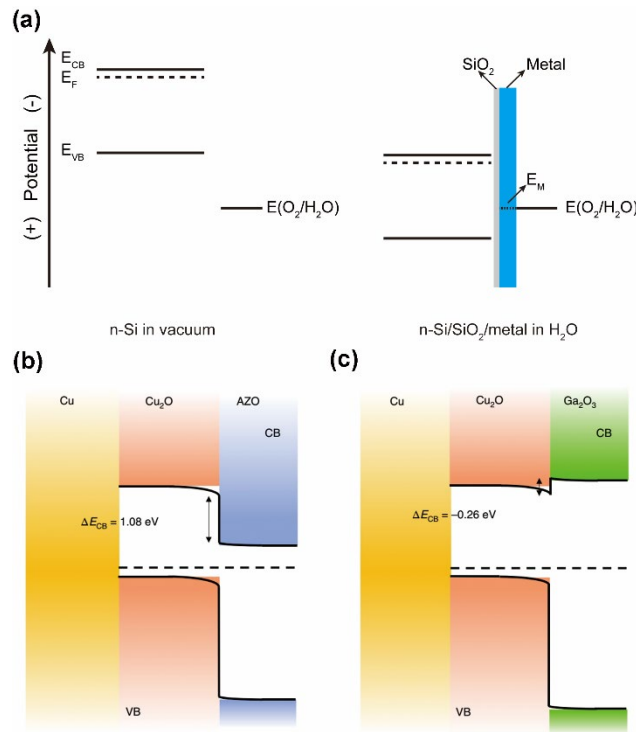


**Figure 1.6** (a) The schematic shows the band edge positions of n-Si in the vacuum before in contact with  $H_2O$  (left) and n-Si/SiO<sub>2</sub>/metal in contact with  $H_2O$  (right).  $E(O_2/H_2O)$ : water oxidation potential;  $E_M$ : work function of the metal;  $E_{CB}/E_{VB}$ : the conduction band minimum/valence band maximum positions;  $E_F$ : Fermi level. Equilibrium band-edge diagrams of Cu<sub>2</sub>O/AZO (Al doped ZnO) (b) and Cu<sub>2</sub>O/Ga<sub>2</sub>O<sub>3</sub> (c) heterojunctions with different conduction band edge discontinuity ( $\Delta E_{CB}$ ). (c) and (d) reproduced from “L. Pan, J. H. Kim, M. T. Mayer, M.-K. Son, A. Ummadisingu, J. S. Lee, A. Hagfeldt, J. Luo and M. Grätzel, *Nat. Catal.*, 2018, 1, 412-420.” with permission from Springer Nature.

#### 1.5.4.1 Forming buried junctions

The flat-band potential of  $\text{Cu}_2\text{O}$  has been reported at around 0.7 V, which limits the maximum photovoltage when used for  $\text{H}_2\text{O}$  reduction. In order to address this issue, buried p-n junction has been applied to enhance the photovoltage. One example is to replace the  $\text{Cu}_2\text{O}/\text{H}_2\text{O}$  interface with a  $\text{Cu}_2\text{O}/\text{ZnS}$  interface.<sup>22</sup> Due to the more negative conduction band edge position and the more negative Fermi level of ZnS relative to the HER potential, the strategy increased the band bending within  $\text{Cu}_2\text{O}$  for a turn-on potential of 0.72 V; by comparison,  $\text{Cu}_2\text{O}$  without ZnS showed a  $V_{\text{on}}$  of only 0.6 V in 0.2 M  $\text{KH}_2\text{PO}_4$  at pH 7. The increased photovoltage was confirmed by the light open-circuit potential measurements under various light intensities. Another example is reported by Li *et al.*, in which the authors deposited a thin layer of  $\text{Ga}_2\text{O}_3$  buffer between  $\text{Cu}_2\text{O}$  and  $\text{TiO}_2$  (as a protection layer) by ALD.<sup>72</sup> The idea was to maximize band bending within  $\text{Cu}_2\text{O}$  by introducing  $\text{Ga}_2\text{O}_3$ . Through photoelectron spectroscopy measurements, they found the conduction band offset between  $\text{Cu}_2\text{O}$  and  $\text{Ga}_2\text{O}_3$  was in the range of -0.37 to +0.01 eV, suggesting that in addition to a large degree of band bending, electron transfer across the  $\text{Ga}_2\text{O}_3$  layer should be facilitated. A stark comparison could be made between  $\text{Ga}_2\text{O}_3$  and  $\text{ZnO}$ , which would also serve the purpose of increasing band bending when integrated with  $\text{Cu}_2\text{O}$ . But  $\text{ZnO}$  features a significant mismatch with  $\text{Cu}_2\text{O}$  in terms of potential of conduction band minimum ( $E_{\text{CB}}$ ), which would impede electron transfer from  $\text{Cu}_2\text{O}$  to  $\text{ZnO}$ . As such,  $\text{ZnO}$  is much less desired for the same purpose (Figure 1.6b&c). Indeed, a turn-on potential of 1.02 V was achieved for the integrated  $\text{Cu}_2\text{O}|\text{Ga}_2\text{O}_3|\text{TiO}_2$  photoelectrode in 0.5 M  $\text{Na}_2\text{SO}_4$  buffered at pH 4.26. Pan *et al.* further advanced this strategy by integrating nanowire nanostructuring, a  $\text{Ga}_2\text{O}_3$  buffer layer, a  $\text{TiO}_2$  protection

layer and RuO<sub>x</sub> as HER catalysts.<sup>33</sup> Together, a turn-on potential >1 V and a photocurrent density of -10 mA/cm<sup>2</sup> at 0 V, as well as stability over 100 h were obtained at pH 5.

Using a similar strategy on a different material, Digdaya *et al.* improved the performance of amorphous SiC.<sup>73</sup> They deposited a thin layer (25 nm) of n-TiO<sub>2</sub> on a-SiC (100 nm) by ALD, replacing the original semiconductor/liquid electrolyte interface with a p-i-n solid junction. Under illumination, photo-generated holes would drift to the p-type amorphous SiC layer and electrons to the n-type TiO<sub>2</sub>. Due to the formation of a buried junction, the photovoltage was increased by 300 mV. After the electrodeposition of active HER catalysts, Ni-Mo, the integrated thin-film photocathode achieved a turn-on potential of 0.8 V and a photocurrent density of -8.3 mA/cm<sup>2</sup> at 0 V in pH 4 phosphate buffer. In addition to forming a buried junction, the TiO<sub>2</sub> layer also enhanced the adhesion of the catalysts to the surface, leading to stable HER operation for 12 h.

In addition to aforementioned examples, forming buried junction has been applied in various semiconductor materials such as Si, III-V compounds, etc., which has been shown as an effective way to improve the photovoltage output. However, some challenges still need to be addressed in this process, such as how to create defect-free interface and how to achieve uniformly deposition on high-aspect-ratio substrates, etc.

#### **1.5.4.2 Tuning band edge positions**

Although Si features high photocurrent density as photoelectrodes, its photovoltage has been limited. When it was used as a photocathode, the photovoltage has been limited to 400 mV without additional buried junctions. As a photoanode, theoretically it cannot oxidize water due to the negative position of the E<sub>VB</sub>. The issue has been shown to be

partially addressable by strategies such as forming a metal-insulator-semiconductor interface (e.g., Ni-SiO<sub>2</sub>-Si), where high photocurrent density was measured. But the turn-on potential was still relatively positive (1 V), representing a photovoltage of only 0.23 V.<sup>74</sup> To further address this problem, amorphous silicon has been developed. Hydrogenated amorphous silicon has a continuously random bonding network, resulting in a relatively large band gap (1.7 eV) and more positive E<sub>VB</sub> for improved photovoltage and better alignment with water oxidation energy levels. Additionally, a-Si has been shown to be a much more efficient light absorber due to the direct nature of the band gap. Importantly, knowledge of semiconductor thin film growth makes it facile to control the doping type and level of a-Si with ease, making it possible to utilize it for both oxidation and reduction reactions readily. To this end, Lin *et al.* reported a-Si with a buried p-i-n structure.<sup>19</sup> Using a glass substrate decorated with 1.8 μm thick pyramidally textured ZnO, 250 nm intrinsic a-Si (active light absorber) were sandwiched between thin layers of p-type and n-type nanocrystalline silicon via plasma-enhanced CVD. After further decoration of a TiO<sub>2</sub> protection layer and Pt HER catalysts, the photocathode showed a turn-on potential of 0.93 V and a photocurrent density of 11.6 mA/cm<sup>2</sup> at 0 V in pH 4 phosphate buffer under 1 sun illumination. The reported turn-on potential was even more positive than what was obtained on n<sup>+</sup>p-Si (usually limited to 0.54 V).

Compared with forming buried junctions, tuning the band edge positions of semiconductors to solve the mismatch of energetics can avoid the risk of forming interfacial defects between different layers. However, only a handful of materials can be modified using such a method, which limits its applications.

### 1.5.5 Instability

Among the issues discussed in this section, instability of photoelectrodes is arguably the most unique to photoelectrochemical applications. Concerns such as narrow light absorption, bulk and surface recombination and charge transport are shared by other semiconductor-based applications. But instability defines photoelectrochemical systems because only for this application does one need to subject a semiconductor material to harsh conditions – intense illumination plus extreme pH environments with high salt concentrations. Broadly speaking, we refer to instability as the rapid degradation of the photoelectrode performance. The phenomenon may be attributed to at least three distinctly different causes: 1. The deactivation of the active sites by mechanisms such as accumulation of by-products; here little change to the photoelectrode itself occurs; 2. The deactivation of the photoelectrode due to the loss of photovoltages, where the photoelectrode loses or gains little in a physical sense; 3. Significant changes to the photoelectrode due to corrosion during the chemical and/or photoelectrochemical reactions.

#### 1.5.5.1 The accumulation of byproducts due to parasitic chemical reactions

It has been shown that the formation and accumulation of peroxy species on  $\text{WO}_3$  surfaces during water oxidation may lead to the loss of photoactivities.<sup>75</sup> The mechanism is to be differentiated from corrosion, which is well known for  $\text{WO}_3$  at higher pH (e.g.,  $>4$ ) due to the loosely bound  $\text{WO}_3(\text{H}_2\text{O})_x$  species on the surface.<sup>76</sup> How to suppress the side reaction will be the key to reactivate the photoelectrode. Seabold *et al.* reported that the deposition of Co-Pi on  $\text{WO}_3$  improved the photocurrent to  $\text{O}_2$  conversion efficiency

from 61% to 100%.<sup>77</sup> At the same time, the  $\text{WO}_3$  was shown to be stable under water oxidation condition for 12 h after the deposition of Co-Pi in pH 7 phosphate buffer, while the bare one lost 63% of its initial photocurrent density within 1 h. Other than introducing OER catalysts, Ma *et al.* used a solution-based reducing reagent, LEDA (lithium dissolved in ethylenediamine), to create an amorphous overlayer on mesoporous  $\text{WO}_3$  photoanode.<sup>26</sup> Consisted of both oxygen vacancies and tungsten vacancies, such an amorphous layer improved charge transfer efficiency, reducing the formation of peroxide species due to hole accumulation. As a result, both the photocurrent density/turn-on potential and the stability were improved. In a different approach, Wang *et al.* tailored the orientation of exposed facets during the hydrothermal growth of  $\text{WO}_3$ .<sup>78</sup> With increased (002) facets as opposed to (200) facets in  $\text{WO}_3$ , the photocurrent density at 1.23 V was improved from 2.1  $\text{mA}/\text{cm}^2$  to 3.1  $\text{mA}/\text{cm}^2$ , with the stability also enhanced. Such a result was attributed to the reduced electron-hole recombination and inhibited peroxo-species on (002) facets.

#### **1.5.5.2 Deactivation of the photoelectrode due to loss of photovoltages**

It has been commonly observed that the performance of  $\text{Ta}_3\text{N}_5$  quickly decayed during water oxidation, which was generally attributed to the oxidation of nitrides. Indeed, nitride oxidation was observed after water oxidation, confirming the formation of oxides. However, it was unclear how the surface oxidation was related to the performance decay. Another puzzle about  $\text{Ta}_3\text{N}_5$  is the positive turn-on potentials for water oxidation ( $>0.6$  V), which is significantly higher than what one would expect from the material based on measurements of the band edge positions and Fermi levels in vacuum. He *et al.* reported a detailed study on the detailed changes on the surface of  $\text{Ta}_3\text{N}_5$  during water oxidation

using a combination of photoelectrochemical methods, high-resolution electron microscopy and X-ray core-level spectroscopy.<sup>79</sup> It was found that the oxidation of Ta<sub>3</sub>N<sub>5</sub> nanotubes (NTs) to tantalum oxide was self-limited on the surface during water oxidation, leading to the formation of a relatively thin amorphous oxide layer (~ 3 nm). The surface oxidation process not only introduced increased charge transfer resistance, but also shifted the Fermi level positively by 200 mV, leading to significant Fermi-level pinning that greatly limits the measurable photovoltages. Moreover, chemisorption of H<sub>2</sub>O onto Ta<sub>3</sub>N<sub>5</sub> alone was found to introduce an additional positive shift of the flat-band potential by nearly 600 mV. This shift explains why most reports on Ta<sub>3</sub>N<sub>5</sub> only observed highly positive turn-on potentials when characterizing the material in water. By comparison, a much less positive potential could be measured in nonaqueous systems, such as acetonitrile. The results imply that even though surface oxidation is relatively mild when measured by thickness, the reaction could suppress the achievable performance of nitrides by a large margin. More details about the study will be discussed in Chapter 2.

### 1.5.5.3 Corrosion

BiVO<sub>4</sub> in near-neutral and alkaline solution is known to be susceptible to chemical and photochemical corrosion, although thermodynamically it is expected to be stable. Toma *et al.* studied the instability of polycrystalline BiVO<sub>4</sub> using various methods, including SEM, TEM, Rutherford backscattering spectrometry (RBS), *in-situ* electrochemical AFM, ICP-MS and computational prediction.<sup>80</sup> It was found that the V in BiVO<sub>4</sub> dissolved in the electrolyte. Thermodynamically, a self-passivation process should take place via the formation of a chemically stable bismuth oxide on BiVO<sub>4</sub> surface.

However, such a process is kinetically hindered at room temperature in aqueous solutions, leading to the formation of defective and unstable bismuth oxide or hydroxide. As a result, bulk dissolution of  $\text{BiVO}_4$  occurs, which would be accelerated by illumination, increased pH and/or applied bias. It was hypothesized that the photo-induced chemical instability may be a result of the accumulation of holes on the surface and the formation of reactive oxygen species, which could oxidize  $\text{Bi}^{3+}$  to  $\text{Bi}^{5+}$  or oxidize  $\text{O}^{2-}$  to  $\text{O}^\cdot$ . To address the instability issue, one common strategy was to protection layer to avoid the contact between  $\text{BiVO}_4$  and  $\text{H}_2\text{O}$ , and introduce the OER catalyst to guide the hole transfer for water oxidation instead of self-oxidation. Another class of materials that have been intensely studied for their corrosion problems are high-efficiency phosphides and/or arsenides. More details will be discussed next in the strategies on how to protect them.

#### **1.5.5.4 Protection strategies**

One common strategy to protect unstable materials is to conceal the reactive surface altogether by one or multiple protection layers. Stable oxide materials (e.g.,  $\text{TiO}_2$ ) have been used to serve this purpose. The key here is to achieve uniform and compact deposition of protective materials with appropriate thicknesses, so that the contact between the electrolyte and the semiconductor can be separated to prevent corrosion, yet efficient charge transfer across the protection is ensured. Due to the lack of inherent catalytic activities on such protection layers, catalysts are often required. In addition, one should manage light absorption so that the protection layer does not compete with the active material in absorbing in the visible range. For the ease of discussions, we summarize materials studied for the purpose of protection based on their types below.

## Catalytically-inactive oxide/nitride materials

Metal oxides with wide band gaps have been studied extensively as a protection layer for both photocathodes and photoanodes.  $\text{TiO}_2$  is one of the most representative examples for this purpose, which has been applied to various photoelectrode materials including Si,<sup>13, 19, 71</sup> III-V semiconductors,<sup>71, 81-83</sup> unstable metal oxides ( $\text{Cu}_2\text{O}$ ,<sup>22, 33, 55, 84</sup>  $\text{BiVO}_4$ ,<sup>23</sup> etc.) and metal chalcogenides (CZTS,<sup>27</sup> etc.). For instance,  $\text{TiO}_2$  has been reported to serve as a protective material on various photocathodes. Gu *et al.* reported a bilayer protection of  $\text{GaInP}_2$  photocathode by amorphous  $\text{TiO}_x$  and  $\text{MoS}_x$ ,<sup>83</sup> which were deposited by ALD and electrochemical deposition, respectively. Further annealing in Ar atmosphere at 450 °C improved the crystallinity of  $\text{MoS}_2$  and  $\text{TiO}_2$ , as well as forming a hybrid interface between  $\text{MoS}_2$  and  $\text{TiO}_2$  in the form of  $\text{MoS}_x/\text{MoO}_y\text{O}_z/\text{MoO}_x/\text{TiO}_2$ . Compared with the as-deposited photoelectrode, the annealed one showed not only better fill factors but also enhanced stability. After 20 h photoelectrolysis at 0 V in 0.5 M  $\text{H}_2\text{SO}_4$ , the photocurrent density of the as-deposited one decreased from 10  $\text{mA}/\text{cm}^2$  to 5  $\text{mA}/\text{cm}^2$ , while the annealed one only decreased by less than 20%. In terms of using  $\text{TiO}_2$  to protect photoanodes, Verlage *et al.* synthesized III-V tandem cells using MOCVD on  $n^+$ -GaAs (100).<sup>81</sup> The tandem light absorber consisted of an InGaP top cell ( $E_g=1.84$  eV, 550 nm) and a GaAs bottom cell ( $E_g=1.42$  eV, 3200 nm), connected by an AlGaAs/GaAs tunnel junction (40 nm). An amorphous, hole-conducting  $\text{TiO}_2$  layer (62.5 nm) was deposited on the light absorber surface by ALD to prevent photocorrosion as well as serving as an anti-reflection coating, with additional 2 nm Ni as the OER catalysts. When connected to a Ni-Mo cathode in 1 M KOH electrolyte, the device was shown to split water without external bias at a current density of 8.5  $\text{mA}/\text{cm}^2$  under 1 sun

illumination, which decreased to 7.3 mA/cm<sup>2</sup> after 80 h operations. Similar protection layer/catalyst combinations have been shown effective in protecting photoanodes of a variety compositions, including Si, GaP, GaAs and BiVO<sub>4</sub>.<sup>71</sup> .

Oxide materials as a protection layer face limitations when directly applied to nitride semiconductors (e.g., Ta<sub>3</sub>N<sub>5</sub>), which are often sensitive to oxidative conditions. To address this issue, Zhong *et al.* reported a GaN-protected Ta<sub>3</sub>N<sub>5</sub> photoanode.<sup>11</sup> In this study, GaN (50 nm) was synthesized by e-beam evaporation and subsequent nitridation. With Co-Pi as the OER catalysts, the protected photoanode showed a turn-on potential of 0.65 V and a photocurrent density of 8 mA/cm<sup>2</sup> at 1.23 V in 0.5 M phosphate buffer (pH 13). Importantly, it achieved stable water oxidation at 1.2 V for 10 h. Control samples of Ta<sub>3</sub>N<sub>5</sub> without GaN quickly decayed within 1 h, due to the formation of surface oxides.

### **Catalytically-active materials**

Another strategy to protect the photoactive material is to minimize parasitic chemical reactions such as corrosion by speeding up the desired chemical reactions. That is, using catalysts to facilitate charge transfer for desired solar fuel synthesis may be regarded as a good strategy for protection purposes. For water oxidation, transition metal oxide/hydroxides (e.g., CoO<sub>x</sub>,<sup>28, 85</sup> Co(OH)<sub>2</sub>,<sup>29, 86</sup> Ni(OH)<sub>2</sub>,<sup>24, 87, 88</sup> NiFe-LDH,<sup>30</sup> etc.) have been commonly used. For water reduction, precious metal catalysts (e.g., Pt<sup>22, 89, 90</sup>) or non-noble-metal catalysts (e.g., MoS<sub>2</sub><sup>83, 91</sup>) are usually applied. For example, efficient electrocatalysts such as Pt and MoS<sub>2</sub> have been shown to stabilize high-performance photocathodes. MoS<sub>2</sub> has been used to protect GaInP<sub>2</sub>, as reported by Britto *et al.*<sup>91</sup> Thin-film GaInP<sub>2</sub> (~200 nm) was coated by a thin layer (3.6 nm) of Mo metal, which was partially converted to MoS<sub>2</sub> through sulfurization. In a sulfuric acid electrolyte (cc. 3 M),

bare GaInP<sub>2</sub> showed quick performance decay (within minutes) and complete failure after several hours due to dissolution. In stark contrast, GaInP<sub>2</sub> coated with Mo/MoS<sub>2</sub> showed enhanced turn-on potentials during the initial test (presumably due to more exposed edge sites of MoS<sub>2</sub>) and stable HER performance for 60 h. Along this line, Kumagai *et al.* reported that the performance of CIGS photocathode could be improved significantly by adding a thin layer of Ti/Mo between CIGS/CdS and Pt.<sup>10</sup> The authors attributed the phenomenon to better electron transfer from CIGS/CdS to Pt. The stability of the integrated photocathode was improved to 10 days.

It is important to note that the protection effect by similar materials is apparent as long as efficient charge extraction from the semiconductors is achieved. For instance, Liu *et al.* reported a hydrothermally-deposited ferrihydrite layer on Ta<sub>3</sub>N<sub>5</sub>, when coupled with Co<sub>3</sub>O<sub>4</sub> OER catalysts, could significantly improve the stability of the latter to up to 6 h.<sup>28</sup> As a comparison, Ta<sub>3</sub>N<sub>5</sub> with only Co<sub>3</sub>O<sub>4</sub> showed 70% of decay within 2 h. The role of the ferrihydrite was revealed as a storage layer for photogenerated holes in the form of positively charge states. Besides the ferrihydrite, the combination of Ni(OH)<sub>x</sub> and MoO<sub>3</sub> was shown to work well as a hole storage layer for the protection of Ta<sub>3</sub>N<sub>5</sub>.<sup>87</sup> When used alone on Ta<sub>3</sub>N<sub>5</sub>, the Ni(OH)<sub>x</sub>/MoO<sub>3</sub> layer featured low charge injection efficiency (<15%) and, therefore, is an inefficient OER catalyst.

Overall, protective layers have become a critical component for high-efficiency but unstable semiconductor materials. Numerous research efforts have been devoted to this research direction, and various types of protective materials have been reported, providing a rich knowledge base for its applications in different study platforms.

### **Other strategies**

In addition to depositing protection materials, modifying the photoelectrode|electrolyte interface by strategies such as changing the structures of the semiconductors or altering the compositions of the electrolyte has been reported as effective in addressing the instability issues. To this end, Kuang *et al.* reported that the crystallinity of BiVO<sub>4</sub> nanoparticles was enhanced after a two-step high temperature annealing treatment (800°C-ball milling-700°C).<sup>92</sup> These nanoparticles exhibited inherently better stability against photocorrosion in comparison to nanoworm BiVO<sub>4</sub>, which was obtained by annealing at 450°C. With the introduction of self-generation and regeneration of NiFe-based OER catalysts, the stability was further extended to >1000 h. In terms of surface modifications, by tuning the exposed surface of single crystalline GaN to be N-terminated, Kibria *et al.* found that MBE-grown GaN showed better photostability than the ones grown by conventional MOCVD, whose Ga-terminated surfaces could be easily oxidized to Ga<sub>2</sub>O<sub>3</sub> in the presence of oxygen/H<sub>2</sub>O and dissolved in the electrolyte, leading to the photocorrosion as well as Fermi level pinning.<sup>44</sup> Moreover, since the loss of V<sup>5+</sup> was involved in the photocorrosion of BiVO<sub>4</sub>, Lee *et al.* introduced a V<sup>5+</sup>-saturated 1 M borate buffer (pH 9.3) for water oxidation test.<sup>93</sup> Based on the Le Châtelier principle, the dissolution of V<sup>5+</sup> was hindered. As a result, the stability of the BiVO<sub>4</sub> photoelectrode was improved. With additional decorations of FeOOH/NiOOH OER catalysts, the stability of BiVO<sub>4</sub> in the V<sup>5+</sup>-saturated electrolyte was extended to 500 h.

Compared with the deposition of protective layers, the aforementioned strategies reduced the decoration materials on semiconductors, simplifying the photoelectrode

configurations. However, the broad applications of these strategies beyond the case studies remain to be seen.

## 1.5.6 Other issues

### 1.5.6.1 High fabrication cost

In addition to materials cost, the fabrication process itself could incur significant cost. In general, the cost concern limits the scale of implementation for many high-performance materials, especially III-V semiconductors (e.g., GaAs, InGaP, etc.). Many strategies developed to reduce costs of solar cells are expected to be transferrable to solar fuel synthesis, as well. For example, while effective in synthesizing high quality semiconductor thin films, MOCVD tends to be an expensive process. An even more expensive part, however, comes from the usage of single-crystalline III-V substrates for epitaxial growth of solar cell-grade materials. To address this problem, researchers have optimized the synthesis so that the expensive substrates may be recycled for repeated growths. Moreover, other less expensive synthesis methods have been explored to replace the MOCVD, which has been reviewed elsewhere<sup>94</sup>. Similar arguments are equally applicable to MBE processes.<sup>95</sup>

As an example of transferring knowledge learned in research on photovoltaics to solar fuel applications, Kang *et al.* fabricated GaAs/Al<sub>x</sub>Ga<sub>1-x</sub>As based photocathodes and photoanodes using epitaxial lift-off and printing-based assemblies (Figure 1.7).<sup>14</sup> During the synthesis, a p-on-n or n-on-p epitaxial GaAs solar cells were first grown on a GaAs wafer, which were later lifted off and printed on glass substrates. Pt and IrO<sub>x</sub>·nH<sub>2</sub>O was deposited to serve as the water reduction and oxidation catalysts, respectively. Such a



### 1.5.6.2 Charge recombination at semiconductor/substrate interface

As discussed in Sections 1.5.2 and 1.5.3, charge recombination in the bulk or near the surface can lead to decreased charge collection efficiency. In another case, charge recombination can take place at the semiconductor/substrate interface. For example, the formation of a “dead layer” at the hematite-substrate interface, especially in ultrathin film (with thickness < 50 nm), was believed as the result of lattice strains between hematite and the substrate (usually FTO), which would lead to imperfect crystal structures near the interface and induce charge recombination.<sup>97</sup> Hisatomi *et al.* reported a thin layer of Ga<sub>2</sub>O<sub>3</sub> (2 nm) between the FTO substrate and hematite can serve as an isomorphic structure template for the growth of ultrathin hematite (27 nm) due to their similar crystal structures. After the FTO substrate was modified with Ga<sub>2</sub>O<sub>3</sub>, the crystallinity of hematite was improved based on the increased peak intensity observed in XRD. As a consequence, the turn-on potential was cathodically shifted by 200 mV and the photocurrent density at 1.23 V was improved by 15 times.<sup>67</sup> Zandi *et al* used ALD to synthesize Ti-doped hematite by tuning the numbers of Ti precursor (titanium isopropoxide) pulses and Fe precursor (ferrocene) pulses during the ALD process.<sup>98</sup> Although Ti<sup>4+</sup> has been reported to serve as the dopant to improve the donor density in hematite, the introduction of Ti in this study showed no effect on carrier concentration. Instead, the bulk properties were improved with hole mobility and/or the hole lifetime enhanced after the introduction of Ti, which was due to the elimination of dead layer. In addition, EIS analysis indicated a higher density of active sites for water oxidation was achieved after the Ti doping.

## 1.6 THIN FILM PROTECTION LAYER

Thin-film protection materials for photoelectrodes have been recently reviewed in detail.<sup>99, 100</sup> Here those thin-film protection materials based on their method of protection are briefly summarized. One method protects the semiconductor by isolating the unstable surface from the aqueous electrolyte, which inhibits the photoelectrochemical or chemical dissolution of the semiconductor. We refer to this protection method as a physical barrier layer. The other method inhibits photocorrosion of semiconductors by selectively tuning the pathway of photogenerated charge carriers to the desired chemical reactions opposed to the corrosion. Since this method of protection relies on optimizing relative rates of reactions, we refer to it as a kinetic protection layer. Some examples of thin-film protection layers have been discussed in section 1.5.5.4.

### 1.6.1 Physical barrier protection layer

In order to fully isolate the unstable semiconductors from the aqueous electrolyte, the protection layers are required to be ion-impermeable and pin-hole free. Therefore, deposition techniques that feature uniform coating of dense material, such as PVD and CVD, are usually applied to deposit the films. On the other hand, since this type of materials is catalytic non-active, it's important to control its thickness to be thin and conductive so that the photo-generated charge carriers can be transferred to the catalyst/electrolyte.

Metal thin films such as Ti<sup>101</sup> or Pd<sup>102</sup>, have been demonstrated to protect crystalline Si photocathodes and photoanodes. The metals can form Schottky-junctions

with semiconductors and serve as conductive layers, and the photogenerated electrons or holes can be separated and transferred to solution. One limitation of using metal protection layers is the competition of light absorption with the semiconductor underneath. One way to overcome this drawback is to illuminate from the back side of photoelectrode instead of the electrolyte side. For example, Bae *et al.* reported that by thinning the p-Si photocathode from 350  $\mu\text{m}$  to 30  $\mu\text{m}$  by wet etching, increased photocurrent density was observed by illuminating the Si from the back side.<sup>103</sup> In this configuration, the protection was achieved by depositing Ti/TiO<sub>2</sub> (5/100 nm) on the surface. Kang *et al.* changed the catalytic side of photoelectrode from the semiconductor/electrolyte junction to the ohmic contact/electrolyte interface using printing-based material assemblies.<sup>14</sup> In this case, the “thick” layer of metal contact (AuGe/Ni/Au: 100 nm/30 nm/150 nm) was used to separate the GaAs photocathode from an aqueous electrolyte, realizing 8 hours stable HER. The unprotected one showed quick performance decay with 2 hours.

As discussed in section 1.5.5.4, stable metal oxides and nitrides have been developed as protection layers. For example, amorphous TiO<sub>2</sub> has been deposited on BiVO<sub>4</sub> photoanode by ALD, followed by sputtering of Ni on the surface as the OER catalyst.<sup>23</sup> With the thickness around 1 nm, this amorphous protection layer achieved stable water oxidation in pH 13 electrolyte for 120 min, while the bare BiVO<sub>4</sub> showed quick decay of performance within 20 min due to the chemical and photoelectrochemical dissolution. On the photocathode side, it has been reported that Cu<sub>2</sub>O photocathodes can be stabilized via the deposition of ZnO (20 nm) and TiO<sub>2</sub> (10 nm) by ALD.<sup>84</sup> It should be noted here that the deposition of TiO<sub>2</sub> alone didn't stabilize the photocathode, which was

attributed to the formation of pin-holes between the Cu<sub>2</sub>O / TiO<sub>2</sub> interface due to non-uniform growth even using ALD. The insertion of ZnO between Cu<sub>2</sub>O and TiO<sub>2</sub> might provide a more uniform hydroxylated surface for TiO<sub>2</sub> to achieve conformal deposition. This demonstrates the important synthetic challenge of depositing pin-hole free protection layers to achieve long-term stability.

In addition, some carbon-based materials, such as graphene, have also been used to protect photoelectrodes like macroporous silicon wafers.<sup>104</sup> Zhang *et al.* reported carbon-protected Cu<sub>2</sub>O nanowire arrays that showed improved stability with a carbon layer compared with the bare nanowires.<sup>105</sup> The thin, uniform layer of carbon (20 nm) was deposited via the decomposition of a glucose solution on Cu<sub>2</sub>O at 550 °C in an N<sub>2</sub> atmosphere. The carbon-protected Cu<sub>2</sub>O also showed photocurrent enhancement from -2.28 mA/cm<sup>2</sup> to -3.95 mA/cm<sup>2</sup> at 0 V, and the photocurrent decay was inhibited from 87.4% to 19.3% over a 20 min stability test.

### **1.6.2 Kinetic protection layer**

As discussed above, catalysts are usually necessary to improve water oxidation and reduction performance no matter which semiconductors are studied as the photoelectrodes. Since the nature of photocorrosion is usually the reaction between semiconductors and photo-generated carriers in the presence of H<sub>2</sub>O, it should be effective to protect the material by transferring the photo-generated carriers from the semiconductor to the desired chemical reaction. Indeed, various OER and HER catalysts have been demonstrated to reduce the degree of photocorrosion (some examples have been discussed in section 1.5.5.4).

For example, ultrathin Ni metal (2 nm) films have been demonstrated to protect planar n-Si photoanodes.<sup>74</sup> The role of Ni was shown to form semiconductor-insulator-metal (Si-SiO<sub>2</sub>-Ni) junction to improve the charge separation of Si, as well as forming OER catalyst species on the surface. Combined with a potassium borate and lithium borate electrolyte, the integrated photoanode was shown to be stable against photocorrosion for 3 days. It was suspected that the Li<sup>+</sup> helped eliminate the formation of  $\alpha$ -phase Ni(OH)<sub>2</sub>, thus avoiding large volume expansion of Ni layers during the oxidation process and enhancing the stability.

One important factor limiting the protection ability of thin-film catalysts is the chemical instability of catalysts under operating conditions. To address this issue, Kuang *et al.* recently reported an *in-situ* regeneration method to deposit a NiFe-based OER catalyst on BiVO<sub>4</sub> to extend its stability.<sup>92</sup> With Ni as the substrate, the BiVO<sub>4</sub> photoanode showed gradual performance enhancement during the stability test in a borate buffer (pH 9). This was attributed to the formation of an amorphous NiFe-based catalyst (~ 5 nm), where the Ni<sup>2+</sup> comes from dissolution of the NiO and Ni(OH)<sub>2</sub> layers on the Ni substrate and the Fe<sup>x+</sup> species comes from impurities in the electrolyte. Long-term stability of over 1000 hours has been achieved, due to the regeneration of NiFe-based catalyst on BiVO<sub>4</sub> sites where the catalyst has been exfoliated or dissolved. Low concentration of Ni<sup>2+</sup> (< 1 $\mu$ M) and the borate electrolyte are key factors for this strategy. Higher concentration of Ni<sup>2+</sup> caused overloading of the catalyst to increase surface charge recombination, while the choice of other electrolytes, such as phosphate, accelerated the catalyst dissolution.

The application of catalysts as protection layers has its own limitations. First, the relatively slow kinetics of water oxidation and water reduction makes it difficult to fully inhibit the photocorrosion via kinetic control. Second, the stability of catalysts can be an issue. The stability includes both the structural stability of catalysts and their attachment to the substrate. Third, there are more and more reports indicating that porosity and ion-permeability is critical to achieve high-performance OER catalyst and form a favorable interface with semiconductors, such as the transition-metal-based (oxy)hydroxide. As a result, the contact between unstable semiconductors and water may not be completely avoided. Therefore, the combination of both types of protection layer may ultimately be the winning strategy to achieve optimized stability and performance of photoelectrodes.

## 1.7 THIN FILM CATALYSTS

The performance of thin film catalysts on photoelectrodes is not only affected by the electrocatalytic activity of the catalyst, but also by the interface between catalyst and semiconductor. Understanding along this direction is critical to design efficient photoelectrode systems. In addition, the problems introduced by the catalysts, such as the parasitic light absorption, need to be carefully considered in order to optimize the overall performance.

### 1.7.1 The role of catalysts on photoelectrodes

It has become widely recognized that catalysts are critical components in photoelectrode configurations in order to achieve high performance for both OER and HER. For OER, various catalysts including precious metal (e.g. Ir<sup>106-109</sup>) and transition metal (e.g. Co, Ni and Fe) oxides<sup>15, 85, 110</sup> and (oxy)hydroxides<sup>25, 30, 86, 111</sup> have been studied extensively and shown promising results. For HER, precious metal (e.g. Pt<sup>22, 89, 90</sup>) and transition metal based catalysts (e.g. MoS<sub>2</sub>,<sup>83, 91</sup> CoP,<sup>89</sup> etc.) have been employed. Many examples have been discussed in section 1.5. Despite the critical importance of the semiconductor-catalyst junction and the large number of studies investigating the behavior, the mechanism(s) concerning how the catalysts affect the performance remains a topic of current debate. One of the complications is that different synthetic methods of a given semiconductor can influence the behavior with a given catalyst, coupled with many different semiconductor materials and catalyst compositions that have been investigated using different methods. Below selected examples are summarized to unify the interpretations to present a general picture of the semiconductor / catalyst junction.

Typically, when semiconductors are coated with catalysts, either the turn-on potential or photocurrent density or both can be improved. From a fundamental perspective, the photocurrent density can be described by the following two equations (using a photoanode as the example).<sup>8</sup>

$$\frac{P_S}{P_S^0} = \exp\left(-\frac{q\Phi}{kT}\right) = \exp\left[-\frac{q(V_{app} + V_{ph} - V_{fb})}{kT}\right] \quad (1.6)$$

$$i_p = i_p^0 \left\{ \frac{P_S}{P_S^0} \exp\left(\frac{q\alpha_p \eta}{kT}\right) - \exp\left[-\frac{q(1-\alpha_p)\eta}{kT}\right] \right\} \quad (1.7)$$

In equation (1.6),  $P_s$  is the concentration of surface holes;  $P_s^0$  is the equilibrium concentration of surface holes;  $q$  is the charge of electrons;  $k$  is the Boltzmann constant;  $T$  is the temperature;  $\Phi$  is the magnitude of band bending, which is determined by the combination of applied potential ( $V_{app}$ ), photovoltage ( $V_{ph}$ , defined as the difference of Fermi level under dark and light conditions) and the flat-band potential ( $V_{fb}$ ). The equation (1.7) is derived from the Butler-Volmer equation assuming that charge transfer kinetics is dependent on the surface hole concentration. In equation (1.7),  $i_p$  is the photocurrent of holes under light;  $i_p^0$  is the exchange current under dark;  $\alpha_p$  is the hole transfer coefficient;  $\eta$  is the overpotential to drive the water oxidation reaction.

From those two equations, it is clear that the photocurrent generated from photoanodes is determined by a convolution of thermodynamic and kinetic factors (Figure 1.8). The extent of band bending at the semiconductor/electrolyte interface is determined by the band edge positions and photovoltage which controls the surface electron and hole concentrations. In addition, reduced hole/electron recombination on the surface can also increase the surface hole concentration. The photovoltage determines the position of the hole quasi-Fermi level, which must ultimately be sufficiently positive of the water oxidation formal potential to drive the reaction.

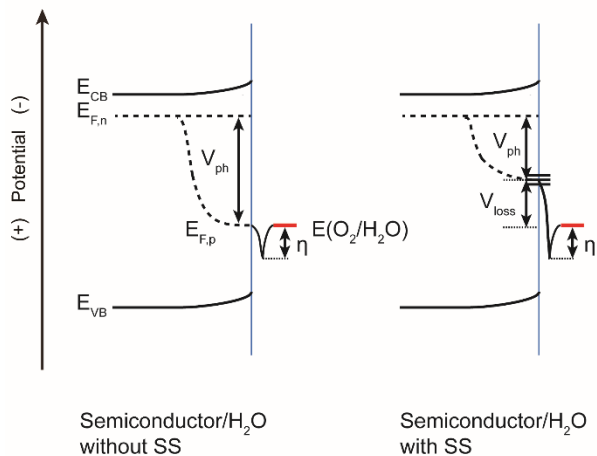


**Figure 1.8** The schematic shows that how the hole quasi Fermi level ( $E_{F,p}$ ) affected the performance of photoelectrodes. When there are no surface states (SS) on the semiconductor/liquid interface, the overpotential is mainly the kinetic overpotential ( $\eta$ ); when there are SS, recombination decreased the photovoltage, leading to increased overpotential ( $V_{loss}$ ).  $E_{F,n}$ : the electron quasi Fermi level.

Similarly, the turn-on potential, another important parameter to describe the photoelectrode performance, is affected by both thermodynamic and kinetic factors. Since the photovoltage determines position of the hole quasi-Fermi level, it also limits  $V_{on}$ . Therefore, reducing the overpotential of the reaction can further shift the  $V_{on}$  to its theoretical value. As a result, the “catalysts” on photoelectrodes can either serve the true catalyst to reduce the kinetic overpotential, as the conventionally defined, or tuning the surface energetics at the semiconductor/electrolyte interface, or both.

In order to understand the role of catalysts on semiconductor surfaces, various techniques have been applied, including transient absorption spectroscopy (TAS)<sup>112, 113</sup>, photoelectrochemical impedance spectroscopy (PEIS)<sup>106, 114-116</sup>, intensity modulated photocurrent spectroscopy (IMPS)<sup>88, 89, 106, 117, 118</sup>, dual-working-electrode (DWE) technique<sup>119-122</sup> and more recently potential-sensing electrochemical atomic force microscopy (PS-EC-AFM)<sup>123</sup>. With more and more evidence being discovered, the roles

of catalysts on the semiconductor surface become gradually clear. Here we reviewed thin-film semiconductor/catalyst systems that studied by different techniques, and corresponding conclusions to reveal the role of catalysts.

### 1.7.1.1 Transient absorption spectroscopy

Barroso *et al.* reported a TAS study on hematite photoanodes with different material added to modify the surface.<sup>113</sup> In one system,  $\text{CoO}_x$  was added to serve as the co-catalysts, while a  $\text{Ga}_2\text{O}_3$  overlayer was added in another system, which is electrocatalytically inert. Interestingly, a negative shift of  $V_{\text{on}}$  was observed in both cases. The TAS study under applied bias showed that both treatments increased the absorption signals attributed to long-lived holes, and the shift of signal amplitude was consistent with the negative shift of  $V_{\text{on}}$  observed in  $J$ - $V$  curves. From this, the authors concluded that both  $\text{CoO}_x$  and  $\text{Ga}_2\text{O}_3$  treatments likely passivate surface states thereby reducing electron/hole recombination and increasing the yield of long-lived holes at the electrode surface.

Similarly, Barroso *et al.* studied the role of Co-Pi, another widely used OER catalyst, on the surface of hematite photoanodes.<sup>112</sup> The electrodeposited Co-Pi on mesoporous hematite thin-film photoanodes also shifted the  $V_{\text{on}}$  to more negative values and increased the  $J_{\text{ph}}$  at 1.4 V by 0.1  $\text{mA}/\text{cm}^2$ . The TAS results in the absence of applied bias indicated the addition of Co-Pi significantly increased the lifetime of the transient signal by more than 3 orders of magnitude, with the half-life ( $t_{1/2}$ ) increased from  $\sim 15$   $\mu\text{s}$  to  $\sim 30$  ms. The authors interpreted this behavior as retarded charge recombination in hematite due to the formation of Schottky-type heterojunction between hematite and Co-Pi.

### 1.7.1.2 Photoelectrochemical impedance spectroscopy

PEIS has been widely used to measure the charge transfer processes of photoelectrodes. The key of PEIS lies in constructing meaningful equivalent circuit models that accurately describe the relevant charge-transfer processes which ultimately control the  $J$ - $V$  behavior. The development of appropriate equivalent circuit for photoelectrodes has been extensively investigated by Bisquert *et al.* during the past decade.<sup>114, 124-127</sup> By studying the PEIS results for the bare photoelectrodes and the one with catalyst on the surface, the role of catalysts can be clarified.

Klahr *et al.* studied hematite thin-film photoanodes grown via ALD with different thicknesses of cobalt phosphate (Co-Pi) as an OER catalyst.<sup>114</sup> To overcome complications in interpretation due to heterogeneity of mesoporous photoelectrodes and competitive light absorption by the catalysts, light was illuminated from the back side of FTO-glass substrates. It was found that the photocurrent and turn-on potential of hematite was improved when the thickness of Co-Pi increased. After fitting analysis in the corresponded equivalent circuit for Co-Pi decorated hematite, it was found that the capacitance for Co-Pi ( $C_{\text{Co-Pi}}$ ) increased and the charge transfer resistance from the Co-Pi layer ( $R_{\text{ct, Co-Pi}}$ ) decreased as the increased thickness of Co-Pi layer. Together with the transient photocurrent measurement and chopped light measurement, it was concluded that Co-Pi improved the performance of water oxidation by efficiently collecting and storing photogenerated holes from hematite. The increased charge separation was invoked to explain the improved performance as it led to reduced charge recombination at the semiconductor/electrolyte interface.

Riha *et al.* studied the effect of sub-monolayer  $\text{Co}(\text{OH})_2/\text{Co}_3\text{O}_4$  catalyst on the performance inverse-opal scaffolded hematite photoanode.<sup>115</sup> Deposition of only 1 ALD cycle, the sub-monolayer Co-based catalyst shifted the  $V_{\text{on}}$  by 200 mV and increased  $J_{\text{ph}}$  from 1.4 to 2.1  $\text{mA}/\text{cm}^2$  at 1.53 V. By performing the PEIS measurement on planar thin-film hematite photoanode and assuming the charge transfer occurred through the surface states, it was found the capacitance of surface states decreased after ALD modification when water oxidation occurred, indicating faster hole transfer resulting lower steady-state hole concentration. In addition, the charge transfer resistance from the surface states was much lower compared with the un-modified hematite. Together, these results were interpreted as the Co-based catalyst accelerating the hole transfer kinetics, thereby acting as the water oxidation catalyst in the conventional sense.

### 1.7.1.3 Intensity modulated photocurrent spectroscopy

The IMPS technique was developed by Peter *et al.* in late 1980s, which measures the phase shift in photocurrent in relation to a sinusoidal modulation of light intensity.<sup>128-131</sup> Several assumptions need to be satisfied in order to obtain meaningful IMPS data: (1) the surface hole concentration (taking a photoanode as the example) changes linearly with the light intensity; (2) the light intensity modulation is sufficiently low so that only the surface hole concentration is altered instead of the degree of band bending; (3) the reaction process is dominated by a single step kinetically and the surface hole concentration falls into the first-order reaction region. By analyzing the complex photocurrent as a function of light modulation frequency, the surface charge transfer rate constant ( $k_{\text{tran}}$ ) and surface charge recombination rate constant ( $k_{\text{rec}}$ ) can be derived, using which the charge transfer efficiency (TE,  $\text{TE} = k_{\text{tran}} / (k_{\text{tran}} + k_{\text{rec}})$ ) can be obtained. The rate

constants describe the charge transfer process on photoelectrode/electrolyte interface thermodynamically ( $k_{rec}$ ) and kinetically ( $k_{tran}$ ).

Du *et al.* found that decoration of a hematite surface with NiFeO<sub>x</sub> via a photochemical decomposition method could shift the  $V_{on}$  negatively by 400 mV.<sup>111</sup> Measurements of the photovoltage by comparing the open circuit potential in the dark and under illumination revealed that NiFeO<sub>x</sub> increased the photovoltage by reducing Fermi level pinning, which was caused by the hematite surface states. With the help of IMPS measurements, detailed kinetics parameters were extracted for the NiFeO<sub>x</sub>/hematite system.<sup>117</sup> By comparing the bare hematite and the one with NiFeO<sub>x</sub>, it was found that  $k_{tran}$  remained the same for both photoanodes at 1.1 V for water oxidation, but the one with NiFeO<sub>x</sub> showed lower  $k_{rec}$  compared with the bare one.<sup>117</sup> The result indicated that NiFeO<sub>x</sub> improved the water oxidation performance by reducing the surface charge recombination.

Li *et al.* studied the effect of two different Ir-based catalysts on the performance of hematite photoanode.<sup>106</sup> It was found the addition of either IrO<sub>x</sub> or a heterogenized molecular Ir catalyst on the hematite surface led to a negative shift of  $V_{on}$  and increased  $J_{ph}$  in 0.1 M KNO<sub>3</sub> (pH 1.01). While the IrO<sub>x</sub> was deposited on hematite as a dense thin film, the Ir molecular catalyst was anchored on the surface via the direct binding with Ir centers, with the molecular identity remained. IMPS study revealed that compared with the bare hematite, the IrO<sub>x</sub>-decorated one showed increased  $k_{tran}$  and decreased  $k_{rec}$ , while the one with the heterogenized molecular Ir catalyst showed only increased  $k_{tran}$  but similar  $k_{rec}$  as the bare one. By increasing the loading amount of these two catalysts, it was found that only  $k_{rec}$  increased for Ir molecular catalyst, while both  $k_{tran}$  and  $k_{rec}$  were

improved for IrO<sub>x</sub>. As a result, it was concluded that the application of Ir molecular catalyst provided additional hole transfer pathway while the surface recombination still occurs via surface states at the hematite/H<sub>2</sub>O interface. As a comparison, the IrO<sub>x</sub> dense thin film replaced the original hematite/H<sub>2</sub>O interface to reduce the charge recombination and increased the hole transfer at the same time.

In addition to hematite, IMPS studies have also been applied to other semiconductor/catalyst systems. For example, Zachäus *et al.* studied the influence of Co-Pi on the charge transfer processes on BiVO<sub>4</sub> photoanodes.<sup>118</sup> It was found that the performance of BiVO<sub>4</sub> was mainly limited by the surface charge recombination instead of water oxidation kinetics. By comparing the  $k_{tran}$  and  $k_{rec}$  of bare BiVO<sub>4</sub> and the one with Co-Pi, it was found that the addition of Co-Pi decreased the  $k_{rec}$  by a factor of 10-20 over the entire potential range (0.6-1.5 V), while the  $k_{tran}$  remained unchanged when the potential was less than 1 V. Furthermore, the addition of the efficient RuO<sub>x</sub> OER electrocatalyst decreased the performance because it failed to passivate the surface states on BiVO<sub>4</sub>. Moreover, Liu *et al.* reported the decoration ferrihydrite and Ni(OH)<sub>x</sub> as “hole-storage” layer on Ta<sub>3</sub>N<sub>5</sub> photoanode significantly increased its performance.<sup>88</sup> IMPS study revealed that the charge carrier lifetime was prolonged by 2 to 6 times after the hole-storage layer deposition. Meanwhile, the  $k_{rec}$  decreased dramatically while  $k_{tran}$  was not improved, indicating reducing surface recombination rather than enhancing surface hole transfer was the main function of such a hole-storage layer.

In addition to OER catalysts, the effect of HER catalysts on photocathodes has been studied via IMPS.<sup>89</sup> Using a Si photocathode with GaN nanowires grown on it, different HER catalysts were deposited including Pt, Ag and cobalt phosphide (CoP). It

was found that under all three cases the  $V_{\text{on}}$  and  $J_{\text{ph}}$  was improved and Pt was the most effective one, followed by CoP and Ag. The IMPS results revealed that adding Ag or Pt reduced  $k_{\text{rec}}$  by one order of magnitude over a wide range of potential window (even before  $V_{\text{on}}$ ), while adding CoP only reduced the  $k_{\text{rec}}$  after the turn-on potential. This indicated that CoP functioned as a HER catalyst quite differently from the metals on the semiconductor. For CoP, it couldn't accept the charge from the photocathode at low applied potential, leading to severe charge recombination and limited photovoltage. On the other hand, the metals (Pt or Ag) can extract the charge through the formation of Schottky junctions and reduce charge recombination. With further enhanced charge transfer kinetics, such as with Pt, the highest performance was achieved.

More details about using IMPS to study the interfacial charge transfer kinetics will be illustrated in Chapter 3 and Chapter 4.

#### **1.7.1.4 Dual-working-electrode technique**

In 2007 Peter employed a second evaporated Ti working electrode to sense the potential of TiO<sub>2</sub> nanoparticles away from the conductive substrate to establish working model of such electrodes used in dye-sensitized solar cells.<sup>132</sup> A similar dual working electrode (DWE) technique was used by Lin *et al.* for dense IrO<sub>x</sub> and ion-permeable Ni(OH)<sub>x</sub> OER catalysts integrated on TiO<sub>2</sub> photoanodes.<sup>119</sup> By depositing a thin layer of porous Au on the surface of the catalyst, without forming direct contact with the semiconductor, they were able to simultaneously sense and control the current and potential of both the TiO<sub>2</sub> semiconductor and the catalyst under working conditions. Unlike TA, EIS, IMPS methods which are indirect and model-dependent for results interpretation, the DWE offers a direct measure of the catalyst and the interpretation is less ambiguous.

It was found that the dense, ion-impermeable  $\text{IrO}_x$  formed a Schottky-type buried junction with  $\text{TiO}_2$ , leading the constant photovoltage of only 0.2 V, which explains the relatively poor performance of this system despite  $\text{IrO}_x$  as one of the best OER catalysts. However, since the  $\text{Ni(OH)}_x$  catalyst is ion-permeable, it can store charge via redox reactions of the Ni ions. Since oxidation of the Ni ions lowers to catalyst potential, the photovoltage of the junction with  $\text{TiO}_2$  increases and this is therefore termed an “adaptive junction”. Since the catalyst potential was measured directly, as well as the current at the catalyst which matched the current at  $\text{TiO}_2$ , it was concluded that hole transfer was efficient from  $\text{TiO}_2$  to  $\text{Ni(OH)}_x$  and the OER occurred primarily via the catalyst. As a result, improved turn-on potential and fill factor was observed for the  $\text{TiO}_2/\text{Ni(OH)}_x$  system.

Qiu *et al.* later reported the application of DWE technique on hematite photoanodes coated with the  $\text{Ni}_{0.8}\text{Fe}_{0.2}\text{O}_x$  catalyst where a thin layer of porous Au was deposited on the surface of  $\text{Ni}_{0.8}\text{Fe}_{0.2}\text{O}_x$  to form the second working electrode.<sup>121</sup> It was found that the conductivity of catalyst increased sharply after oxidation of the Ni species, no matter the catalyst was on conductive substrate (ITO) or hematite photoanode. By monitoring the photocurrent of hematite and the current of catalyst at the same time over a wide range of applied bias, it was found that hole transfer from hematite to the catalyst occurs with an efficiency up to 95%. This result indicates that the  $\text{Ni}_{0.8}\text{Fe}_{0.2}\text{O}_x$  not only serves as a hole-collecting contact but also as the catalyst to drive water oxidation. In addition, the authors found that the heterogeneity of the catalyst could affect the hole collection from semiconductor to the catalyst, which may explain the difference between various reported results for the role of catalyst.

Qiu *et al.* later reported the effect of semiconductor morphology and catalyst conductivity on the photoelectrode performance via the DWE technique.<sup>122</sup> Two types of hematite with different morphologies and two types of  $\text{NiFeO}_x\text{H}_y$  with different conductivities (as well as OER activity) were combined to illustrate the effect. Electrodeposited (ED) hematite on FTO substrates featured a porous morphology while the ALD electrode forms a compact, dense thin film.  $\text{Ni}_{0.8}\text{Fe}_{0.2}\text{O}_x\text{H}_y$  has better conductivity and OER activity compared with  $\text{Ni}_{0.2}\text{Fe}_{0.8}\text{O}_x\text{H}_y$ . However, the  $\text{Ni}_{0.2}\text{Fe}_{0.8}\text{O}_x\text{H}_y$  decorated ED hematite showed much worse performance than the one with  $\text{Ni}_{0.8}\text{Fe}_{0.2}\text{O}_x\text{H}_y$ , while the ALD hematite showed good performance after the deposition of both catalysts. By measuring the potential of the catalyst as a function of semiconductor potential, it was found that charge recombination due to the direct contact between the conductive catalyst and FTO substrate occurred which inhibited the performance. To avoid this shunting, photo-assisted electrodeposition of catalyst on ED hematite was carried to avoid the direct contact between FTO and catalyst, which shown much better performance compared with one deposited via photochemical decomposition. The study pointed out the importance to avoid shunting using porous semiconductors with catalysts, which could be achieved by photo-assisted electrodeposition method, or preventing the direct contact between catalyst and conductive substrate by inserting insulating layer or electronically insulating catalyst between them.

#### **1.7.1.5 Potential-sensing electrochemical atomic force microscopy**

Although the DWE technique can reveal the electrochemical information of catalyst layers during the reaction, its application is generally limited to planar photoelectrodes.

High-aspect-ratio substrates can lead to the non-uniform coverage of second working electrode layer, resulting in direct electrical shorting to the semiconductor. To overcome this problem, Nellist *et al* developed a method to use an electrochemical AFM to sense the local potential of catalysts on different morphologies of photoanodes.<sup>123</sup> In this configuration, an electrically insulated AFM cantilever was modified with a conductive nanotip of Pt. As a result, the tip-substrate interaction could be controlled by force feedback through cantilever deflection, so that the potential of substrate (the catalyst layer) could be detected without damaging the catalyst layer (Figure 1.9a).

The PS-EC-AFM was used to study the effect of Co-Pi on both planar and nanostructured hematite photoanodes. The tip potential didn't track the increase of substrate potential until the  $\text{Co}^{2+}$  ions were oxidized and the catalyst layer became conductive (Figure 1.9c). It was observed that similar tip potentials were achieved for both Co-Pi coated ITO substrate under dark and Co-Pi coated hematite photoanode under light when the current density was the same, indicating the photogenerated holes were transferred from hematite to Co-Pi layer to drive the water oxidation reaction (Figure 1.9b). Study for other semiconductor/catalyst systems based on this technique can be promising to further reveal the role of catalysts on the semiconductors.

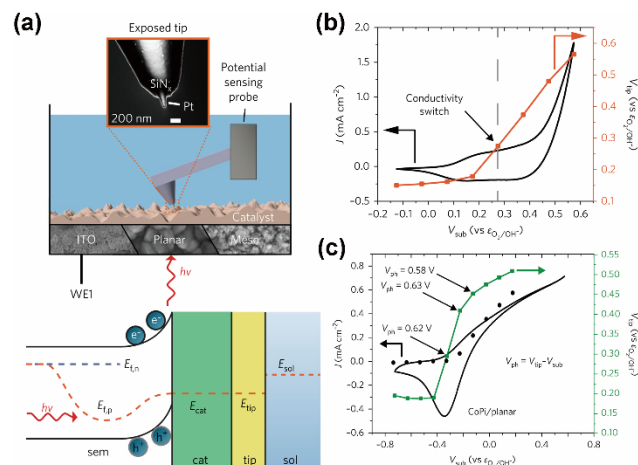


**Figure 1.9** (a) The schematic shows the electrochemical AFM set up to measure the catalyst potential during (photo)electrochemical water oxidation. The inset is a TEM image of the AFM tip. The band diagram shows the equilibrium of tip potential ( $E_{tip}$ ) with the catalyst potential ( $E_{cat}$ ) during the PEC measurement. (b) The J-V curve of Co-Pi coated ITO electrode in 0.1 M phosphate buffer (pH 6.9) and the corresponding tip potentials. (c) The J-V curve of Co-Pi coated planar hematite photoelectrode in the same electrolyte and the corresponded tip potentials. Light source: 405 nm light with 27 mW/cm<sup>2</sup>. A clear switching of tip potential was observed in both (b) and (c). (a-c) reproduced from “M. R. Nellist, F. A. L. Laskowski, J. Qiu, H. Hajibabaei, K. Sivula, T. W. Hamann and S. W. Boettcher, *Nat. Energy*, 2018, 3, 46-52.” with permission from Springer Nature.

## 1.7.2 The effect of catalysts on the light absorption

The loading amount of catalysts has a great impact on the water oxidation/reduction performance. In order to achieve the optimized performance, the catalyst loading is considerably high, which introduced another problem in photoelectrodes. That is, the usually opaque electrocatalysts compete with the underneath semiconductors in terms of light absorption. To avoid this competition, mainly two strategies have been employed in the literature: (1) decoupling the reaction sites with light absorption sites; (2) synthesis of catalysts with high intrinsic activity to reduce the loading amount, which will be transparent for the incident light.

### 1.7.2.1 Decoupling reaction sites and light absorption sites

The most convenient method to overcome competitive light absorption by the catalyst layer is to illuminate the photoelectrode from the back side (the ohmic contact side) instead of front side (the catalyst side). Such a method requires the deposition of semiconductor thin films on the transparent and conductive substrate, such as the conductive oxide coated glass (e.g., FTO and ITO). In addition, the thickness of semiconductors needs to be controlled so that the photo-generated carriers can reach the surface before recombination. For example, Du *et al.* synthesized the amorphous NiFeO<sub>x</sub> layer on the surface of ALD grown hematite (25 nm) via a photochemical decomposition method.<sup>111</sup> Due to the brown color of NiFeO<sub>x</sub>, it competed with the light absorption of hematite. With illumination from the back side of photoelectrode, the J<sub>ph</sub> at 1.23 V was enhanced by almost 70%. Similarly, Klahr *et al.* reported that Co-Pi decorated hematite thin film photoanode.<sup>114</sup> Since Co-Pi broadly absorbed visible light, back illumination was used so that the performance of hematite could be optimized by controlling the thickness of Co-Pi thin films.

Another method to achieve this goal is to selectively deposit the catalyst instead of a uniform deposition on the surface of photoelectrodes so that only a small portion of incident light will be blocked by the catalysts even under the front illumination. Such a strategy often requires the synthesis of high-aspect-ratio semiconductors. For example, Shaner *et al.* reported a Si microwire design consisting of Si microwire arrays with the height of 100 μm, 5-10 μm of Ni-Mo HER catalyst on the bottom of microwire, with additional 1-3 μm of light-scattering TiO<sub>2</sub> particles.<sup>133</sup> The light absorption was enabled by the exposed Si microwires, while the photo-generated carriers were transferred to Ni-

Mo HER catalyst on the bottom of microwires. The addition TiO<sub>2</sub> further enhanced the light absorption by light-scattering. In addition, Vijselaar *et al.* reported the selective deposition of Ni-Mo HER catalysts on the top of Si microwires.<sup>134</sup> The Si surface was first conformally covered with SiO<sub>2</sub>, followed by addition of a photoresist layer, which was etched in O<sub>2</sub> plasma to expose the top of wires. Then the exposed SiO<sub>2</sub> was etched away so that only the top of Si could be electrodeposited with Ni-Mo HER catalyst. Through the selective deposition, it was found the light absorption by Ni-Mo was inhibited compared with the one with fully exposed Si surface after the same catalyst deposition time. As a result, the  $J_{ph}$  was improved by over 6 times.

In addition, the decoupling of light absorption with photocatalytic activity can be achieved by changing the assembly method of semiconductors. For example, Kang *et al.* reported an epitaxial lift-off and printing-based assemblies to prepare the GaAs-based photocathode.<sup>14</sup> After removing from the growth substrate of GaAs wafers, the photocathode was sealed into transparent, photocurable polymer, which was further assembled onto glass substrate. As a result, the back ohmic contact layer was facing the electrolyte side, with Pt HER catalysts on it (Figure 1.7b). In this bifacial configuration, the light penetrated from the glass side while the electrons were collected on the backside to electrolyte.

### 1.7.2.2 Synthesis of transparent catalysts

There are limitations of using geometrical approaches to reduce the effect of light absorption by catalysts. For example, in conventional tandem cell configurations, it is critical to allow the light absorption by the smaller band gap photo absorber underneath the top absorber. Thus, light must pass through the top catalyst layer before reaching the

bottom cell. Therefore, a more ideal approach is to synthesize a transparent catalyst layer with high activity.

For instance, Morales-Guio *et al.* reported the synthesis of semi-transparent FeNiO<sub>x</sub> catalysts on hematite photoanodes via photo-assisted electrodeposition.<sup>135</sup> It was found that the oxidative deposition of NiO<sub>x</sub> in pH 5.3 was much slower due to faster corrosion of NiO<sub>x</sub> films, with Fe incorporation further accelerating the corrosion process. As a result, the loading amount of FeNiO<sub>x</sub> was low (4-7 nm in thickness), leading to low light absorption by the catalyst layer. In addition, the as-deposited FeNiO<sub>x</sub> featured a high turnover frequency (TOF) of 1.1 s<sup>-1</sup> with an overpotential of 0.35 V, which was almost 10 times of that for NiO<sub>x</sub> at the similar loading amount. The FeNiO<sub>x</sub> decorated hematite achieved higher  $J_{ph}$  and better  $V_{on}$  compared with the bare or NiO<sub>x</sub> -decorated hematite.

Another approach that has also been reported recently is to reduce the size of the catalyst to the atomic scale, which can result in improved intrinsic activity of the catalyst with high atomic efficiency and negligible light absorption. Zhao *et al.* recently reported the synthesis single-atom catalysts (SACs) and dinuclear heterogeneous catalysts (DHCs) of Ir on hematite photoanodes.<sup>109</sup> The DHCs were synthesized via the photochemical decomposition of the organic ligands in Ir homodimers, consisting of two Ir atoms per catalytic site in the form of Ir-O-Ir arrangement. The Ir DHCs decorated hematite showed the best  $V_{on}$  (0.55 V) and highest  $J_{ph}$  compared with Ir SACs and Ir nanoparticles in pH 6 electrolyte. The measured TOF for Ir DHCs is 2.6 and 5 times higher than the corresponding Ir SACs and nanoparticles. DFT calculation indicated that the energy required after the second proton-coupled electron transfer (PCET) process was much lower in DHCs compared with the Ir SACs. Similarly, DHCs of Ir was synthesized on

WO<sub>3</sub> photoanode, but with different bonding configuration compared with the one on  $\alpha$ -Fe<sub>2</sub>O<sub>3</sub> surfaces.<sup>108</sup> It was found that only one Ir atom was anchored on the WO<sub>3</sub> surface with second Ir atom on top of the first Ir (end on bonding), while two Ir atoms were anchored on the  $\alpha$ -Fe<sub>2</sub>O<sub>3</sub> surfaces. The difference comes from the density and distance of binding sites on different surfaces. In addition, the WO<sub>3</sub> photoanode coated with DHCs of Ir showed higher product selectivity for O<sub>2</sub> instead of peroxide species compared with bare WO<sub>3</sub> and the one coated with SACs of Ir, which was explained as more favorable water oxidation pathways having a second Ir site.

In addition to OER catalysts, synthesis of semi-transparent HER catalysts have also been explored. For instance, Roger *et al.* reported a hydrothermal synthesis method to deposit Co<sub>2</sub>Mo<sub>9</sub>S<sub>26</sub> thin films on FTO-coated glass from aqueous solution of cobalt sulfate, ammonia heptamolybdate and thiourea at 180 °C for 72 hours.<sup>136</sup> With a thickness of 300 nm, such a thin film showed a translucent nature, but it still delivered current densities of 10 mA/cm<sup>2</sup> at 260 mV overpotential in 0.5 M H<sub>2</sub>SO<sub>4</sub>. Furthermore, Ding *et al.* deposited amorphous MoS<sub>x</sub>Cl<sub>y</sub> catalysts on n<sup>+</sup>pp<sup>+</sup>-Si micropyramid photocathodes through a low temperature CVD method.<sup>137</sup> With a thickness between 40 and 60 nm, the MoS<sub>x</sub>Cl<sub>y</sub> catalysts showed little light absorption in the 500 to 1200 nm wavelength region where Si absorbs strongly. As a result, the integrated photocathode showed V<sub>on</sub> of 0.41 V and J<sub>ph</sub> of 43.0 mA/cm<sup>2</sup> at 0 V in 0.5 M H<sub>2</sub>SO<sub>4</sub>.

## 1.8 SUMMARY

Storing solar energy to overcome the intermittent nature of this abundant resource is of paramount importance to a future society that is primarily powered by renewable sources. PEC water splitting provides a promising route to solving this problem, but the solar hydrogen production technology, using PEC or other methods, is still far from being ready for commercialization. The critical issue lies in the development of photoelectrodes for harvesting solar energy and carrying out the desired chemical reactions efficiently and stably. Among them, thin-film photoelectrodes are unique thanks to features such as serving as a good model platform for fundamental understanding of important processes and the rich knowledge on thin-film materials. The strategies developed for thin-film materials with the purpose of overcoming challenges for efficient and inexpensive solar fuel synthesis are summarized.

A variety of synthetic methods have been applied to produce thin-film components of photoelectrodes including semiconductors, protection layers and catalysts. Those approaches can be categorized into physical vapor depositions, chemical depositions and (photo)electrochemical depositions, with corresponding advantages and caveats for each of them. How to balance the cost and material qualities would be a critical criterion to consider in choosing the suitable synthesis methods.

As the key component in thin-film photoelectrodes, the light absorbers have been explored using various semiconductors with different compositions, structures and morphologies. However, it is extremely difficult to find a single material that can meet all the needs. Common issues that limit the performance of a given material include light absorption, bulk/surface recombination, mismatch of energetics, instabilities and other

issues such as fabrication cost. Representative strategies to address those issues on prototypical materials are summarized. (1) To address the light absorption problems, two common strategies are usually applied, either to narrow down the band gaps by tuning the compositions, or to reduce the optical loss due to reflection. (2) To reduce the bulk recombination, nanostructuring is usually applied to overcome the short diffusion lengths, and doping is applied to decrease the minority carrier concentrations and improve the transport of the majority carriers. (3) The charge recombination on the surface can be addressed by depositing passivation layers or change the crystal structures at the surface. (4) To deal with the mismatch of energetics, buried junctions can be constructed or the band edge positions can be tuned, resulting larger photovoltage extractions. (5) The instability issue need to be considered from its origins, including the accumulation of by-products, the deactivation due to loss of photovoltages and corrosions. Different protection strategies corresponding to the origin of instabilities need to be applied. Among them, the deposition thin-film protection layers is the most widely used one, divided into physical barrier protection layers and kinetic protection layers.

Thin-film catalysts have been widely used to improve the performance of photoelectrodes. For better design and development of catalysts, a better understanding on their roles is critical but still missing. From a fundamental perspective, the catalysts should help to enhance the performance by either reducing the kinetic overpotentials or tuning the surface energetics at the semiconductor/electrolyte interfaces or both. A number of techniques have been developed that can be used to discern the various roles, including transient absorption spectroscopy (TAS), photoelectrochemical impedance spectroscopy (PEIS), intensity modulated photocurrent spectroscopy (IMPS), dual-

working-electrode (DWE) technique and potential-sensing electrochemical atomic force microscopy (PS-EC-AFM). In addition, to deal with the effect of catalysts on light absorption, two common strategies have been applied: (1) decoupling reaction sites and light absorption sites; (2) synthesis of transparent catalysts.

It is envisioned that further development of research on solar fuel synthesis will continue to demand and benefit from detailed understanding of the photoelectrode materials. New device engineering on using PEC for practical solar fuel synthesis will likely be needed, as well. Both aspects will require studies on model material systems that are thin-films in form factors. Such efforts will progress hand in hand with efforts aimed at understanding the catalysis, as well as new concepts of creative light utilization. Together, these efforts will see a convergence, where practical solutions to the grand challenge of artificial photosynthesis become possible.

## 1.9 REFERENCE

1. N. S. Lewis, *Science*, 2016, **351**, aad1920.
2. X. Yang, R. Liu, Y. He, J. Thorne, Z. Zheng and D. Wang, *Nano Res.*, 2015, **8**, 56-81.
3. P. J. Boddy, *J. Electrochem. Soc.*, 1968, **115**, 199-203.
4. A. Fujishima and K. Honda, *Nature*, 1972, **238**, 37-38.
5. M. G. Walter, E. L. Warren, J. R. McKone, S. W. Boettcher, Q. Mi, E. A. Santori and N. S. Lewis, *Chem. Rev.*, 2010, **110**, 6446-6473.
6. W. W. Gärtner, *Physical Review*, 1959, **116**, 84-87.
7. L. Peter, in *Photoelectrochemical Water Splitting: Materials, Processes and Architectures*, The Royal Society of Chemistry, 2013, pp. 19-51.
8. J. E. Thorne, S. Li, C. Du, G. Qin and D. Wang, *J. Phys. Chem. Lett.*, 2015, **6**, 4083-4088.
9. M. G. Mali, H. Yoon, B. N. Joshi, H. Park, S. S. Al-Deyab, D. C. Lim, S. Ahn, C. Nervi and S. S. Yoon, *ACS Appl. Mater. Interfaces*, 2015, **7**, 21619-21625.

10. H. Kumagai, T. Minegishi, N. Sato, T. Yamada, J. Kubota and K. Domen, *J. Mater. Chem. A*, 2015, **3**, 8300-8307.
11. M. Zhong, T. Hisatomi, Y. Sasaki, S. Suzuki, K. Teshima, M. Nakabayashi, N. Shibata, H. Nishiyama, M. Katayama, T. Yamada and K. Domen, *Angew. Chem. Int. Ed.*, 2017, **56**, 4739-4743.
12. B. AlOtaibi, H. P. T. Nguyen, S. Zhao, M. G. Kibria, S. Fan and Z. Mi, *Nano Lett.*, 2013, **13**, 4356-4361.
13. D. Bae, T. Pedersen, B. Seger, B. Iandolo, O. Hansen, P. C. K. Vesborg and I. Chorkendorff, *Catal. Today*, 2017, **290**, 59-64.
14. D. Kang, J. L. Young, H. Lim, W. E. Klein, H. Chen, Y. Xi, B. Gai, T. G. Deutsch and J. Yoon, *Nat. Energy*, 2017, **2**, 17043.
15. H.-P. Wang, K. Sun, S. Y. Noh, A. Kargar, M.-L. Tsai, M.-Y. Huang, D. Wang and J.-H. He, *Nano Lett.*, 2015, **15**, 2817-2824.
16. A. Kay, I. Cesar and M. Grätzel, *J. Am. Chem. Soc.*, 2006, **128**, 15714-15721.
17. J. Yoon, S. Jo, I. S. Chun, I. Jung, H.-S. Kim, M. Meitl, E. Menard, X. Li, J. J. Coleman, U. Paik and J. A. Rogers, *Nature*, 2010, **465**, 329-333.
18. D. Kang, S. Arab, S. B. Cronin, X. Li, J. A. Rogers and J. Yoon, *Appl. Phys. Lett.*, 2013, **102**, 253902.
19. Y. Lin, C. Battaglia, M. Boccard, M. Hettick, Z. Yu, C. Ballif, J. W. Ager and A. Javey, *Nano Lett.*, 2013, **13**, 5615-5618.
20. Y. Lin, S. Zhou, S. W. Sheehan and D. Wang, *J. Am. Chem. Soc.*, 2011, **133**, 2398-2401.
21. M. T. Mayer, C. Du and D. Wang, *J. Am. Chem. Soc.*, 2012, **134**, 12406-12409.
22. P. Dai, W. Li, J. Xie, Y. He, J. Thorne, G. McMahon, J. Zhan and D. Wang, *Angew. Chem. Int. Ed.*, 2014, **53**, 13493-13497.
23. M. T. McDowell, M. F. Lichterman, J. M. Spurgeon, S. Hu, I. D. Sharp, B. S. Brunshwig and N. S. Lewis, *J. Phys. Chem. C*, 2014, **118**, 19618-19624.
24. M. Zhong, T. Hisatomi, Y. Kuang, J. Zhao, M. Liu, A. Iwase, Q. Jia, H. Nishiyama, T. Minegishi, M. Nakabayashi, N. Shibata, R. Niishiro, C. Katayama, H. Shibano, M. Katayama, A. Kudo, T. Yamada and K. Domen, *J. Am. Chem. Soc.*, 2015, **137**, 5053-5060.
25. J.-W. Jang, C. Du, Y. Ye, Y. Lin, X. Yao, J. Thorne, E. Liu, G. McMahon, J. Zhu, A. Javey, J. Guo and D. Wang, *Nat. Commun.*, 2015, **6**, 7447.
26. M. Ma, K. Zhang, P. Li, M. S. Jung, M. J. Jeong and J. H. Park, *Angew. Chem. Int. Ed.*, 2016, **55**, 11819-11823.
27. W. Yang, Y. Oh, J. Kim, M. J. Jeong, J. H. Park and J. Moon, *ACS Energy Lett.*, 2016, **1**, 1127-1136.
28. G. Liu, J. Shi, F. Zhang, Z. Chen, J. Han, C. Ding, S. Chen, Z. Wang, H. Han and C. Li, *Angew. Chem. Int. Ed.*, 2014, **53**, 7295-7299.
29. L. Wang, F. Dionigi, N. T. Nguyen, R. Kirchgeorg, M. Gliech, S. Grigorescu, P. Strasser and P. Schmuki, *Chem. Mater.*, 2015, **27**, 2360-2366.
30. L. Cai, J. Zhao, H. Li, J. Park, I. S. Cho, H. S. Han and X. Zheng, *ACS Energy Lett.*, 2016, **1**, 624-632.
31. D. Kang, T. W. Kim, S. R. Kubota, A. C. Cardiel, H. G. Cha and K.-S. Choi, *Chem. Rev.*, 2015, **115**, 12839-12887.

32. I. A. Digdaya, P. P. Rodriguez, M. Ma, G. W. P. Adhyaksa, E. C. Garnett, A. H. M. Smets and W. A. Smith, *J. Mater. Chem. A*, 2016, **4**, 6842-6852.
33. L. Pan, J. H. Kim, M. T. Mayer, M.-K. Son, A. Ummadisingu, J. S. Lee, A. Hagfeldt, J. Luo and M. Grätzel, *Nat. Catal.*, 2018, **1**, 412-420.
34. W. Liu, H. Liu, L. Dang, H. Zhang, X. Wu, B. Yang, Z. Li, X. Zhang, L. Lei and S. Jin, *Adv. Funct. Mater.*, 2017, **27**.
35. T. W. Kim and K.-S. Choi, *Science*, 2014, **343**, 990-994.
36. T. Hisatomi, J. Kubota and K. Domen, *Chem. Soc. Rev.*, 2014, **43**, 7520-7535.
37. A. Kudo and Y. Miseki, *Chem. Soc. Rev.*, 2009, **38**, 253-278.
38. X. Chen, S. Shen, L. Guo and S. S. Mao, *Chem. Rev.*, 2010, **110**, 6503-6570.
39. J. R. Bolton, S. J. Strickler and J. S. Connolly, *Nature*, 1985, **316**, 495-500.
40. X. Chen, L. Liu and F. Huang, *Chem. Soc. Rev.*, 2015, **44**, 1861-1885.
41. C. Yang, Z. Wang, T. Lin, H. Yin, X. Lü, D. Wan, T. Xu, C. Zheng, J. Lin, F. Huang, X. Xie and M. Jiang, *J. Am. Chem. Soc.*, 2013, **135**, 17831-17838.
42. M. G. Kibria and Z. Mi, *J. Mater. Chem. A*, 2016, **4**, 2801-2820.
43. A. Theuwis, K. Strubbe, L. M. Depestel and W. P. Gomes, *J. Electrochem. Soc.*, 2002, **149**, E173-E178.
44. M. G. Kibria, R. Qiao, W. Yang, I. Boukahil, X. Kong, F. A. Chowdhury, M. L. Trudeau, W. Ji, H. Guo, F. J. Himpsel, L. Vayssieres and Z. Mi, *Adv. Mater.*, 2016, **28**, 8388-8397.
45. Y. J. Hwang, A. Boukai and P. Yang, *Nano Lett.*, 2008, **9**, 410-415.
46. E. Garnett and P. Yang, *Nano Lett.*, 2010, **10**, 1082-1087.
47. J. R. Maiolo, B. M. Kayes, M. A. Filler, M. C. Putnam, M. D. Kelzenberg, H. A. Atwater and N. S. Lewis, *J. Am. Chem. Soc.*, 2007, **129**, 12346-12347.
48. P. Dai, J. Xie, M. T. Mayer, X. Yang, J. Zhan and D. Wang, *Angew. Chem. Int. Ed.*, 2013, **52**, 11119-11123.
49. Y. Qiu, W. Liu, W. Chen, W. Chen, G. Zhou, P.-C. Hsu, R. Zhang, Z. Liang, S. Fan, Y. Zhang and Y. Cui, *Sci. Adv.*, 2016, **2**, e1501764.
50. X. Shi, H. Jeong, S. J. Oh, M. Ma, K. Zhang, J. Kwon, I. T. Choi, I. Y. Choi, H. K. Kim, J. K. Kim and J. H. Park, *Nat. Commun.*, 2016, **7**, 11943.
51. I. Cesar, K. Sivula, A. Kay, R. Zboril and M. Grätzel, *J. Phys. Chem. C*, 2009, **113**, 772-782.
52. J. H. Kennedy and K. W. Frese, *J. Electrochem. Soc.*, 1978, **125**, 709-714.
53. P. E. de Jongh, D. Vanmaekelbergh and J. J. Kelly, *Chem. Mater.*, 1999, **11**, 3512-3517.
54. C. J. Engel, T. A. Polson, J. R. Spado, J. M. Bell and A. Fillinger, *J. Electrochem. Soc.*, 2008, **155**, F37-F42.
55. J. Luo, L. Steier, M.-K. Son, M. Schreier, M. T. Mayer and M. Grätzel, *Nano Lett.*, 2016, **16**, 1848-1857.
56. Y. Li, T. Takata, D. Cha, K. Takanabe, T. Minegishi, J. Kubota and K. Domen, *Adv. Mater.*, 2013, **25**, 125-131.
57. Y. Li, L. Zhang, A. Torres-Pardo, J. M. González-Calbet, Y. Ma, P. Oleynikov, O. Terasaki, S. Asahina, M. Shima, D. Cha, L. Zhao, K. Takanabe, J. Kubota and K. Domen, *Nat. Commun.*, 2013, **4**, 2566.
58. A. Ziani, E. Nurlaela, D. S. Dhawale, D. A. Silva, E. Alarousu, O. F. Mohammed and K. Takanabe, *Phys. Chem. Chem. Phys.*, 2015, **17**, 2670-2677.

59. M. de Respinis, M. Fravventura, F. F. Abdi, H. Schreuders, T. J. Savenije, W. A. Smith, B. Dam and R. van de Krol, *Chem. Mater.*, 2015, **27**, 7091-7099.
60. J. Y. Kim, G. Magesh, D. H. Youn, J.-W. Jang, J. Kubota, K. Domen and J. S. Lee, *Sci. Rep.*, 2013, **3**, 2681.
61. W. Li, P. Da, Y. Zhang, Y. Wang, X. Lin, X. Gong and G. Zheng, *ACS Nano*, 2014, **8**, 11770-11777.
62. S. P. Berglund, A. J. E. Rettie, S. Hoang and C. B. Mullins, *Phys. Chem. Chem. Phys.*, 2012, **14**, 7065-7075.
63. L. Han, I. A. Digdaya, T. W. F. Buijs, F. F. Abdi, Z. Huang, R. Liu, B. Dam, M. Zeman, W. A. Smith and A. H. M. Smets, *J. Mater. Chem. A*, 2015, **3**, 4155-4162.
64. H. Dotan, K. Sivula, M. Grätzel, A. Rothschild and S. C. Warren, *Energy Environ. Sci.*, 2011, **4**, 958-964.
65. D. K. Zhong, S. Choi and D. R. Gamelin, *J. Am. Chem. Soc.*, 2011, **133**, 18370-18377.
66. Y. Gao and T. W. Hamann, *Chem. Commun.*, 2017, **53**, 1285-1288.
67. T. Hisatomi, J. Brillet, M. Cornuz, F. Le Formal, N. Tetreault, K. Sivula and M. Gratzel, *Faraday Discuss.*, 2012, **155**, 223-232.
68. M. Li, J. Deng, A. Pu, P. Zhang, H. Zhang, J. Gao, Y. Hao, J. Zhong and X. Sun, *J. Mater. Chem. A*, 2014, **2**, 6727-6733.
69. J. Zhang, X. Chang, C. Li, A. Li, S. Liu, T. Wang and J. Gong, *J. Mater. Chem. A*, 2018, **6**, 3350-3354.
70. M. Gratzel, *Nature*, 2001, **414**, 338-344.
71. S. Hu, M. R. Shaner, J. A. Beardslee, M. Lichterman, B. S. Brunshwig and N. S. Lewis, *Science*, 2014, **344**, 1005-1009.
72. C. Li, T. Hisatomi, O. Watanabe, M. Nakabayashi, N. Shibata, K. Domen and J.-J. Delaunay, *Energy Environ. Sci.*, 2015, **8**, 1493-1500.
73. I. A. Digdaya, L. Han, T. W. F. Buijs, M. Zeman, B. Dam, A. H. M. Smets and W. A. Smith, *Energy Environ. Sci.*, 2015, **8**, 1585-1593.
74. M. J. Kenney, M. Gong, Y. Li, J. Z. Wu, J. Feng, M. Lanza and H. Dai, *Science*, 2013, **342**, 836-840.
75. J. Augustynski, R. Solaraska, H. Hagemann and C. Santato, *Proc. SPIE*, 2006, **6340**, 63400J.
76. R. S. Lillard, G. S. Kanner and D. P. Butt, *J. Electrochem. Soc.*, 1998, **145**, 2718-2725.
77. J. A. Seabold and K.-S. Choi, *Chem. Mater.*, 2011, **23**, 1105-1112.
78. S. Wang, H. Chen, G. Gao, T. Butburee, M. Lyu, S. Thaweesak, J.-H. Yun, A. Du, G. Liu and L. Wang, *Nano Energy*, 2016, **24**, 94-102.
79. Y. He, J. E. Thorne, C. H. Wu, P. Ma, C. Du, Q. Dong, J. Guo and D. Wang, *Chem*, 2016, **1**, 640-655.
80. F. M. Toma, J. K. Cooper, V. Kunzelmann, M. T. McDowell, J. Yu, D. M. Larson, N. J. Borys, C. Abelyan, J. W. Beeman, K. M. Yu, J. Yang, L. Chen, M. R. Shaner, J. Spurgeon, F. A. Houle, K. A. Persson and I. D. Sharp, *Nat. Commun.*, 2016, **7**, 12012.
81. E. Verlage, S. Hu, R. Liu, R. J. R. Jones, K. Sun, C. Xiang, N. S. Lewis and H. A. Atwater, *Energy Environ. Sci.*, 2015, **8**, 3166-3172.

82. J. Gu, Y. Yan, J. L. Young, K. X. Steirer, N. R. Neale and J. A. Turner, *Nat. Mater.*, 2016, **15**, 456-460.
83. J. Gu, J. A. Aguiar, S. Ferrere, K. X. Steirer, Y. Yan, C. Xiao, James L. Young, M. Al-Jassim, N. R. Neale and J. A. Turner, *Nat. Energy*, 2017, **2**, 16192.
84. A. Paracchino, V. Laporte, K. Sivula, M. Grätzel and E. Thimsen, *Nat. Mater.*, 2011, **10**, 456-461.
85. W. Qin, N. Wang, T. Yao, S. Wang, H. Wang, Y. Cao, S. Liu and C. Li, *ChemSusChem*, 2015, **8**, 3987-3991.
86. Y. He, P. Ma, S. Zhu, M. Liu, Q. Dong, J. Espano, X. Yao and D. Wang, *Joule*, 2017, **1**, 831-842.
87. G. Liu, P. Fu, L. Zhou, P. Yan, C. Ding, J. Shi and C. Li, *Chem. Eur. J.*, 2015, **21**, 9624-9628.
88. G. Liu, S. Ye, P. Yan, F.-Q. Xiong, P. Fu, Z. Wang, Z. Chen, J. Shi and C. Li, *Energy Environ. Sci.*, 2016, **9**, 1327-1334.
89. J. E. Thorne, Y. Zhao, D. He, S. Fan, S. Vanka, Z. Mi and D. Wang, *Phys. Chem. Chem. Phys.*, 2017, **19**, 29653-29659.
90. Y. F. Tay, H. Kaneko, S. Y. Chiam, S. Lie, Q. Zheng, B. Wu, S. S. Hadke, Z. Su, P. S. Bassi, D. Bishop, T. C. Sum, T. Minegishi, J. Barber, K. Domen and L. H. Wong, *Joule*, 2018, **2**, 537-548.
91. R. J. Britto, J. D. Benck, J. L. Young, C. Hahn, T. G. Deutsch and T. F. Jaramillo, *J. Phys. Chem. Lett.*, 2016, **7**, 2044-2049.
92. Y. Kuang, Q. Jia, G. Ma, T. Hisatomi, T. Minegishi, H. Nishiyama, M. Nakabayashi, N. Shibata, T. Yamada, A. Kudo and K. Domen, *Nat. Energy*, 2016, **2**, 16191.
93. D. K. Lee and K.-S. Choi, *Nat. Energy*, 2018, **3**, 53-60.
94. A. L. Greenaway, J. W. Boucher, S. Z. Oener, C. J. Funch and S. W. Boettcher, *ACS Energy Lett.*, 2017, **2**, 2270-2282.
95. J. S. Ward, T. Remo, K. Horowitz, M. Woodhouse, B. Sopori, K. VanSant and P. Basore, *Prog. Photovolt. Res. Appl.*, 2016, **24**, 1284-1292.
96. J. L. Young, M. A. Steiner, H. Döscher, R. M. France, J. A. Turner and Todd G. Deutsch, *Nat. Energy*, 2017, **2**, 17028.
97. F. L. Formal, M. Grätzel and K. Sivula, *Adv. Funct. Mater.*, 2010, **20**, 1099-1107.
98. O. Zandi, B. M. Klahr and T. W. Hamann, *Energy Environ. Sci.*, 2013, **6**, 634-642.
99. S. Hu, N. S. Lewis, J. W. Ager, J. Yang, J. R. McKone and N. C. Strandwitz, *J. Phys. Chem. C*, 2015, **119**, 24201-24228.
100. D. Bae, B. Seger, P. C. K. Vesborg, O. Hansen and I. Chorkendorff, *Chem. Soc. Rev.*, 2017, **46**, 1933-1954.
101. Y.-H. Lai, H. S. Park, J. Z. Zhang, P. D. Matthews, D. S. Wright and E. Reisner, *Chem. Eur. J.*, 2015, **21**, 3919-3923.
102. R. C. Kainthla, B. Zelenay and J. O. M. Bockris, *J. Electrochem. Soc.*, 1986, **133**, 248-253.
103. D. Bae, T. Pedersen, B. Seger, M. Malizia, A. Kuznetsov, O. Hansen, I. Chorkendorff and P. C. K. Vesborg, *Energy Environ. Sci.*, 2015, **8**, 650-660.
104. H. Yu, S. Chen, X. Fan, X. Quan, H. Zhao, X. Li and Y. Zhang, *Angew. Chem. Int. Ed.*, 2010, **49**, 5106-5109.

105. Z. Zhang, R. Dua, L. Zhang, H. Zhu, H. Zhang and P. Wang, *ACS Nano*, 2013, **7**, 1709-1717.
106. W. Li, D. He, S. W. Sheehan, Y. He, J. E. Thorne, X. Yao, G. W. Brudvig and D. Wang, *Energy Environ. Sci.*, 2016, **9**, 1794-1802.
107. W. Li, S. W. Sheehan, D. He, Y. He, X. Yao, R. L. Grimm, G. W. Brudvig and D. Wang, *Angew. Chem. Int. Ed.*, 2015, **54**, 11428-11432.
108. Y. Zhao, X. Yan, K. R. Yang, S. Cao, Q. Dong, J. E. Thorne, K. L. Materna, S. Zhu, X. Pan, M. Flytzani-Stephanopoulos, G. W. Brudvig, V. S. Batista and D. Wang, *ACS Cent. Sci.*, 2018, **4**, 1166-1172.
109. Y. Zhao, K. R. Yang, Z. Wang, X. Yan, S. Cao, Y. Ye, Q. Dong, X. Zhang, J. E. Thorne, L. Jin, K. L. Materna, A. Trimpalis, H. Bai, S. C. Fakra, X. Zhong, P. Wang, X. Pan, J. Guo, M. Flytzani-Stephanopoulos, G. W. Brudvig, V. S. Batista and D. Wang, *Proc. Natl. Acad. Sci. U.S.A.*, 2018, **115**, 2902-2907.
110. J. Seo, T. Takata, M. Nakabayashi, T. Hisatomi, N. Shibata, T. Minegishi and K. Domen, *J. Am. Chem. Soc.*, 2015, **137**, 12780-12783.
111. C. Du, X. Yang, M. T. Mayer, H. Hoyt, J. Xie, G. McMahon, G. Bischofing and D. Wang, *Angew. Chem. Int. Ed.*, 2013, **52**, 12692-12695.
112. M. Barroso, A. J. Cowan, S. R. Pendlebury, M. Grätzel, D. R. Klug and J. R. Durrant, *J. Am. Chem. Soc.*, 2011, **133**, 14868-14871.
113. M. Barroso, C. A. Mesa, S. R. Pendlebury, A. J. Cowan, T. Hisatomi, K. Sivula, M. Grätzel, D. R. Klug and J. R. Durrant, *Proc. Natl. Acad. Sci. U.S.A.*, 2012, **109**, 15640-15645.
114. B. Klahr, S. Gimenez, F. Fabregat-Santiago, J. Bisquert and T. W. Hamann, *J. Am. Chem. Soc.*, 2012, **134**, 16693-16700.
115. S. C. Riha, B. M. Klahr, E. C. Tyo, S. Seifert, S. Vajda, M. J. Pellin, T. W. Hamann and A. B. F. Martinson, *ACS Nano*, 2013, **7**, 2396-2405.
116. G. M. Carroll and D. R. Gamelin, *J. Mater. Chem. A*, 2016, **4**, 2986-2994.
117. J. E. Thorne, J.-W. Jang, E. Y. Liu and D. Wang, *Chem. Sci.*, 2016, **7**, 3347-3354.
118. C. Zachaus, F. F. Abdi, L. M. Peter and R. van de Krol, *Chem. Sci.*, 2017, **8**, 3712-3719.
119. F. Lin and S. W. Boettcher, *Nat. Mater.*, 2014, **13**, 81-86.
120. M. R. Nellist, F. A. L. Laskowski, F. Lin, T. J. Mills and S. W. Boettcher, *Acc. Chem. Res.*, 2016, **49**, 733-740.
121. J. Qiu, H. Hajibabaei, M. R. Nellist, F. A. L. Laskowski, T. W. Hamann and S. W. Boettcher, *ACS Cent. Sci.*, 2017, **3**, 1015-1025.
122. J. Qiu, H. Hajibabaei, M. R. Nellist, F. A. L. Laskowski, S. Z. Oener, T. W. Hamann and S. W. Boettcher, *ACS Energy Lett.*, 2018, **3**, 961-969.
123. M. R. Nellist, F. A. L. Laskowski, J. Qiu, H. Hajibabaei, K. Sivula, T. W. Hamann and S. W. Boettcher, *Nat. Energy*, 2018, **3**, 46-52.
124. L. Bertoluzzi and J. Bisquert, *J. Phys. Chem. Lett.*, 2012, **3**, 2517-2522.
125. B. Klahr, S. Gimenez, F. Fabregat-Santiago, J. Bisquert and T. W. Hamann, *Energy Environ. Sci.*, 2012, **5**, 7626-7636.
126. B. Klahr, S. Gimenez, F. Fabregat-Santiago, T. Hamann and J. Bisquert, *J. Am. Chem. Soc.*, 2012, **134**, 4294-4302.
127. J. Bisquert, L. Bertoluzzi, I. Mora-Sero and G. Garcia-Belmonte, *J. Phys. Chem. C*, 2014, **118**, 18983-18991.

128. L. M. Peter, *Chem. Rev.*, 1990, **90**, 753-769.
129. E. A. Ponomarev and L. M. Peter, *J. Electroanal. Chem.*, 1995, **396**, 219-226.
130. E. A. Ponomarev and L. M. Peter, *J. Electroanal. Chem.*, 1995, **397**, 45-52.
131. L. M. Peter, E. A. Ponomarev and D. J. Fermín, *J. Electroanal. Chem.*, 1997, **427**, 79-96.
132. L. M. Peter, *J. Phys. Chem. C*, 2007, **111**, 6601-6612.
133. M. R. Shaner, J. R. McKone, H. B. Gray and N. S. Lewis, *Energy Environ. Sci.*, 2015, **8**, 2977-2984.
134. W. Vijselaar, P. Westerik, J. Veerbeek, R. M. Tiggelaar, E. Berenschot, N. R. Tas, H. Gardeniers and J. Huskens, *Nat. Energy*, 2018, **3**, 185-192.
135. C. G. Morales-Guio, M. T. Mayer, A. Yella, S. D. Tilley, M. Grätzel and X. Hu, *J. Am. Chem. Soc.*, 2015, **137**, 9927-9936.
136. I. Roger, R. Moca, H. N. Miras, K. G. Crawford, D. A. J. Moran, A. Y. Ganin and M. D. Symes, *J. Mater. Chem. A*, 2017, **5**, 1472-1480.
137. Q. Ding, J. Zhai, M. Cabán - Acevedo, M. J. Shearer, L. Li, H. C. Chang, M. L. Tsai, D. Ma, X. Zhang, R. J. Hamers, J. H. He and S. Jin, *Adv. Mater.*, 2015, **27**, 6511-6518.

Section 1.3 to 1.8 is partially adapted with permission from “Y. He, T. Hamann and D. Wang, *Chem. Soc. Rev.*, 2019, **48**, 2182-2215.” Copyright 2019 Royal Society of Chemistry.

## CHAPTER 2 WHAT LIMITS THE PERFORMANCE OF TANTALUM NITRIDE FOR SOLAR WATER SPLITTING?

### 2.1 TANTALUM NITRIDE PHOTOANODE AS A PROTOTYPICAL PLATFORM FOR WATER OXIDATION

Solar water splitting has received significant attention as a promising route to direct solar energy harvesting and storage.<sup>1</sup> A key challenge that prevents its development into a practical technology is the availability of efficient *and* inexpensive photoactive materials.<sup>2</sup> Based on the considerations of light absorption, charge separation, charge transfer, and stability, the issues that limit the performance of photoactive materials may be categorized into five groups (Figure 2.1), and the strategies to tackle those problems have been summarized in Chapter 1. First, narrow light absorption within the solar spectrum makes it difficult to achieve high photocurrents on a number of otherwise highly promising materials. One of the best examples in this category is TiO<sub>2</sub>, which exhibits desired properties in almost every aspect for solar water splitting other than broad light absorption (TiO<sub>2</sub> only absorbs in the UV region).<sup>3</sup> Second, shallow space charge region is a critical issue faced by materials such as pyrite (FeS<sub>2</sub>). Third, strong bulk recombination is perhaps the most investigated issue within the field of solar-to-chemical energy conversion. It is a common challenge shared by a large number of

materials, especially metal oxides (e.g.,  $\text{Fe}_2\text{O}_3$ ).<sup>4-6</sup> Fourth, poor stability due to photocorrosion is a common issue faced by many semiconductors that are efficient at converting light to electricity, such as GaAs and GaP.<sup>7,8</sup> Fifth, poor stability due to non-corrosion surface chemical reactions is yet another mechanism that contributes to the degradation of photoelectrodes. While the behavior (i.e., rapid decay of water splitting performance) appears to be similar to photocorrosion, the non-corrosion nature makes the issue unique. Such a nature provides opportunities to tackle the problem differently from brute force passivation used to stabilize photoelectrodes such as GaP.<sup>9</sup> Most importantly, the issue due to non-corrosion surface chemical reactions has received little attention previously and is a missing link in the understanding of photoactive materials for solar-to-chemical energy conversion research. To make up for the deficiency, here we present a systematic study focusing on the last issue.

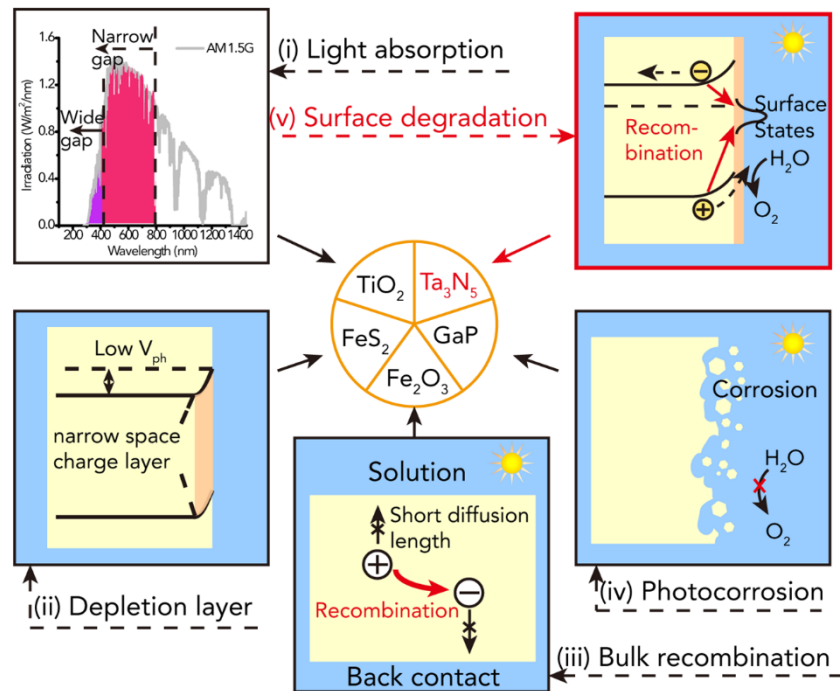


**Figure 2.1** Schematics of the main issues that limit the performance of photoactive materials for solar water splitting. The representative materials corresponding to each issue are shown in the center.

The prototypical material platform we chose for the present study is Ta<sub>3</sub>N<sub>5</sub>. It features a direct bandgap of 2.1 eV and promises high photocurrent densities, which has been recently realized experimentally by Li *et al.*<sup>10-12</sup> A record photocurrent current density of 12.1 mA/cm<sup>2</sup> at 1.23 V vs. reversible hydrogen electrode (RHE; unless noted, all voltages in Chapter 2 are vs. RHE) was reported.<sup>12</sup> This impressive progress notwithstanding, Ta<sub>3</sub>N<sub>5</sub> still faces two critical issues, namely low photovoltage and poor stability. The low photovoltage is manifested as the late turn-on potentials ( $V_{on}$ ; the lowest potential at which non-zero photocurrent is measured), typically >0.6 V.<sup>11-16</sup> Given that the conduction band minimum ( $E_{CB}$ ) of Ta<sub>3</sub>N<sub>5</sub> has been predicted by density functional theory (DFT) calculations to be more negative than water reduction potential, the reported  $V_{on}$ 's are unreasonably high.<sup>17, 18</sup> Significant efforts have been attracted to address the issue. For instance, Domen *et al.* recently improved the  $V_{on}$  to 0.55 V through a combination of doping and surface treatment.<sup>19</sup> Nevertheless, the true reasons behind the poor performance in terms of photovoltages remain poorly understood. Similarly, little is known about the degradation mechanism. For instance, without passivation, the photocurrent of Ta<sub>3</sub>N<sub>5</sub> would decrease >50% within the first few minutes of water splitting reactions.<sup>11, 20</sup> It has not been discussed previously in detail how the degradation is related to the photo-oxidation of Ta<sub>3</sub>N<sub>5</sub>.<sup>11, 20-22</sup> Here we show that these two critical issues are intimately connected. Most strikingly, through systematic photoelectrochemical (PEC) and X-ray spectroscopic studies, we discovered that photo-oxidation of Ta<sub>3</sub>N<sub>5</sub> is self-limiting and not the direct origin of the performance degradation. Instead, surface Fermi level pinning due to the thin oxidation formation

plays a key role in defining the photovoltage and stability. A quantitative correlation between the extent of surface oxidation and the degree of Fermi level pinning was established. The new insight permitted us to develop a strategy to improve the performance of Ta<sub>3</sub>N<sub>5</sub> using ultra-thin MgO grown by ALD, coupled with nickel-iron oxyhydroxide (NiFeOOH) oxygen evolution reaction catalysts.

## 2.2 MATERIALS AND METHODS

### 2.2.1 Material synthesis

The Ta<sub>3</sub>N<sub>5</sub> nanotubes were synthesized through the anodization of Ta foil to form tantalum oxide nanotubes followed by a post annealing in NH<sub>3</sub> to form tantalum nitride based on a modified procedure reported previously.<sup>23</sup> For the anodization procedure, tantalum foil (0.127 mm thick, Alfa Aesar) was firstly cut into 1cm x 4cm pieces. Then one side of the Ta foil was roughened using sandpaper for about 10 min. After the roughening, the Ta foil was cleaned by ultrasonication in acetone, methanol, isopropanol as well as deionized (DI) water and dried by flowing air. The electrolyte for anodization was made by mixing 38 mL sulfuric acid (95-98%, Sigma-Aldrich), 0.4 mL hydrofluoric acid (48%, Sigma-Aldrich) and 1.6 mL DI water with vigorous stirring during preparation. The Ta foil was anodized with a Pt gauze as the counter electrode at 60 V DC bias for 10 min without stirring. After thoroughly washing with ethanol and DI water, the as-prepared tantalum oxide nanotubes were naturally dried in air. The conversion of oxide to nitride was performed in a quartz tube furnace (Lindberg/Blue M). The

temperature was raised from room temperature to 1000 °C at the rate of 10 °C/min and held at 1000 °C for 2 hours. After that, the furnace was naturally cooled down to room temperature. During the whole process, 75 sccm anhydrous NH<sub>3</sub> flowed through the quartz tube and the pressure in the tube remained as 300 torr. The Ta<sub>3</sub>N<sub>5</sub> sample was scratched on the edge to expose the underneath conductive Ta. Tinned Cu wire was secured to the exposed Ta substrate by Ag epoxy (M.G. Chemicals Ltd.). Non-conductive hysol epoxy (Loctite 615) was used to seal the sample except for the exposed area for testing. Typical electrodes were ~0.05 cm<sup>2</sup> in area.

MgO was deposited on Ta<sub>3</sub>N<sub>5</sub> nanotube using the Cambridge nanotech (Savannah 100) ALD system based on previous reports.<sup>24, 25</sup> The Mg precursor was bis(ethylcyclopentadienyl)magnesium (Mg(CpEt)<sub>2</sub>, min. 98%, Strem Chemicals) and DI water was used as oxygen precursor. During growth, the Mg precursor was heated to 90 °C and the growth temperature was 200 °C. During each growth cycle, the pulse time for Mg(CpEt)<sub>2</sub> and H<sub>2</sub>O is 0.05s and 0.015s, respectively. The total growth cycles were varied from 5 to 25 cycles. After the growth, the MgO/Ta<sub>3</sub>N<sub>5</sub> sample was irradiated with UV light (UVO cleaner 42) for 3 hours to remove the organic residue. Then the sample was heated in the furnace at 1000 °C for 1 hour under 50 sccm anhydrous NH<sub>3</sub> flow.

The Co(OH)<sub>x</sub> was deposited using a soaking method. The Co(OH)<sub>x</sub> precursor solutions was made by mixing 0.1M cobalt(II) nitrate hexahydrate (Co(NO<sub>3</sub>)<sub>2</sub>·6H<sub>2</sub>O, ACS reagent, 98%, Sigma-Aldrich) and 0.1M NaOH solution in the volume ratio of 1:1. Then the Ta<sub>3</sub>N<sub>5</sub> and MgO/Ta<sub>3</sub>N<sub>5</sub> photoelectrodes were immersed in the precursor solution for 1hr. After that, the electrodes were rinsed with DI water and dried naturally in the air.

NiFeOOH and CoFeOOH catalyst was deposited using cathodic electrodeposition. For NiFeOOH deposition a 0.09 M solution of nickel(II) nitrate hexahydrate ( $\text{Ni}(\text{NO}_3)_2 \cdot 6\text{H}_2\text{O}$ , 98%, Alfa Aesar) was purged with  $\text{N}_2$  for 20 min. Then 0.01 M of iron(II) chloride ( $\text{FeCl}_2$ , 98%, Sigma-Aldrich) was added. The deposition was carried out galvanostatically at  $-0.1 \text{ mA/cm}^2$  for 10 min while stirring. The electrodes were then washed thoroughly with DI water. For the CoFeOOH deposition a 0.06 M of  $\text{Co}(\text{NO}_3)_2 \cdot 6\text{H}_2\text{O}$  and 0.04 M  $\text{FeCl}_2$  solution was used and the deposition rate of  $-4 \text{ mA/cm}^2$  was used for 1 minute. These procedures follow a previously reported method by the Boettcher group.<sup>26, 27</sup>

### 2.2.2 PEC measurement

PEC measurement was carried out using a potentiostat (Modulab<sup>®</sup> XM, coupled with the Modulab<sup>®</sup> XM ECS software) in a three-electrode configuration. The light source was an AM 1.5 solar simulator ( $100 \text{ mW/cm}^2$ , Solarlight Model 16S-300-M Air Mass Solar Simulator). There were three kinds of testing electrolyte, including 1M NaOH (pH 13.6), 1M NaOH with 0.1M  $\text{H}_2\text{O}_2$  (pH 13.6), 0.1M phosphate solution (mixing of 0.1M  $\text{K}_2\text{HPO}_4$  and 0.1M  $\text{K}_3\text{PO}_4$ ) with 0.1M  $\text{K}_4\text{Fe}(\text{CN})_6$  and 0.1mM  $\text{K}_3\text{Fe}(\text{CN})_6$  (pH 10). The  $\text{Ta}_3\text{N}_5$  photoanode served as the working electrode, with an Ag/AgCl electrode (for pH 10 testing electrolyte) or an Hg/HgO electrode (for pH 13.6 testing electrolyte) as the reference electrode, and a Pt wire as the counter electrode. The potential was corrected to RHE scale according to the Nernst equation:

$$E_{RHE} = E_{Ag/AgCl} + 0.059 \times pH + 0.197 \quad (2.1)$$

$$E_{RHE} = E_{Hg/HgO} + 0.059 \times pH + 0.098 \quad (2.2)$$

In a typical linear sweep voltammetry (LSV) measurement, the potential was swept from negative to positive at a rate of 20 mV/s with stirring. The turn-on potential is defined as the potential where the logarithm of absolute photocurrent reaches the lowest value in the J-V curves. In a typical open circuit potential (OCP) measurement in aqueous solution, the OCP values were recorded after a minimum of 15 min of stabilization under open-circuit conditions with vigorous stirring. The photoelectrochemical impedance spectroscopy (PEIS) was measured in 0.1M phosphate solution (mixing of 0.1M  $\text{K}_2\text{HPO}_4$  and 0.1M  $\text{K}_3\text{PO}_4$ ) with 0.1M  $\text{K}_4\text{Fe}(\text{CN})_6$  and 0.1mM  $\text{K}_3\text{Fe}(\text{CN})_6$  (pH 10) using the same three-electrode configuration and illumination intensity as mentioned above. The PEIS data were obtained by a 10 mV perturbation between 1 MHz to 1 Hz at 1.9 V.

For the PEC measurement in non-aqueous electrolyte, acetonitrile ( $\text{CH}_3\text{CN}$ , anhydrous, 99.8%, Sigma-Aldrich) used in the experiment was dried through atmospheric vacuum distillation and stored over activated 3 Å sieves. All the solution preparation and measurement was done in a  $\text{N}_2$ -filled glovebox. To prepare the solution, tetrabutylammonium hexafluorophosphate ( $\text{TBAPF}_6$ , 98%, Sigma-Aldrich) was added to the dry  $\text{CH}_3\text{CN}$  to make 0.1 M  $\text{TBAPF}_6/\text{CH}_3\text{CN}$  supporting electrolyte. The reduced form of the redox couples, including lithium sulfide ( $\text{Li}_2\text{S}$ , 99.9%, Alfa Aesar), potassium iodide ( $\text{KI}$ , 99+%, ACROS Organics), 1,1'-dimethylferrocene ( $\text{Me}_2\text{Fc}$ , 95%, Sigma-Aldrich), ferrocene ( $\text{Fc}$ , 98%, Sigma-Aldrich), (2,2,6,6-Tetramethylpiperidin-1-yl)oxyl ( $\text{TEMPO}$ , 98%, Sigma-Aldrich) and lithium bromide ( $\text{LiBr}$ , ReagentPlus, 99%, Sigma-Aldrich) with the concentration of 0.1 M was dissolved in the supporting electrolyte, respectively. The measurement was carried out using a potentiostat (CH Instrument, CHI6008C) in a three-electrode configuration similar as the aqueous solution case, but

the reference electrode was changed to  $\text{Ag}^+/\text{Ag}$  reference electrode (CH Instrument, CHI 112, filled with 10 mM  $\text{AgNO}_3$  in 0.1 M  $\text{TBAPF}_6/\text{CH}_3\text{CN}$ ). The reference electrode was calibrated using  $\text{Fc}^{+/0}$  redox couple and referred to the normal hydrogen electrode (NHE) based on the redox potential of  $\text{Fc}^{+/0}$  (0.623 V vs NHE).<sup>28</sup> For each redox couple, the redox potential was determined by cyclic voltammetry of the Pt wire electrode using the same  $\text{Ag}^+/\text{Ag}$  reference electrode. The light source was a 150 W Xenon lamp (model 71228, Newport, CA, USA) equipped with an AM 1.5G filter and the illumination intensity was calibrated to be 100  $\text{mW}/\text{cm}^2$  using a Si photodiode (UV 005, OSI, Optoelectronic, CA, USA). In a typical light OCP measurement, the OCP value was recorded after at least 15 min stabilization with continuous stirring. Then the OCP value was referred to the NHE.

### 2.2.3 Material characterization

Regular X-ray photoelectron spectroscopy (XPS) measurements were performed using a PHI 5400 XPS system equipped with an Al x-ray source (incident photon energy 1486.7 eV). The aperture size was set to 1.1 mm in diameter. The binding energy of the obtained XPS spectra was calibrated with respect to the *C1s* peak of adventitious carbon at 284.4 eV. XPS depth profiles and work function measurements using gas phase Ar were measured at the ambient-pressure XPS endstation at Beamline 9.3.2 in the Advanced Light Source, Lawrence Berkeley National Laboratory. To avoid cross-contamination from previous experiments, the XPS chamber was freshly backed before the measurements. With different incident photon energies, the binding energy of each element was calibrated with respect to *C1s* peak of the adventitious carbon, except the

case of lowest photon energy 325 eV. In this case, binding energy of Ta4f was simply aligned to the spectra collected under 560 eV photons. All the XPS spectra were quantitatively analyzed by deconvoluting Voigt-type line shapes, preceded by subtracting Shirley-type background or linear background (only for N1s/Ta4p3 regions). X-ray absorption spectroscopy (XAS) measurements were carried out at the wet-RIXS endstation at Beamline 8.0.1 and the ISAAC endstation at Beamline 6.3.1.2, both at the Advanced Light Source, Lawrence Berkeley National Laboratory. Fluorescence signal was collected using a Channeltron device, whereas total electron yield was measured as the drain current from the sample to the ground upon illumination, using a current amplifier. The energy scales of O1s and N1s XAS spectra were calibrated using a TiO<sub>2</sub> and a BN standard sample, respectively. All the XAS spectra were normalized by setting the pre-edge intensity to zero and the intensities well above the edge to unity, preceded by subtracting a linear background based on the slope of the pre-edge regions.

The scanning electron microscope (SEM, JSM6340F) was used to obtain the perspective and front view images. The fresh and tested Ta<sub>3</sub>N<sub>5</sub> samples were imaged by the transmission electron microscope (TEM, JEOL 2010F) operated at an accelerating voltage of 200 kV. The nanotube samples were first scratched from Ta foils and dispersed in isopropanol by ultrasonication. Then the dispersion was dropcasted onto Cu grid for TEM measurement. X-ray diffraction was performed on Bruker D2 PHASER with Cu K $\alpha$  radiation. Raman spectra were acquired using a Micro-Raman system (XploRA, Horiba) with a 532 nm laser excitation. The Kubelka-Munk function ( $F(R_{\infty})$ ) was calculated based on the reflectance ( $R_{\infty}$ ) of Ta<sub>3</sub>N<sub>5</sub> recorded by an integrating sphere from SphereOptics and a spectrometer (Ocean Optics USB 4000). Since  $F(R_{\infty})$  is

proportional to the light absorption coefficient, it can be substituted into the Tauc plot to determine the band gap of Ta<sub>3</sub>N<sub>5</sub>.<sup>29</sup> The band gap was determined by finding the intercept of the straight line in the low energy region of Tauc plot ( $[F(R_\infty)hv]^{1/n}$  vs.  $hv$ , when  $n=1/2$ , the measured band gap is the direct band gap).

$$F(R_\infty) = \frac{(1-R_\infty)^2}{2R_\infty} \quad (2.3)$$

$$(hvF(R_\infty))^{1/n} = A(hv - E_g) \quad (2.4)$$

The  $hv$  is the incident photon energy. The  $E_g$  is the optical band gap.  $A$  is the constant.

## 2.3 RESULTS AND DISCUSSIONS

### 2.3.1 Material characterization and PEC performance

The crystal structure of the Ta<sub>3</sub>N<sub>5</sub> NTs was confirmed by X-ray diffraction patterns (XRD, Figure 2.2a). The optical properties were characterized by ultraviolet-visible (UV-Vis) absorption spectra (Figure 2.2c), indicating the band gap of Ta<sub>3</sub>N<sub>5</sub> is 2.08 eV. The morphology and microstructures were studied using scanning electron microscopy (SEM, Figure 2.2b) and transmission electron microscopy (TEM, Figure 2.2d-e), showing the nanotube morphologies with porous structures after NH<sub>3</sub> annealing. The base performance of the resulting materials for PEC water oxidation was plotted in Figure 2.3a, where two representative samples (with and without oxygen evolution reaction catalyst) were compared. With the addition of electrodeposited NiFeOOH

catalyst, the photocurrent density of Ta<sub>3</sub>N<sub>5</sub> at 1.23 V was 6.3 mA/cm<sup>2</sup>, and the  $V_{on}$  was 0.64 V. These performance metrics are comparable to the base performance of most existing reports on Ta<sub>3</sub>N<sub>5</sub>.<sup>10, 11, 15, 16</sup>

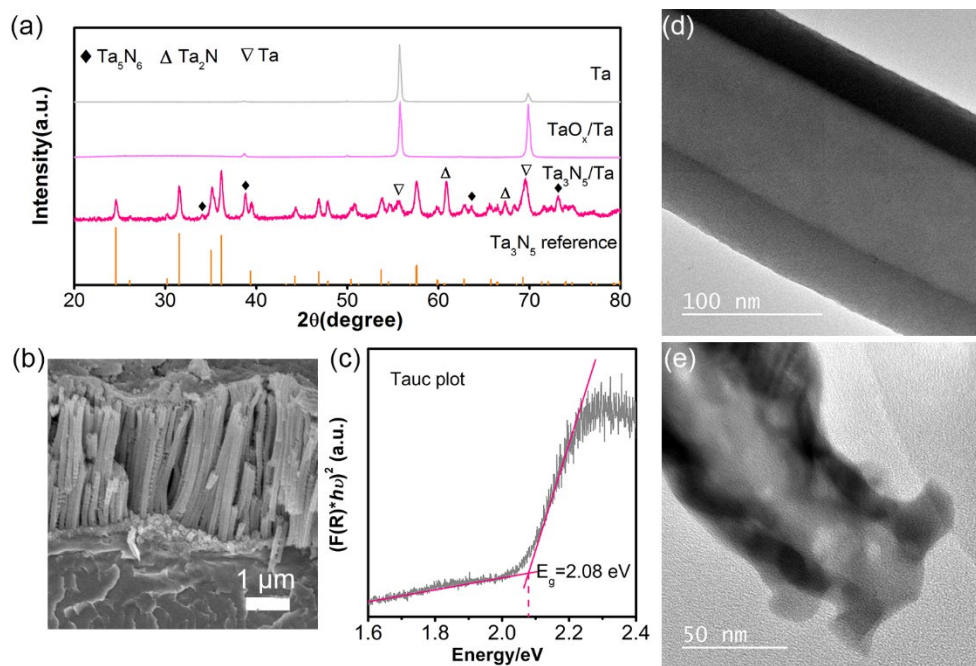


**Figure 2.2** (a) XRD patterns of Ta foil, tantalum oxide on Ta foil after anodization and Ta<sub>3</sub>N<sub>5</sub> on Ta foil after nitridation. The reference pattern of Ta<sub>3</sub>N<sub>5</sub> (PDF No. 65-1247) was also listed as comparison. (b) The side-view SEM image of Ta<sub>3</sub>N<sub>5</sub> NTs. (c) The Tauc plot of the as-prepared Ta<sub>3</sub>N<sub>5</sub> sample. TEM images of (d) TaO<sub>x</sub> nanotubes after the anodization and (e) Ta<sub>3</sub>N<sub>5</sub> nanotubes after nitridation.

For bare Ta<sub>3</sub>N<sub>5</sub>, its PEC performance in 1 M NaOH is unstable, showing photocurrent decay from 3 mA/cm<sup>2</sup> to 0.5 mA/cm<sup>2</sup> within 1 min. A photocurrent of < 0.03 mA/cm<sup>2</sup> was measured after 3 hr. The stability issue is also consistent with other reports on bare Ta<sub>3</sub>N<sub>5</sub>.<sup>11</sup> Similar performance degradation has been frequently observed on non-oxide photoactive materials such as GaP, GaAs and CdSe (or CdS), where photocorrosion was identified as the reason.<sup>7, 8, 30</sup> High-resolution TEM was carried out to compare Ta<sub>3</sub>N<sub>5</sub> with different history of water oxidation (as prepared, 1 cycle of CV, and 3 hr photoelectrolysis of H<sub>2</sub>O). As shown in Figure 2.3b-d, while an amorphous layer

appeared after the initial CV scan, it only grew from ca. 0.5 nm to ca. 1 nm after 3 hr of photoelectrolysis. When the photoelectrolysis time was extended to 6 hr and 13 hr, the thickness of surface amorphous layer remained unchanged (ca. 3 nm), supporting that surface oxidation is self-limiting. The change of other properties including morphologies and crystal structures of  $Ta_3N_5$  remained undistinguishable before and after performance degradation, supporting that the change of the bulk properties is not a reason for the performance decay. Next the changes of surface electronic properties were examined to understand the performance decay.

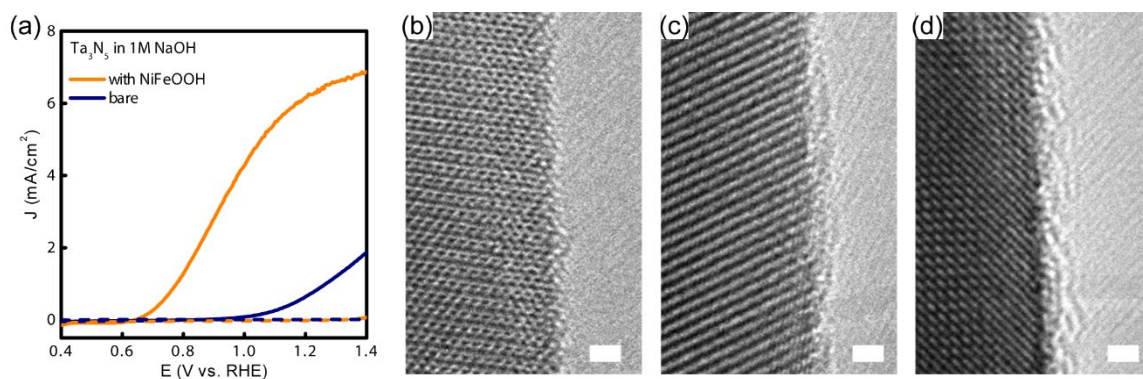


**Figure 2.3** Base Performance and TEM Characterization of  $Ta_3N_5$  (a) The current-voltage relationship of  $Ta_3N_5$  in 1 M NaOH (pH 13.6). Illumination condition = 100 mW/cm<sup>2</sup>, AM 1.5; scan rate = 20 mV/s. (b-d) TEM image of the  $Ta_3N_5$  surface as prepared (b), after one cycle of CV scan (c), and after 3 hr of photoelectrolysis at 1.23 V (d). Scale bars represent 1 nm.

### 2.3.2 X-ray core-level spectroscopy studies

X-ray absorption spectroscopy (XAS) and X-ray photoelectron spectroscopy (XPS) were carried out to further study the surfaces. The total electron yield (TEY) of O 1s and N 1s X-ray absorption spectra were shown in Figure 2.4a&b, respectively. As shown in Figure 2.4a, there is indeed an increase of O intensity on the surface as  $Ta_3N_5$  performs PEC

water oxidation. The trend supports that the amorphous layer as shown in Figure 2.3c&d contains oxygen. The evolution of a shoulder peak at 401 eV for N 1s TEY spectra (Figure 2.4b) may be assigned to the feature corresponding to trapped molecular N<sub>2</sub>, a product from the surface oxidation of N<sup>3-</sup> (Ref. <sup>31</sup>).

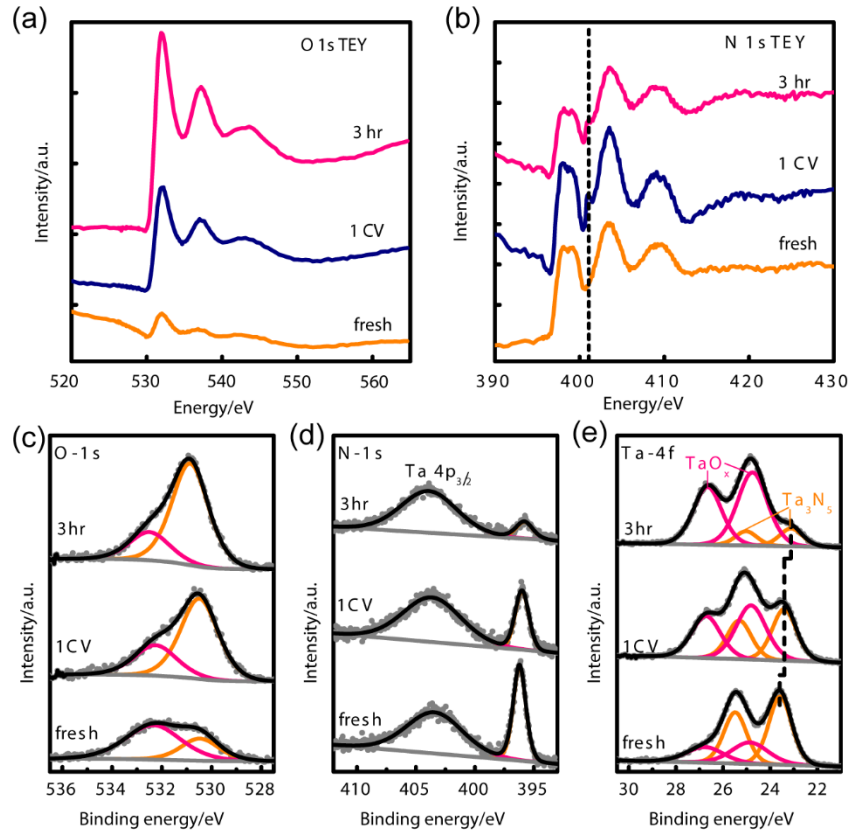


**Figure 2.4** X-ray spectra of Ta<sub>3</sub>N<sub>5</sub> (a and b) Total electron yield of O 1s and N 1s X-ray absorption spectra. The dotted vertical line in (b) serves as a visual guide. (c–e) Binding energies of O 1s (c), N 1s (d), and Ta 4f (e) electrons as measured by XPS. Samples compared in this figure include as-prepared Ta<sub>3</sub>N<sub>5</sub> (fresh), Ta<sub>3</sub>N<sub>5</sub> after one cycle of CV (1 CV), and Ta<sub>3</sub>N<sub>5</sub> after 3 hr of photoelectrolysis (3 hr). The dotted vertical line in (e) serves as a visual guide.

In Figure 2.4c-d, the XPS spectra of O 1s, N 1s and Ta 4f electrons for samples of different history were compared. In Figure 2.4c, the O 1s peak at 532.5 eV corresponds to the O-contamination species (e.g., surface chemisorbed H<sub>2</sub>O/hydroxyl group, NaOH residue), while the one at 530.5 eV belongs to TaO<sub>x</sub> species. A clear trend of O signal

intensity increase, N signal intensity decrease and the growth of  $\text{TaO}_x$  upon water oxidation is obvious from this set of data, which is consistent with the conclusion that surface N is displaced by O as a function of photoelectrolysis. Close examinations of the Ta 4f spectra revealed a shift of the binding energies, from 23.6 eV to 23.1 eV. Because XPS measures the energy difference between the Fermi level ( $E_F$ ) and the core electrons, the shift as shown in Figure 2.4e strongly suggests a shift of the  $\text{Ta}_3\text{N}_5$  Fermi level toward the positive direction by 0.5 eV. The shift will be further studied in section 2.3.3 by ambient pressure XPS (APXPS), which is more surface sensitive. It is important to note here that in the XPS depth-profile (using different incident photon energies, Figure 2.5), a sharp increase of oxide component in the Ta 4f XPS spectra with the decreasing incident photon energies (thus shallower probing depth) was observed. Comparison of this set of data for samples after 1 cycle of CV and 3 hr photoelectrolysis strongly supported the self-limiting feature of the surface oxidation. This feature distinguishes  $\text{Ta}_3\text{N}_5$  from other non-oxide photoanode materials such as GaP, GaAs and CdSe.

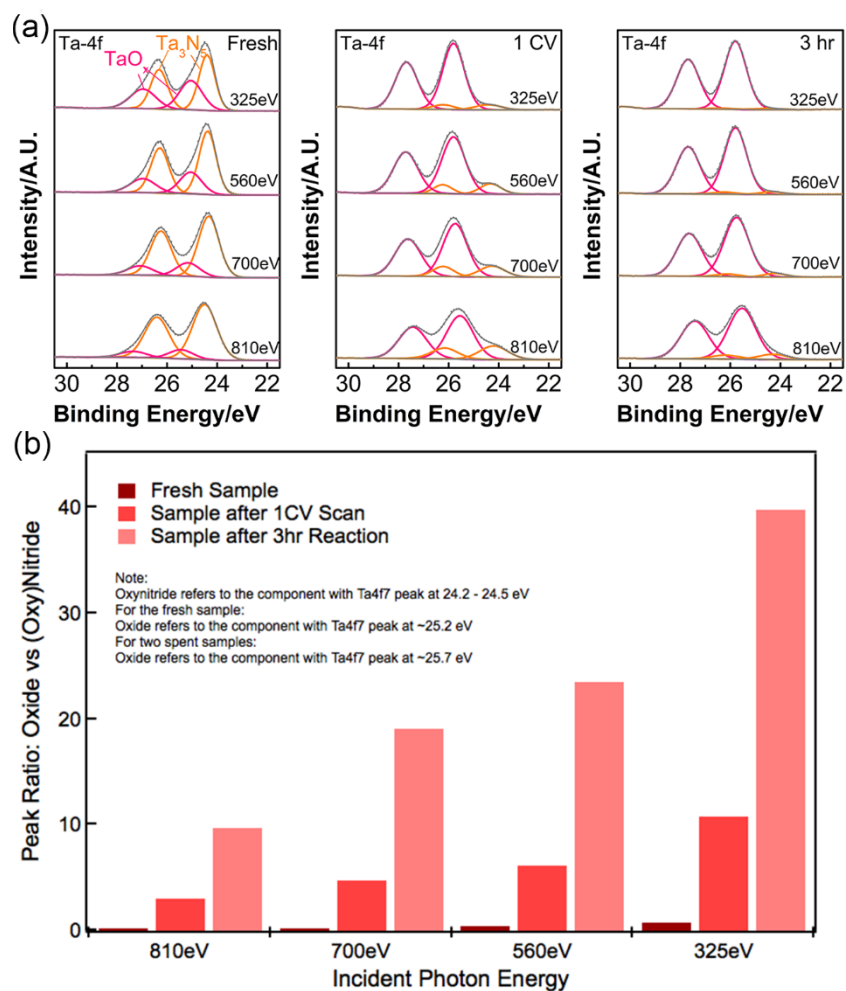


**Figure 2.5** (a) The XPS depth profile of fresh Ta<sub>3</sub>N<sub>5</sub>, Ta<sub>3</sub>N<sub>5</sub> after one light CV and 3 hours photoelectrolysis at 1.23 V<sub>RHE</sub> in 1M NaOH. The photo energy varied from 325 eV to 810 eV. (b) The peak intensity ratio of oxide vs. nitride based on the XPS spectrum in (a).

### 2.3.3 Energetics evolution due to surface reaction

Previous results have pointed out the surface oxide formation for Ta<sub>3</sub>N<sub>5</sub> during PEC water oxidation process. In this section, how this process affected the surface energetics (e.g., Fermi level) was studied, which led to the explanation for the limited photovoltage of Ta<sub>3</sub>N<sub>5</sub> during water oxidation.

### 2.3.3.1 PEC characterization with hole scavengers

A conclusion we can draw from the aforementioned experiments is that O is a critical species connected to the performance degradation of Ta<sub>3</sub>N<sub>5</sub> because its appearance appears to be associated with the performance degradation. To test this understanding, PEC characterization was conducted with hole scavengers, which are expected to be effective in extracting holes from the photoelectrode under PEC conditions, but do not involve O as a necessary intermediate or product. For this purpose, Fe(CN)<sub>6</sub><sup>4-</sup> was used, which possesses the redox potential of 1.02 V in the pH 10 buffer solution. Within the first 60 s of chronoamperometry, a negligible decay of the photocurrent was observed when Fe(CN)<sub>6</sub><sup>4-</sup> was present (Figure 2.6a). In stark contrast, the photocurrent decreased >50% within the first 5 s in 1 M NaOH. TEM studies of the Ta<sub>3</sub>N<sub>5</sub> surfaces with and without Fe(CN)<sub>6</sub><sup>4-</sup> also revealed a striking difference: Little change was observed when Fe(CN)<sub>6</sub><sup>4-</sup> was present. When H<sub>2</sub>O<sub>2</sub> was used as a hole scavenger, although effective in receiving holes, the oxidation of H<sub>2</sub>O<sub>2</sub> does involve O species. An intermediate stability, better than without hole scavengers but worse than with Fe(CN)<sub>6</sub><sup>4-</sup>, was observed.

Taken as a whole, it is concluded that the performance degradation of Ta<sub>3</sub>N<sub>5</sub> is connected to surface oxidation. The displacement of N by O yields surface states that pin the Fermi level, which compromises the charge separation capability (i.e., the decreased band bending). Although the surface oxidation process is self-limiting, the electronic states it creates are sufficient to suppress the photoactivity of Ta<sub>3</sub>N<sub>5</sub>. Further comparison of the PEC characteristics of Ta<sub>3</sub>N<sub>5</sub> in H<sub>2</sub>O, with Fe(CN)<sub>6</sub><sup>4-</sup> and with H<sub>2</sub>O<sub>2</sub>, respectively, shows that in addition to better stability, better  $V_{on}$ 's (0.35 V) were also measured in the presence of hole scavengers (Figure 2.6b). The data suggest that both the performance

degradation and the late  $V_{on}$  are connected to surface oxidation. While the impact of surface Fermi level pinning on the PEC performance of photoelectrode has been frequently discussed in the literature,<sup>32-36</sup> here the clear link between surface oxidation and surface Fermi level pinning was explicitly demonstrated. It points to a direction where complete blocking of O-containing species from contacting  $Ta_3N_5$  is necessary to maintain the performance of  $Ta_3N_5$ .

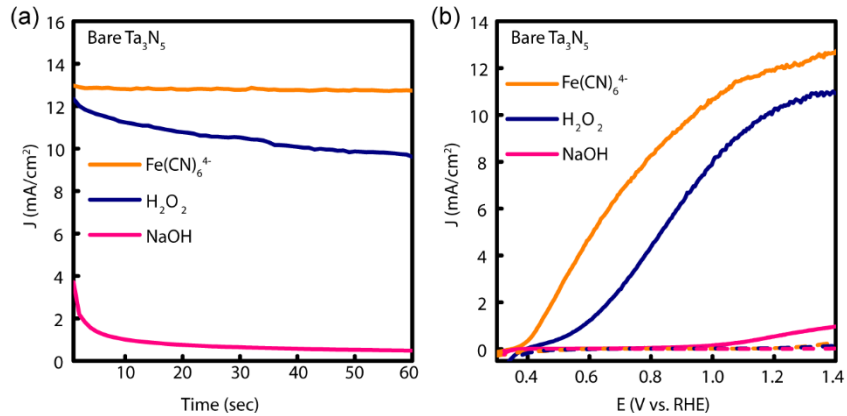


**Figure 2.6** PEC performance in the presence of hole scavengers. (a) The stability of bare  $Ta_3N_5$  was much better when  $H_2O_2$  (0.1 M; 1 M NaOH [pH 13]) was added and the best when  $K_4Fe(CN)_6$  (0.1 M; potassium phosphate buffer [pH 10] with 0.1 mM  $K_3Fe(CN)_6$ ) was present. Applied potential ( $V_{app}$ ) = 1.23 V. (B) The initial current-voltage relationship of  $Ta_3N_5$  in the solutions as identified above. Scan rate = 20 mV/s.

### 2.3.3.2 Flatband potential shift due to $H_2O$

In this section, the answer to an important question was explored. That is, what is the origin of the significant difference between the predicted flat-band potential ( $V_{fb}$ ) and the measured  $V_{on}$  in  $H_2O$ ? DFT calculations showed that the  $E_{CB}$  and  $V_{fb}$  should be more negative than 0 V vs. NHE.<sup>17, 18</sup> The prediction was consistent with the measurements carried out by Domen et al. using UPS (ultraviolet photoelectron spectroscopy) and Mott-Schottky techniques.<sup>37</sup> However, the reported  $V_{on}$ 's are typically much more positive

than the predicted/measured  $V_{fb}$ , by  $>0.6$  V.<sup>10-12, 14-16</sup> To help understand the difference, open-circuit potential (OCP) measurements were carried out under illumination in both aqueous and non-aqueous solutions. The assumption is that illumination would flatten the band, and the probed OCPs report on the pseudo- $V_{fb}$ . Under similar lighting conditions, the comparison of these pseudo- $V_{fb}$  provides a reasonable measure of how the true  $V_{fb}$  changes for different samples.<sup>38</sup> As shown in Figure 2.7, the OCPs of Ta<sub>3</sub>N<sub>5</sub> in H<sub>2</sub>O (ca. 0.44 V vs. RHE) and that in acetonitrile (ca. -0.23 V vs. NHE) are different by ca. 0.67 V. The difference ( $>0.6$  V) was attributed as the band edge shift due to the chemisorption of H<sub>2</sub>O on the surface of Ta<sub>3</sub>N<sub>5</sub>. It explains why the  $V_{on}$  as measured in H<sub>2</sub>O is always so positive. Furthermore, the result suggests that in order to actualize the full potentials of Ta<sub>3</sub>N<sub>5</sub> (both high photocurrent and high photovoltage), it would require fully isolating its surface from H<sub>2</sub>O to avoid the polarization effect of H<sub>2</sub>O that induces severe positive shift of the band edge positions.

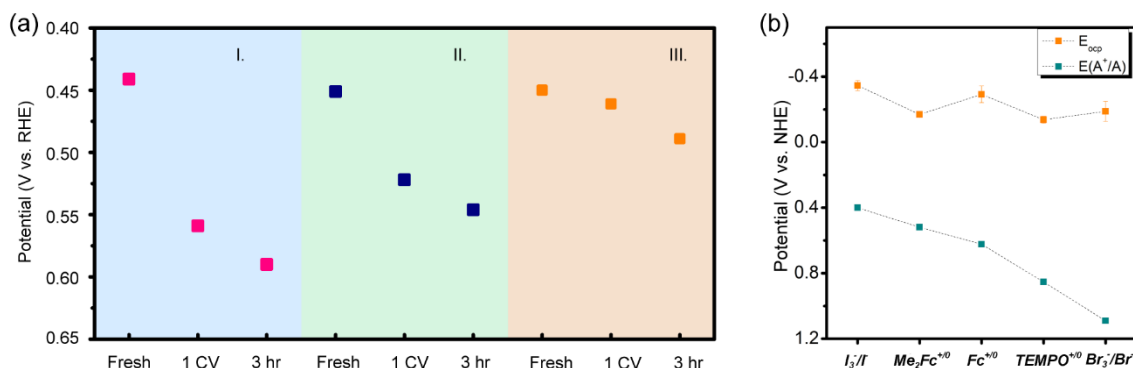


**Figure 2.7** (a) Light OCPs of three groups of Ta<sub>3</sub>N<sub>5</sub> electrodes as measured in phosphate buffer with 0.1 M K<sub>4</sub>Fe(CN)<sub>6</sub> and 0.1 mM K<sub>3</sub>Fe(CN)<sub>6</sub>. The samples in (I) were tested in 1 M NaOH for one cycle of CV and 3 hr of photoelectrolysis. Similarly, the samples in (II) were tested in 1 M NaOH with 0.1 M H<sub>2</sub>O<sub>2</sub>. The samples in (III) were tested in phosphate buffer (pH 10) with 0.1 M K<sub>4</sub>Fe(CN)<sub>6</sub> and 0.1 mM K<sub>3</sub>Fe(CN)<sub>6</sub>.  $V_{app}$  for all tests = 1.23 V. (b) The light OCPs (orange square) of Ta<sub>3</sub>N<sub>5</sub> in the solution of 0.1 M TBAPF<sub>6</sub>/CH<sub>3</sub>CN with 0.1M different redox couples. The redox potential of each redox pair is labelled as green square. The average value of light OCP is -0.23 V vs. NHE.

### 2.3.3.3 Surface Fermi level pinning due to oxidation

The aforementioned  $>0.6$  V shift is global (both the band edge positions and the Fermi level) upon contact with  $\text{H}_2\text{O}$ . As  $\text{Ta}_3\text{N}_5$  is subjected to  $\text{H}_2\text{O}$  oxidation, the surface is chemically oxidized, and N is displaced by O. This process is expected to introduce additional states within the bandgap and lead to the shift of the Fermi level relative to the band edge positions, a phenomenon known as Fermi level pinning.<sup>32-36</sup> Such a shift has already been shown by XPS studies of  $\text{Ta}_3\text{N}_5$  in Figure 2.4e. To further study this shift, the work functions of  $\text{Ta}_3\text{N}_5$  electrode with different history of PEC water oxidation was measured using ambient pressure XPS (APXPS). The basic idea was to use the shift in the apparent binding energy of gas molecules near the sample surface as a probe to measure the work function.<sup>39</sup> In the experiments, the measurements were carried out in a chamber where 100 mTorr of Ar was present. By probing the changes of the apparent binding energies of Ar, a direct measure on how the surface Fermi level changes for different samples was obtained. As shown in Figure 2.8, three different samples were compared, fresh  $\text{Ta}_3\text{N}_5$ ,  $\text{Ta}_3\text{N}_5$  after 1 cycle of CV, and  $\text{Ta}_3\text{N}_5$  after 3 hr photoelectrolysis. The binding energies of Ar  $2p$  electrons shifted a total of ca.  $-0.4$  eV, corresponding to a shift of the  $\text{Ta}_3\text{N}_5$   $E_F$  by  $+0.4$  eV. The shift is comparable to that observed in Figure 2.4e. It can be understood as the continued photoelectrolysis by  $\text{Ta}_3\text{N}_5$  and, hence, surface oxidation of  $\text{Ta}_3\text{N}_5$ , leads to the Fermi level shift toward the  $E_{\text{VB}}$  by  $0.4$ - $0.5$  V. In addition, since the measurement of XPS/APXPS tells about the interface in vacuum or Ar where no condense phase of water exists, it confirms the Fermi level pinning happens on the  $\text{Ta}_3\text{N}_5/\text{TaO}_x\text{N}_y$  interface.

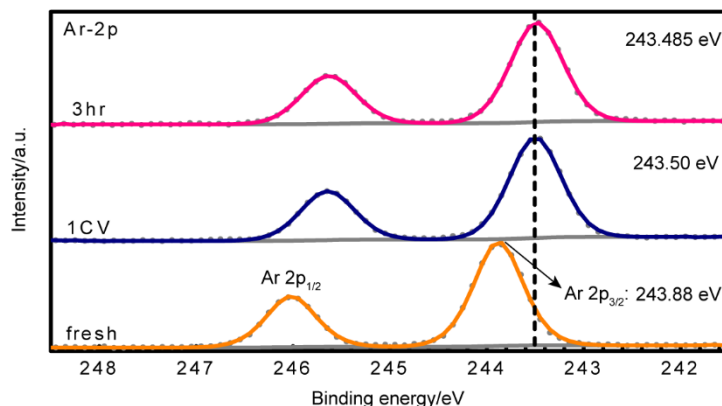


**Figure 2.8** Ar 2p XPS spectra of 100 mTorr Ar gas phase at the near surface region of Ta<sub>3</sub>N<sub>5</sub>. The testing samples included fresh Ta<sub>3</sub>N<sub>5</sub>, Ta<sub>3</sub>N<sub>5</sub> after one cycle of CV under illumination, and Ta<sub>3</sub>N<sub>5</sub> after 3 hr of photoelectrolysis at 1.23 V. The test electrolyte was 1 M NaOH, and the light intensity was 100 mW/cm<sup>2</sup> (AM 1.5). The dotted vertical line serves as a visual guide.

However, there is an important feature in this group of data as compared to that in Figure 3E that is worth discussing. That is, the shift as measured by XPS (Figure 2.4e) was gradual (0.2 eV for fresh sample to after 1 cycle of CV; and 0.3 eV after 3 hr photoelectrolysis), while that measured by APXPS was almost complete after 1 cycle of CV (0.4 eV). The difference may be explained by the characteristic probing depth of XPS and APXPS under different incident photon energies.<sup>31</sup> For Figure 2.4e, photoelectrons with kinetic energies around 1450 eV (Ta 4f electrons) were measured, featuring a typical escape depth of 2-2.5 nm. For Figure 2.8, photoelectrons corresponding to Ar 2p orbitals were measured, reporting on the surface energies of Ta<sub>3</sub>N<sub>5</sub> <1nm deep. As such, the information as shown in Figure 2.8 is far more surface sensitive than that in Figure 2.4e. This group of data strongly suggests that the Fermi level pinning due to surface oxidation starts on the very top surface of Ta<sub>3</sub>N<sub>5</sub>. After 1 cycle of CV, the effect is already fully measured by APXPS. As the photoelectrolysis continues, the oxidation continues into the underlayers of the surface atoms, whose effect

becomes obvious over time as measured by XPS. The understanding is supported by the compositional depth profile as shown in Figure 2.5.

### 2.3.3.4 The evolution of tantalum nitride surface energetics

The combination of OCP, XPS and APXPS measurements offered a complete picture of how the surface energetics evolve as a function of surface adsorption and/or oxidation. As shown in Figure 2.9, three key conclusions can be drawn to understand the evolution of the surface energetics.

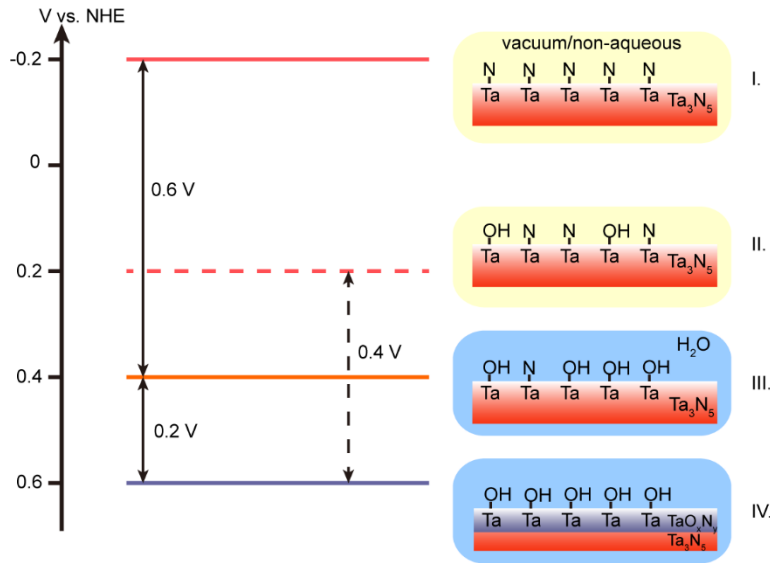


**Figure 2.9** The evolution of Ta<sub>3</sub>N<sub>5</sub> surface energetics. Stage I: fresh Ta<sub>3</sub>N<sub>5</sub> free of H<sub>2</sub>O. Stage II: Ta<sub>3</sub>N<sub>5</sub> with partial H<sub>2</sub>O adsorption due to exposure to ambient air. Stage III: Ta<sub>3</sub>N<sub>5</sub> immersed in H<sub>2</sub>O. Stage IV: Ta<sub>3</sub>N<sub>5</sub> with surface oxides. The horizontal lines correspond to the surface Fermi-level position of Ta<sub>3</sub>N<sub>5</sub> in stages I–IV.

(1) Truly fresh Ta<sub>3</sub>N<sub>5</sub> (without H<sub>2</sub>O adsorption on the surface; stage I in Figure 2.9) features a  $V_{fb}$  close to -0.2 V vs. NHE. This is supported by the OCP measurements carried out in non-aqueous solutions. It is also consistent with the UPS measurements reported by Domen et al.<sup>37</sup> Once such a surface is exposed to liquid H<sub>2</sub>O, due to the strong surface adsorption and the solvent effect, a dramatic shift of the band edge

positions toward the positive direction by 0.6 V takes place (stage III in Figure 2.9). The shift is measured by the difference between the OCP in non-aqueous and aqueous solutions (Figure 2.7). Similar band edge shift due to the solvation effect is well known for non-oxide semiconductors when characterized in H<sub>2</sub>O.<sup>40</sup> It is noted that such a global shift of the band edge positions (as well as the Fermi level) is detrimental to the application of H<sub>2</sub>O photo-oxidation as it reduces the measureable photovoltage. It may be necessary to fully isolate Ta<sub>3</sub>N<sub>5</sub> from H<sub>2</sub>O in order to fully realize the energy conversion capability of Ta<sub>3</sub>N<sub>5</sub>.

(2) When Ta<sub>3</sub>N<sub>5</sub> oxidizes H<sub>2</sub>O under illumination, its surface N atoms are displaced by O atoms, and this change leads to a relative change of the Fermi level to the band edge positions by 0.2 V toward the positive direction (stage IV in Figure 2.9). The shift of the Fermi level is probed by the OCP measurements in H<sub>2</sub>O (Figure 2.7a). The final position of the Fermi level defines the relatively high  $V_{on}$  as measured on bare Ta<sub>3</sub>N<sub>5</sub> in most reports, ca. >0.6 V. Collectively, ca. 0.8 V shift of the Fermi level can be observed from fresh, H<sub>2</sub>O-free Ta<sub>3</sub>N<sub>5</sub> surface (stage I in Figure 2.9) to the oxidized, H<sub>2</sub>O-adsorbed Ta<sub>3</sub>N<sub>5</sub> surface (stage IV in Figure 2.9). The understanding is consistent with a recent study on the surface of GaN due to reactions with H<sub>2</sub>O.<sup>41</sup>

(3) The Fermi level shift as measured by XPS (and APXPS) reflects the difference between the final stage (IV in Figure 2.9) and an intermediate stage (II in Figure 2.9) where there is partial surface H<sub>2</sub>O adsorption due to exposure to ambient air. From the comparison between the shift as measured by APXPS (Figure 2.8) and that by XPS (Figure 2.4e), the initial shift (after 1 cycle of CV) may be non-permanent and is reversible, which is tested in the next section.

### 2.3.4 Recovery of the initial performance degradation by water oxidation catalysts

Previous sections have shown that Ta<sub>3</sub>N<sub>5</sub> surface can be oxidized in the presence of photogenerated holes. Not only does the process compete with H<sub>2</sub>O oxidation, it also leads to severe surface Fermi level pinning that compromises the charge separation capabilities of Ta<sub>3</sub>N<sub>5</sub>. As shown in Figure 2.10, the gray trace from a to c indicated a rapid performance degradation. After 25 cycles of continued CV, little photocurrent was observed in Figure 2.10c (gray trace). Additional PEIS measurement showed that the charge transfer resistance across Ta<sub>3</sub>N<sub>5</sub> and electrolyte interface increased from around 500 Ω to over 20000 Ω after just 1 CV scan in 1 M NaOH, indicating that the surface oxidation introduced an extra charge transfer barrier on Ta<sub>3</sub>N<sub>5</sub> surface. It has been shown that the addition of water oxidation catalyst, such as NiFeOOH, can promote forward hole transfer.<sup>42</sup> Such an addition (the catalyst) is expected to reduce the competing reaction of surface oxidation of the photoelectrode itself as well as facilitate the hole transfer from Ta<sub>3</sub>N<sub>5</sub> to water. Indeed, immediately after the 1<sup>st</sup> CV, the addition of NiFeOOH led to a significant increase of the photocurrent (from 1.2 mA/cm<sup>2</sup> to 3.2 mA/cm<sup>2</sup> at 1.23 V). The effect also supports that the initial surface Fermi level pinning as measured by APXPS (Figure 2.8) does not fully suppress the performance of Ta<sub>3</sub>N<sub>5</sub>. As the photoelectrode was subjected to prolonged H<sub>2</sub>O oxidation reactions without the presence of a water oxidation catalyst, however, the effect due to surface Fermi level pinning as a result of Ta<sub>3</sub>N<sub>5</sub> oxidation becomes more permanent, as evidenced by the continued reduction of the photocurrent even with the presence of NiFeOOH (Figure 2.10b&c). This group of experiments highlights the nature of Ta<sub>3</sub>N<sub>5</sub> surface oxidation and that its negative impact on the PEC performance is gradual, consistent with our

discussions in the previous section. To provide a baseline for comparison, the performance of fresh bare  $\text{Ta}_3\text{N}_5$ , with  $\text{NiFeOOH}$ , and with  $\text{CoFeOOH}$  (another water oxidation catalyst) is shown in Figure 2.10d.

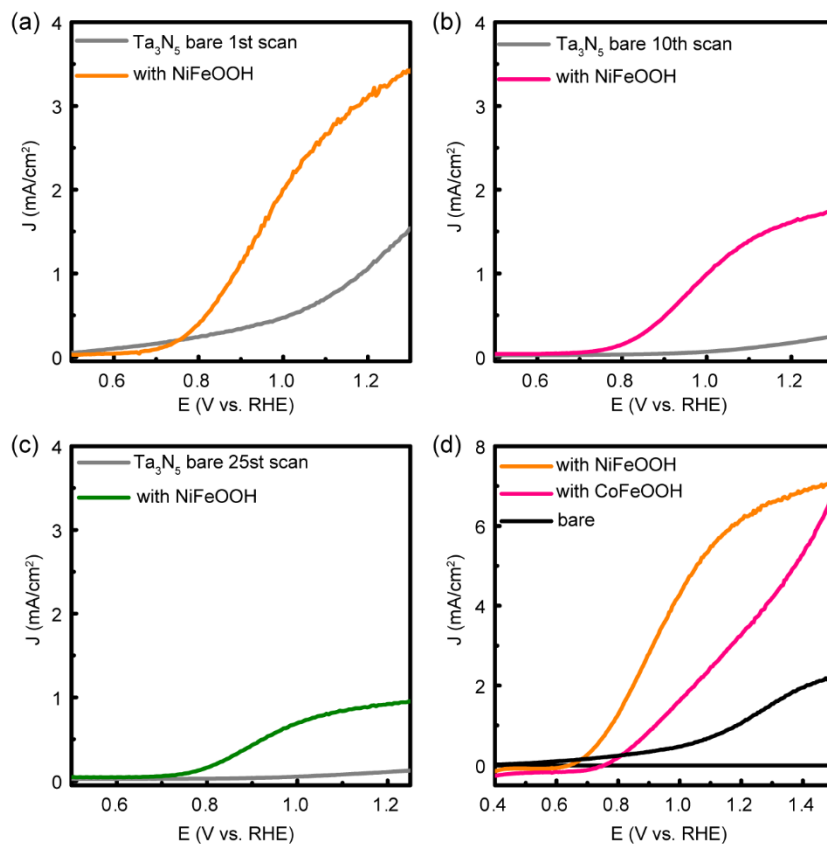


**Figure 2.10** Recovery of the initial performance degradation by water-oxidation catalysts. (a–c) The current-voltage relationships for bare  $\text{Ta}_3\text{N}_5$  with different cycles of water oxidation tests (a, 1st scan; b, 10th scan; c, 25th scan) and the performance with re-deposited  $\text{NiFeOOH}$ . (d) The J-V curve of freshly prepared  $\text{Ta}_3\text{N}_5$  with  $\text{NiFeOOH}$  or  $\text{CoFeOOH}$  as the catalyst.

### 2.3.5 Strategies for improving tantalum nitride

It is seen from previous discussions that the isolation of  $\text{Ta}_3\text{N}_5$  from  $\text{H}_2\text{O}$  (and other reactive oxygen species) is critical to stabilizing its performance. For instance, while the deposition of water oxidation catalyst such as  $\text{NiFeOOH}$ ,  $\text{CoFeOOH}$ , and  $\text{Co(OH)}_x$  all

resulted in higher photocurrents, their effect in improving the stability was limited. Moreover, they showed little effect in improving the  $V_{on}$ . This is likely due to the inclusion of water during the deposition of these catalysts as well as the H<sub>2</sub>O permeable nature of these catalysts.<sup>43-45</sup> Therefore, the possibility of introducing a compact interlayer of MgO by atomic layer deposition (ALD) was explored. The idea was to use the MgO layer as a barrier to separate Ta<sub>3</sub>N<sub>5</sub> from contacting H<sub>2</sub>O and reactive O species. MgO was chosen because it was previously shown as an effective interlayer to improve the attachment of catalysts on Ta<sub>3</sub>N<sub>5</sub> particles.<sup>46</sup> As shown in Figure 2.11a, the ALD growth of MgO on Ta<sub>3</sub>N<sub>5</sub> was successful. Even after soaked in NaOH solution for 1 hour, such a protection layer still remained on the surface of Ta<sub>3</sub>N<sub>5</sub> based on the high-resolution TEM image (Figure 2.11b). Since MgO itself is not a water oxidation catalyst, we deposited Co(OH)<sub>x</sub> on top. Here Co(OH)<sub>x</sub> was chosen because its deposition conditions are compatible with MgO, whereas the deposition of NiFeOOH and other catalysts would etch MgO due to the low pH required. The effect of MgO in protecting Ta<sub>3</sub>N<sub>5</sub> was clearly observed in Figure 2.11. In addition to better stability, the addition of MgO also improved the fill factor, suggesting better charge collection, presumably due to reduction of surface recombination. It is noted that great progress along the direction of stabilizing Ta<sub>3</sub>N<sub>5</sub> has been made by the Li and the Domen groups separately.<sup>10-12, 19</sup> However, the true nature of the performance degradation has not been asked previously in detail (for instance, the difference between photocorrosion and self-limited oxidation was not compared). In their cases, the deposition of a thick layer was necessary. Li et al. ascribed the necessity to the need to store holes, which would minimize the oxidation of Ta<sub>3</sub>N<sub>5</sub> itself.<sup>11, 12</sup> The results reported here provide new insight into this critical issue.

They support that the isolation of Ta<sub>3</sub>N<sub>5</sub> from H<sub>2</sub>O is critical to its stabilization. While there is still much room for further improvement with the ALD-grown MgO idea (e.g., the  $V_{on}$  still remains high), the initial results are promising, given the thinness of the layer (<3 nm). Further research along this direction will likely significantly improve its performance in the future.

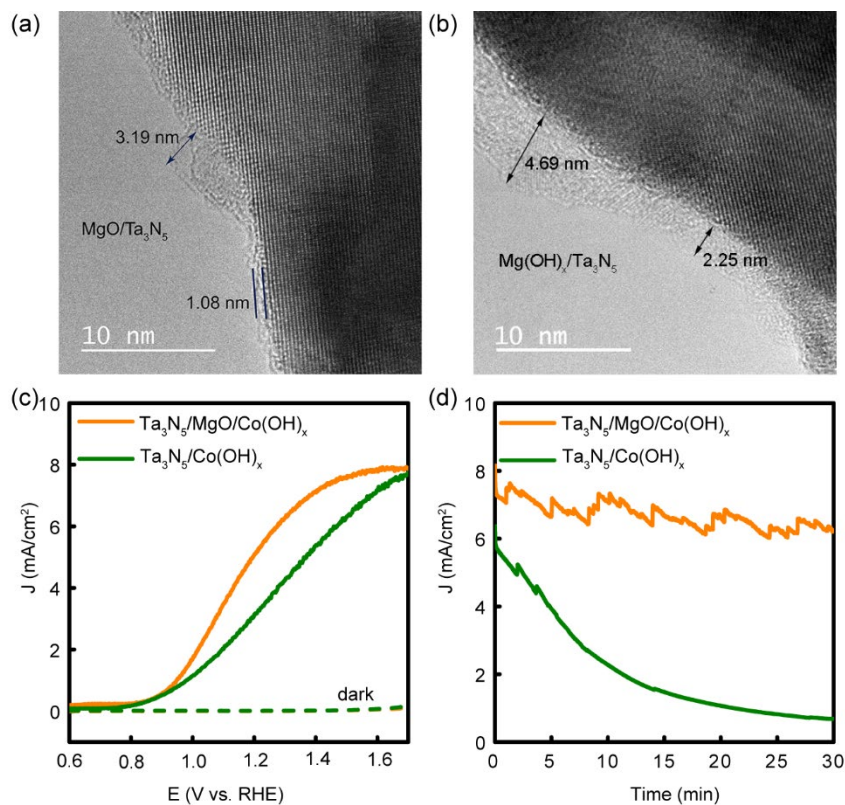


**Figure 2.11** (a) The TEM image of Ta<sub>3</sub>N<sub>5</sub> with 15 cycles of MgO growth by ALD. (b) The TEM image of Ta<sub>3</sub>N<sub>5</sub> with 25 cycles of MgO which has been soaked in 0.1 M NaOH for 1 hour. The J-V curves (c) and the stability of Ta<sub>3</sub>N<sub>5</sub> (d) with and without MgO as a protection layer and Co(OH)<sub>x</sub> as the catalyst in 1 M NaOH. For the stability test, the potential was fixed at 1.23 V.

## 2.4 SUMMARY

In conclusion, the issues that limit the performance of Ta<sub>3</sub>N<sub>5</sub> as a solar water oxidation electrode are the surface oxidation. Although this process is self-limiting, and the oxide remains ca. 3 nm in thickness, the electronic states it generates are more than enough to fully pin the Fermi level, which leads to almost complete suppression of the photoactivity. Using X-ray core-level spectroscopy characterization, the effect was quantitatively measured. Together with photoelectrochemical and open circuit potential measurements, a complete picture on how the surface energetics evolved as a function of surface oxidation and adsorption of H<sub>2</sub>O was obtained. Upon contact with liquid H<sub>2</sub>O, a global shift of both the band edge and the Fermi level by more than 0.6 V was observed. Further oxidation of the surface will result in another shift of the Fermi level relative to the band edge positions by 0.2 V. Mere exposure to ambient air can cause the Fermi level shift by up to 0.5 V. Together, the information sheds light on future strategies to improve the performance of Ta<sub>3</sub>N<sub>5</sub>. It is suggested that complete isolation of Ta<sub>3</sub>N<sub>5</sub> from not only H<sub>2</sub>O but also other reactive O species is necessary.

## 2.5 REFERENCE

1. M. G. Walter, E. L. Warren, J. R. McKone, S. W. Boettcher, Q. Mi, E. A. Santori and N. S. Lewis, *Chem. Rev.*, 2010, **110**, 6446-6473.
2. J. R. McKone, N. S. Lewis and H. B. Gray, *Chem. Mater.*, 2013, **26**, 407-414.
3. Y. Lin, S. Zhou, X. Liu, S. Sheehan and D. Wang, *J. Am. Chem. Soc.*, 2009, **131**, 2772-2773.
4. K. Sivula, F. Le Formal and M. Grätzel, *ChemSusChem*, 2011, **4**, 432-449.
5. F. M. Pesci, A. J. Cowan, B. D. Alexander, J. R. Durrant and D. R. Klug, *J. Phys. Chem. Lett.*, 2011, **2**, 1900-1903.

6. F. F. Abdi and R. van de Krol, *J. Phys. Chem. C*, 2012, **116**, 9398-9404.
7. K. W. Frese, M. J. Madou and S. R. Morrison, *J. Phys. Chem.*, 1980, **84**, 3172-3178.
8. S. Yamane, N. Kato, S. Kojima, A. Imanishi, S. Ogawa, N. Yoshida, S. Nonomura and Y. Nakato, *J. Phys. Chem. C*, 2009, **113**, 14575-14581.
9. S. Hu, M. R. Shaner, J. A. Beardslee, M. Lichterman, B. S. Brunshwig and N. S. Lewis, *Science*, 2014, **344**, 1005-1009.
10. Y. Li, L. Zhang, A. Torres-Pardo, J. M. González-Calbet, Y. Ma, P. Oleynikov, O. Terasaki, S. Asahina, M. Shima, D. Cha, L. Zhao, K. Takanebe, J. Kubota and K. Domen, *Nat. Commun.*, 2013, **4**, 2566.
11. G. Liu, J. Shi, F. Zhang, Z. Chen, J. Han, C. Ding, S. Chen, Z. Wang, H. Han and C. Li, *Angew. Chem. Int. Ed.*, 2014, **53**, 7295-7299.
12. G. Liu, S. Ye, P. Yan, F.-Q. Xiong, P. Fu, Z. Wang, Z. Chen, J. Shi and C. Li, *Energy Environ. Sci.*, 2016, **9**, 1327-1334.
13. H. Hajibabaei, O. Zandi and T. W. Hamann, *Chem. Sci.*, 2016, **7**, 6760-6767.
14. Y. Li, T. Takata, D. Cha, K. Takanebe, T. Minegishi, J. Kubota and K. Domen, *Adv. Mater.*, 2013, **25**, 125-131.
15. L. Wang, X. Zhou, N. T. Nguyen, I. Hwang and P. Schmuki, *Adv. Mater.*, 2016, **28**, 2432-2438.
16. M. Li, W. Luo, D. Cao, X. Zhao, Z. Li, T. Yu and Z. Zou, *Angew. Chem. Int. Ed.*, 2013, **52**, 11016-11020.
17. J. Wang, A. Ma, Z. Li, J. Jiang, J. Feng and Z. Zou, *RSC Adv.*, 2014, **4**, 55615-55621.
18. J. Wang, T. Fang, L. Zhang, J. Feng, Z. Li and Z. Zou, *J. Catal.*, 2014, **309**, 291-299.
19. J. Seo, T. Takata, M. Nakabayashi, T. Hisatomi, N. Shibata, T. Minegishi and K. Domen, *J. Am. Chem. Soc.*, 2015, **137**, 12780-12783.
20. L. Wang, F. Dionigi, N. T. Nguyen, R. Kirchgeorg, M. Gliech, S. Grigorescu, P. Strasser and P. Schmuki, *Chem. Mater.*, 2015, **27**, 2360-2366.
21. M. Higashi, K. Domen and R. Abe, *Energy Environ. Sci.*, 2011, **4**, 4138-4147.
22. K. Maeda and K. Domen, *MRS Bull.*, 2011, **36**, 25-31.
23. L. Wang, N. T. Nguyen, X. Zhou, I. Hwang, M. S. Killian and P. Schmuki, *ChemSusChem*, 2015, **8**, 2615-2620.
24. B. B. Burton, D. N. Goldstein and S. M. George, *J. Phys. Chem. C*, 2009, **113**, 1939-1946.
25. Y. Lin, Y. Xu, M. T. Mayer, Z. I. Simpson, G. McMahon, S. Zhou and D. Wang, *J. Am. Chem. Soc.*, 2012, **134**, 5508-5511.
26. L. Trotochaud, S. L. Young, J. K. Ranney and S. W. Boettcher, *J. Am. Chem. Soc.*, 2014, **136**, 6744-6753.
27. M. S. Burke, M. G. Kast, L. Trotochaud, A. M. Smith and S. W. Boettcher, *J. Am. Chem. Soc.*, 2015, **137**, 3638-3648.
28. V. V. Pavlishchuk and A. W. Addison, *Inorganica Chimica Acta*, 2000, **298**, 97-102.
29. E. Nurlaela, S. Ould-Chikh, M. Harb, S. del Gobbo, M. Aouine, E. Puzenat, P. Sautet, K. Domen, J.-M. Basset and K. Takanebe, *Chem. Mater.*, 2014, **26**, 4812-4825.

30. J. R. Wilson and S. M. Park, *J. Electrochem. Soc.*, 1982, **129**, 149-154.
31. H. C. Choi, S. Y. Bae, J. Park, K. Seo, C. Kim, B. Kim, H. J. Song and H.-J. Shin, *Appl. Phys. Lett.*, 2004, **85**, 5742-5744.
32. A. J. Bard, A. B. Bocarsly, F. R. F. Fan, E. G. Walton and M. S. Wrighton, *J. Am. Chem. Soc.*, 1980, **102**, 3671-3677.
33. C. Du, M. Zhang, J.-W. Jang, Y. Liu, G.-Y. Liu and D. Wang, *J. Phys. Chem. C*, 2014, **118**, 17054-17059.
34. C. Du, X. Yang, M. T. Mayer, H. Hoyt, J. Xie, G. McMahon, G. Bischooping and D. Wang, *Angew. Chem. Int. Ed.*, 2013, **52**, 12692-12695.
35. J.-W. Jang, C. Du, Y. Ye, Y. Lin, X. Yao, J. Thorne, E. Liu, G. McMahon, J. Zhu, A. Javey, J. Guo and D. Wang, *Nat. Commun.*, 2015, **6**, 7447.
36. J. E. Thorne, S. Li, C. Du, G. Qin and D. Wang, *J. Phys. Chem. Lett.*, 2015, **6**, 4083-4088.
37. W.-J. Chun, A. Ishikawa, H. Fujisawa, T. Takata, J. N. Kondo, M. Hara, M. Kawai, Y. Matsumoto and K. Domen, *J. Phys. Chem. B*, 2003, **107**, 1798-1803.
38. Z. Chen, T. F. Jaramillo, T. G. Deutsch, A. Kleiman-Shwarsstein, A. J. Forman, N. Gaillard, R. Garland, K. Takanabe, C. Heske, M. Sunkara, E. W. McFarland, K. Domen, E. L. Miller, J. A. Turner and H. N. Dinh, *J. Mater. Res.*, 2010, **25**, 3-16.
39. S. Axnanda, M. Scheele, E. Crumlin, B. Mao, R. Chang, S. Rani, M. Faiz, S. Wang, A. P. Alivisatos and Z. Liu, *Nano Lett.*, 2013, **13**, 6176-6182.
40. Y. V. Pleskov, *Solar energy conversion: a photoelectrochemical approach*, Springer-Verlag Berlin Heidelberg, 1991.
41. X. Zhang and S. Ptasinska, *Sci. Rep.*, 2016, **6**, 24848.
42. C. G. Morales-Guio, M. T. Mayer, A. Yella, S. D. Tilley, M. Grätzel and X. Hu, *J. Am. Chem. Soc.*, 2015, **137**, 9927-9936.
43. F. Lin and S. W. Boettcher, *Nat. Mater.*, 2014, **13**, 81-86.
44. M. S. Burke, L. J. Enman, A. S. Batchellor, S. Zou and S. W. Boettcher, *Chem. Mater.*, 2015, **27**, 7549-7558.
45. M. R. Nellist, F. A. L. Laskowski, F. Lin, T. J. Mills and S. W. Boettcher, *Acc. Chem. Res.*, 2016, **49**, 733-740.
46. S. Chen, S. Shen, G. Liu, Y. Qi, F. Zhang and C. Li, *Angew. Chem. Int. Ed.*, 2015, **54**, 3047-3051.

Chapter 2 is adapted with permission from “Y. He, J. E. Thorne, C. H. Wu, P. Ma, C. Du, Q. Dong, J. Guo and D. Wang, *Chem*, 2016, **1**, 640-655.” Copyright 2016 Elsevier.

## **CHAPTER 3 PHOTO-INDUCED PERFORMANCE ENHANCEMENT OF TANTALUM NITRIDE FOR SOLAR WATER OXIDATION**

### **3.1 TANTALUM NITRIDE AS A PLATFORM FOR INTERFACIAL STUDY BETWEEN SEMICONDUCTORS AND CATALYSTS**

Photocatalysis by semiconducting materials represents an important class of chemical reactions.<sup>1,2</sup> Key to the functionality and performance of a photocatalyst is the interface between the semiconductor and the electrolyte.<sup>3-5</sup> On the one hand, the interface is critical to the separation of photogenerated charges within the semiconductor. On the other hand, the interface plays a vital role in transferring the separated charges for desired chemical reactions in the liquid electrolyte. Challenges that limit the overall performance of a photocatalyst such as poor charge separation or low stability are often connected to issues at the interface. For instance, previous studies on  $\text{Fe}_2\text{O}_3$ <sup>6-10</sup> have revealed that surface states at the semiconductor/liquid interface (SCLI) are a critical reason for the low photovoltages, the understanding of which has led to significantly improved performance of  $\text{Fe}_2\text{O}_3$  for solar water oxidation.<sup>11, 12</sup> Similarly, detailed analysis on  $\text{Ta}_3\text{N}_5$  has uncovered that rapid surface states formation due to displacement of N atoms by O is the real reason for the fast performance degradation (see Chapter 2). These previous successes highlight the importance of studying the SCLI in details. However, most prior

studies fail to account for the dynamic nature of the interface, particularly for systems where co-catalysts are present.<sup>4, 13</sup> Given that the application of co-catalyst has been increasingly recognized as critical for complex reactions such as water oxidation<sup>14</sup> and CO<sub>2</sub> reduction<sup>15</sup>, it is important to correct such a deficiency. In this chapter, the study focused on the interactions between the co-catalyst (Co(OH)<sub>2</sub>) and the photoactive semiconductor (Ta<sub>3</sub>N<sub>5</sub>). It is found that only under illumination conditions does a favorable interface form, leading to a continuous improvement of the performance of Ta<sub>3</sub>N<sub>5</sub>. The effect is in stark contrast to bare Ta<sub>3</sub>N<sub>5</sub>, which would degrade rapidly under similar conditions.

Ta<sub>3</sub>N<sub>5</sub> is chosen as the prototypical material platform for the present study for two important reasons. First, the physical properties of Ta<sub>3</sub>N<sub>5</sub> render it an appealing material choice for solar water splitting applications, as described in Chapter 2. Second, poor stability is a critical issue that limits the prospect of Ta<sub>3</sub>N<sub>5</sub> as a practical photoelectrode material for solar water splitting. The large gap between the promises and the measured performance makes it significant to stabilize Ta<sub>3</sub>N<sub>5</sub> under PEC water oxidation conditions.<sup>16-19</sup> While encouraging results have been recently obtained in this front by the introduction of, for instance, hole storage layers<sup>20, 21</sup> or GaN<sup>22</sup>, these efforts do not involve chemical reactions between Ta<sub>3</sub>N<sub>5</sub> and the co-catalyst and/or the passivation layer. The approach in this study therefore represents a new direction toward stabilizing Ta<sub>3</sub>N<sub>5</sub>. The efforts are also inspired by recent observations that the performance of BiVO<sub>4</sub> can be improved by a photocharging effect.<sup>23, 24</sup> Nevertheless, the study on BiVO<sub>4</sub> photocharging primarily focused on how the semiconductor changes in response

to light. This study takes an important step forward by examining the interactions between the semiconductor and the co-catalyst.

## 3.2 MATERIALS AND METHODS

### 3.2.1 Material synthesis

The synthesis of Ta<sub>3</sub>N<sub>5</sub> NTs can be found in section 2.2.1. To deposit Co(OH)<sub>2</sub> nanosheets on Ta<sub>3</sub>N<sub>5</sub>, the Co(OH)(OCH<sub>3</sub>) powders was first synthesized based on a modified method.<sup>25</sup> 0.2910 g of cobalt nitrate hexahydrate (Co(NO<sub>3</sub>)<sub>2</sub>·6H<sub>2</sub>O, ACS reagent, 98%, Sigma-Aldrich) was dissolved in 15 mL of methanol (99.8% ACS reagent, Sigma-Aldrich). The solution was sealed in a Teflon autoclave and placed in 180 °C oven for 24 hours. The obtained precipitate was washed by ethanol and H<sub>2</sub>O and collected after centrifuging for 10 min at 3000 rpm. Pink powders were obtained after drying the precipitate in 80 °C oven for 10 hours. Then certain amount (2-4 mg based on PEC performance) of Co(OH)(OCH<sub>3</sub>) powder was added to 10 mL of DI water and ultrasonicated for 30 min. The supernatant was added to Teflon autoclave with Ta<sub>3</sub>N<sub>5</sub> NTs faced up, which has been etched in a mixture of HF:HNO<sub>3</sub>:H<sub>2</sub>O (1:2:7 in v/v) for 30 s. The container was placed in 120 °C oven for 1 hour. After that, the sample was washed mildly by DI water and dried in air.

As the control experiment, α-Co(OH)<sub>2</sub> was synthesized based on a reported method<sup>26</sup>. 0.2922 g of potassium chloride (KCl, 99%, Alpha Aesar), 0.2379 g of cobalt chloride hexahydrate (CoCl<sub>2</sub>·6H<sub>2</sub>O, ACS reagent, 98%, Sigma-Aldrich) and 1.68 g of

hexamethylenetetramine (ACS reagent, 99%, Sigma-Aldrich) were dissolved in 100 mL 9:1 mixture of DI water and ethanol. The solution was heated at 90 °C under stirring for 1 hour. The product was washed by ethanol and H<sub>2</sub>O and collected by centrifuging at 3000 rpm for 10 min. Green powder was obtained after drying the product in 80 °C oven for 2 hours. The Co(OH)<sub>2</sub> was deposited on the Ta<sub>3</sub>N<sub>5</sub> following the same procedure as the Co(OH)<sub>2</sub> nanosheet case.

Co-Pi and NiFeO<sub>x</sub> were deposited on the prepared Ta<sub>3</sub>N<sub>5</sub> NTs photoelectrodes (photoelectrode fabrication procedures see section 2.2.1). For Co-Pi, it was deposited onto Ta<sub>3</sub>N<sub>5</sub> using photo-assisted electrodeposition reported previously.<sup>17</sup> Before the deposition, the Ta<sub>3</sub>N<sub>5</sub> photoelectrode was etched in a mixture of HF:HNO<sub>3</sub>:H<sub>2</sub>O (1:2:7 in v/v) for 30 s and rinsed by DI water. The deposition was conducted in a three-electrode cell containing Ta<sub>3</sub>N<sub>5</sub> as the working electrode, Pt gauze as the counter electrode and Ag/AgCl reference electrode. The electrolyte contained 0.5 mM Co(NO<sub>3</sub>)<sub>2</sub> in 0.1 M potassium phosphate buffer with pH 7. The deposition was conducted at 10 μA/cm<sup>2</sup> constant current under 100 mW/cm<sup>2</sup> illumination for 10 min with stirring. After the deposition, the photoelectrode was rinsed by DI water. Ta<sub>3</sub>N<sub>5</sub>/Co(OH)<sub>2</sub>/Co-Pi was synthesized following the same procedures (no etching step) with different deposition time, but with Ta<sub>3</sub>N<sub>5</sub>/Co(OH)<sub>2</sub> nanosheets as the starting material. For NiFeO<sub>x</sub>, it was deposited on Ta<sub>3</sub>N<sub>5</sub> through a photochemical decomposition method.<sup>27</sup> Iron (III) 2-ethylhexanoate (50% w/w in mineral spirits, Strem Chemicals) and nickel (II) 2-ethylhexanoate (78% w/w in 2-ethylhexanoic acid, Strem Chemicals) were mixed in hexane solvent to achieve a total concentration of 15% w/w metal complex solution. The solution was diluted by hexane by 10 times and about 10 μL/cm<sup>2</sup> of the diluted solution

was dropcasted onto the exposed surface of Ta<sub>3</sub>N<sub>5</sub> photoelectrode. Then the electrode was irradiated with UV light (UVO cleaner 42) for 5 min and placed in 100 °C oven for 10 min. Ta<sub>3</sub>N<sub>5</sub>/Co(OH)<sub>2</sub>/NiFeO<sub>x</sub> was synthesized following the same method, but with Ta<sub>3</sub>N<sub>5</sub>/Co(OH)<sub>2</sub> nanosheets as the starting material.

Hematite and TiO<sub>2</sub> photoanodes were synthesized as the control samples. The hematite was synthesized using a chemical bath deposition.<sup>11</sup> FeOOH was grown on fluorine-doped tin oxide (FTO) substrates (~7 Ω/sq, Sigma-Aldrich) in a solution containing 0.15 M iron chloride (FeCl<sub>3</sub>, 97% Alfa Aesar) and 1 M sodium nitrate (NaNO<sub>3</sub>, 99% Alfa Aesar). After reacting in 100 °C oven for 1 hour, the sample was taken out and rinsed by DI water. Then it was annealed in 800 °C furnace for 5min in air. The whole process was repeated for another two times. The TiO<sub>2</sub> was deposited on FTO substrates using a Cambridge nanotech (Savannah 100) atomic layer deposition (ALD) system.<sup>28</sup> Titanium (IV) isopropoxide (99.999% trace metal basis, Sigma-Aldrich) was heated to 75 °C to serve as Ti precursors and DI H<sub>2</sub>O at room temperature served as O precursor. The growth temperature was 275 °C. The thickness of TiO<sub>2</sub> was about 40 nm. The deposition procedures for Co(OH)<sub>2</sub> nanosheets on hematite and TiO<sub>2</sub> followed the same one mentioned above.

### 3.2.2 EC measurement

PEC measurement was carried out with a potentiostat (Modulab XM coupled with Modulab XM ECS software) in a three-electrode configuration. The light source was an AM 1.5 solar simulator (100 mW/cm<sup>2</sup>, Solarlight Model 16S-300-M Air Mass Solar Simulator). For water oxidation, the electrolyte was 1 M NaOH (pH 13.6) and the

reference electrode was Hg/HgO. For hole scavenger oxidation, the electrolyte was 0.1 M potassium phosphate with 0.1 M  $\text{K}_4\text{Fe}(\text{CN})_6$  (pH 10) and the reference electrode was Ag/AgCl. Particularly, the hole scavenger solution used in Figure 3.12 was 1 M NaOH with 0.1 M  $\text{K}_4\text{Fe}(\text{CN})_6$  and the reference electrode was Hg/HgO. In typical cyclic voltammetry test, the potential was swept between 0.4 V and 1.4 V at a scan rate of 20 mV/s. In a typical light OCP measurement, the OCP value was recorded after a minimum of 20 min stabilization under open-circuit condition with vigorous stirring.

IMPS spectra were recorded with a potentiostat (Modulab XM coupled with a frequency response analyzer, a 405 nm LED and Modulab XM DSSC software) in the same three-electrode cell as the PEC test condition. The IMPS data were obtained at different applied potential between 0.43 V and 1.63 V, and at each potential 10 % light intensity modulation was varied between 10 kHz and 0.1 Hz. The light intensity at the electrode was about 134 mW/cm<sup>2</sup>.

PEIS spectra were measured with a potentiostat (Modulab XM coupled with Modulab XM ECS software) in the same three-electrode cell as the PEC test condition. The data were recorded at 1 V with 10 mV perturbation between 100 kHz and 0.05 Hz. The data was fitted to the equivalent circuit as shown in Figure 3.10 using the Z-view software.

### **3.2.3 Material characterization**

The sample were imaged by a field-emission scanning electron microscopy (FE-SEM, JEOL 6340F) at 10 kV and a transmission electron microscopy (TEM, JEOL 2010F) at 200 kV. The surface species and oxidation states were measured by X-ray photoelectron

spectroscopy (K-alpha<sup>+</sup> XPS, Thermo Scientific, Al K $\alpha$ =1486.7 eV). The X-ray diffraction was performed on a Rigaku D/max-III A diffractometer.

The O<sub>2</sub> evolved during the PEC water oxidation was detected *in-situ* by a Clark-type BOD oxygen electrode (Thermo Scientific 9708 DOP). The Ta<sub>3</sub>N<sub>5</sub>/Co(OH)<sub>2</sub> working electrode, Hg/HgO reference electrode, Pt counter electrode and oxygen sensor were tightly sealed in a three-neck flask with 130 mL 1 M NaOH by plastic rubbers and Para film. Vacuum grease was used to prevent leaking. Before the PEC test, Ar was purged into the electrolyte for at least 30 min to remove the dissolved O<sub>2</sub> as well as the O<sub>2</sub> in the headspace. After the needle to purge Ar was removed, the reading of oxygen sensor was stabilized for 10 min. Once the PEC test started, the O<sub>2</sub> concentration was recorded on a pH meter connected with the oxygen sensor.

### 3.3 RESULTS AND DISCUSSIONS

#### 3.3.1 Material characterization and PEC performance

As shown in Figure 3.1a, Co(OH)<sub>2</sub> was deposited on Ta<sub>3</sub>N<sub>5</sub> NT using a hydrothermal method. The crystal structure of Co(OH)<sub>2</sub> was confirmed by XRD, and its nanosheet morphology was confirmed using SEM (Figure 3.1b-e). In addition, the morphology remained the same even after PEC water oxidation test (Figure 3.1f-g).

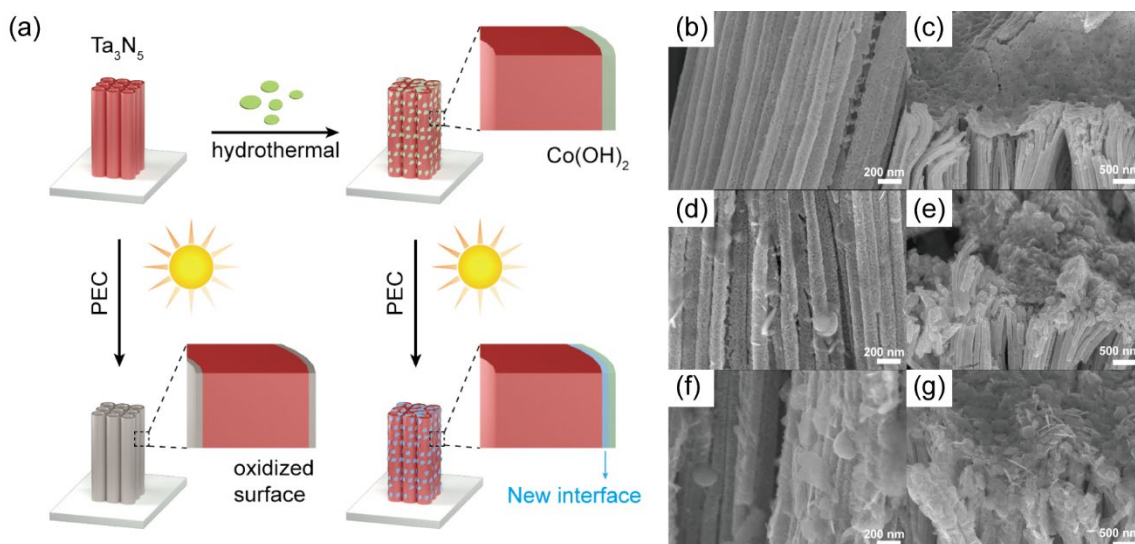


**Figure 3.1** (a) Schematics illustrating the surface oxidation of bare  $\text{Ta}_3\text{N}_5$  and the formation of new interfaces between  $\text{Ta}_3\text{N}_5$  and  $\text{Co}(\text{OH})_2$  during solar water oxidation. The SEM images for side walls (b, d, f) and top (c, e, g) of  $\text{Ta}_3\text{N}_5$  before (b, c) and after (d, e) the deposition of  $\text{Co}(\text{OH})_2$  as well as  $\text{Ta}_3\text{N}_5/\text{Co}(\text{OH})_2$  after the PEC test (f, g, at 1.23 V for 1hr in 1M NaOH, light intensity: 100 mW/cm<sup>2</sup>).

The characteristic photocurrent density-voltage relationship (J-V) for  $\text{Ta}_3\text{N}_5$  with  $\text{Co}(\text{OH})_2$  was plotted in Figure 3.2a. It is highly surprising that repeated PEC scans led to obvious increase of the photocurrent, which is opposite to how bare  $\text{Ta}_3\text{N}_5$  photoelectrodes behave (Figure 2.6). For easy comparison of the effect, the  $J_{\text{ph}}$  at 1.23 V (vs. RHE) and  $V_{\text{on}}$  were plotted as a function of PEC scans in Figure 3.2b. It is seen that at the 14<sup>th</sup> cycle, the photocurrent (3.1 mA/cm<sup>2</sup>) was 3 times of the first scan (1.0 mA/cm<sup>2</sup>). In addition,  $V_{\text{on}}$  shifted negatively by 110 mV after 20 CV scans. The effect was also obvious from the chronoamperometry data as shown in Figure 3.2c, where the photocurrent densities of two samples, bare  $\text{Ta}_3\text{N}_5$  and  $\text{Ta}_3\text{N}_5$  with  $\text{Co}(\text{OH})_2$  nanosheets (denoted as  $\text{Ta}_3\text{N}_5/\text{Co}(\text{OH})_2$ ), were recorded as a function of time. While the initial photocurrent densities for the two samples were comparable (ca. 0.8 mA/cm<sup>2</sup>), it increased to 3.2 mA/cm<sup>2</sup> for the sample with  $\text{Co}(\text{OH})_2$  co-catalyst and decreased to 0.1

mA/cm<sup>2</sup> for bare Ta<sub>3</sub>N<sub>5</sub> within 30 min. Stability up to 5 h can be achieved for Ta<sub>3</sub>N<sub>5</sub>/Co(OH)<sub>2</sub>, which was much better than bare Ta<sub>3</sub>N<sub>5</sub> (Figure 3.2d). More interestingly, dark electrochemical (EC) water oxidation performance did not improve under similar electrolysis conditions. The dark current density appeared to be higher compared with that under light condition because of the high applied potentials (2 V vs. RHE for the measurements of dark currents; 1.23 V vs. RHE was applied for the light current measurements). At this potential, the diode formed at the Ta<sub>3</sub>N<sub>5</sub>/electrolyte interface is effectively operating in the breakdown regime, acting as a conductive substrate to support Co(OH)<sub>2</sub> as OER catalysts. To exclude the possibility that the observed increase of photocurrent was due to parasitic reactions (e.g., the oxidation of Co<sup>2+</sup>) instead of water oxidation, O<sub>2</sub> as a product during photoelectrolysis was detected, and a faradic efficiency close to 100% was measured (Figure 3.2e).

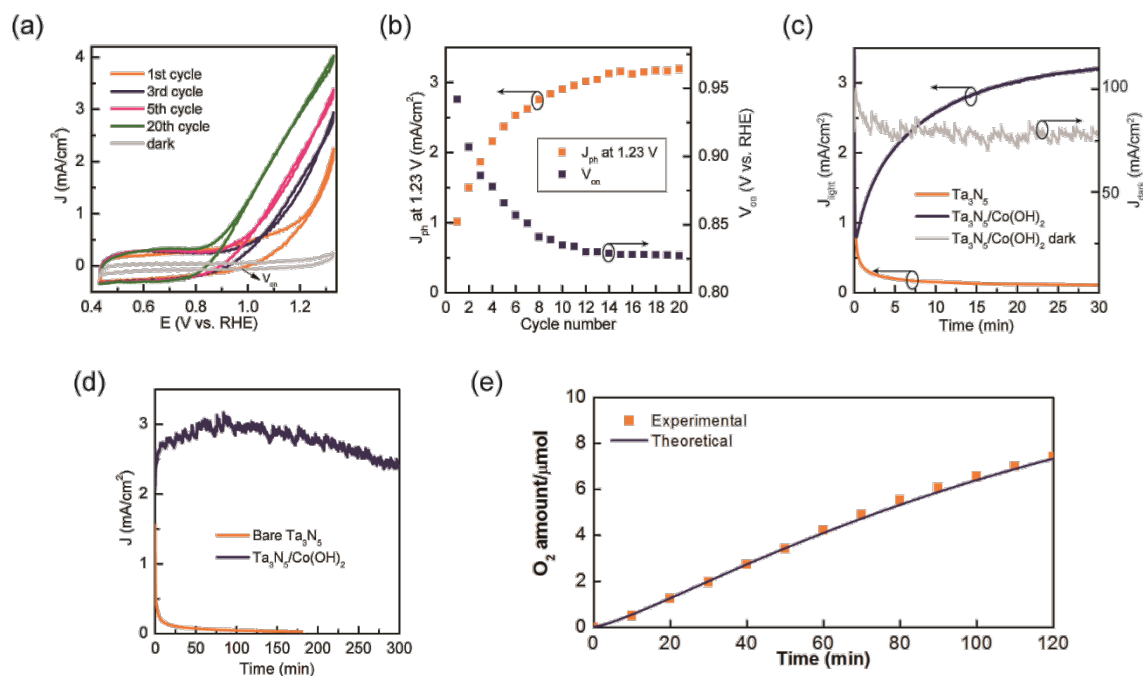


**Figure 3.2** (a) J-V curves of Ta<sub>3</sub>N<sub>5</sub>/Co(OH)<sub>2</sub> at different cycle numbers. (b) Photocurrent densities at 1.23 V from 20 cycles of consecutive CV scans of Ta<sub>3</sub>N<sub>5</sub>/Co(OH)<sub>2</sub>. (c) Photocurrent density-time data of Ta<sub>3</sub>N<sub>5</sub>/Co(OH)<sub>2</sub> and bare

Ta<sub>3</sub>N<sub>5</sub> at 1.23 V. Dark current density-time data of Ta<sub>3</sub>N<sub>5</sub>/Co(OH)<sub>2</sub> at 2 V. (d) The photovoltage-time curve for Ta<sub>3</sub>N<sub>5</sub> with and without Co(OH)<sub>2</sub> at 1.23 V. The Ta<sub>3</sub>N<sub>5</sub>/Co(OH)<sub>2</sub> sample has been tested for 20 CV scans under light before the photoelectrolysis. (e) The O<sub>2</sub> amount experimentally detected (square dot) and calculated based on the charges assuming 100% faradaic efficiency (solid line). Nearly 100% faradaic efficiency was obtained within the two hours' photoelectrolysis at 1.23 V. The electrolyte (1 M NaOH) and the lighting conditions (AM 1.5 illumination at 100 mW/cm<sup>2</sup>) were the same for the data shown from (a) to (d). All voltages are relative to RHE.

### 3.3.2 Explore possible hypotheses for the performance enhancement

To understand the reasons for the performance enhancement, both the semiconductor and the co-catalyst were inspected next.

#### 3.3.2.1 Catalyst activation

The improvement of water oxidation catalysts under photo-oxidation conditions has been reported by Li et al., which was attributed to the charging effect of Ni(OH)<sub>2</sub>.<sup>21</sup> Similarly, EC activation of catalysts has been observed for Co(OH)<sub>2</sub> and Ni(OH)<sub>2</sub> by Boettcher et al.<sup>29,30</sup> To understand whether the phenomenon as shown in Figure 3.2 can be explained by catalyst activation, the J-V curves of Ta<sub>3</sub>N<sub>5</sub>/Co(OH)<sub>2</sub> under two different conditions were measured and compared: (1) after photoelectrolysis at 1.23 V for 10 min; (2) continuous electrolysis at 2 V for 10 min. As shown in Figure 3.3a, the photocurrent at 1.23 V increased 16% in the absence of light. By stark contrast, it increased a factor 2 under PEC conditions. Further increasing the applied potential and time for the EC treatment showed little enhancement for both photocurrent densities and turn-on potentials (Figure 3.3b and c). In addition, the possibility that the EC treatment will damage the photoelectrode was excluded, as shown in Figure 3.3d. The results suggest

that electrochemical activation of  $\text{Co(OH)}_2$  is modest (16% only) and cannot account for the observed enhancement. Moreover,  $\text{Co(OH)}_2$  was confirmed to be oxidized to  $\text{CoOOH}$  under both EC and PEC conditions, further supporting that changes of the catalyst were not the key reason for the performance enhancement.

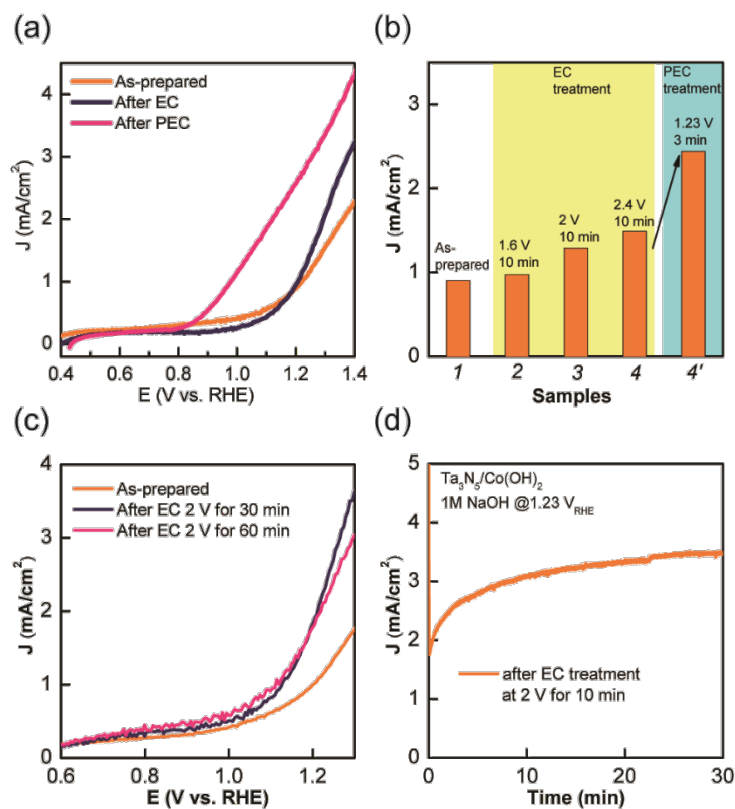


**Figure 3.3** (a) J-V data of  $\text{Ta}_3\text{N}_5/\text{Co(OH)}_2$  as-prepared and after EC and PEC treatment in 1 M NaOH. EC treatment, dark electrolysis at 2 V for 10 min; PEC treatment, photo-electrolysis at 1.23 V for 10 min. The arrows highlight the improvement of photocurrent densities and turn-on potentials after PEC treatments. (b) The photocurrent in 1M NaOH for  $\text{Ta}_3\text{N}_5/\text{Co(OH)}_2$  at 1.23 V for sample 1 (as-prepared), sample 2 (after electrochemical water oxidation at 1.6 V for 10 min), sample 3 (after electrochemical water oxidation at 2 V for 10 min) and sample 4 (after electrochemical water oxidation at 2.4 V for 10 min). The sample 4' is sample 4 after another 3 min's photoelectrolysis at 1.23 V. The light illumination condition is the same for all 4 samples. (c) The J-V curve of  $\text{Ta}_3\text{N}_5$  after 30 min and 60 min electrochemical water oxidation at 2 V. The  $V_{\text{on}}$  and photocurrent is still worse than the sample after PEC test in Figure 3.2a. (d) The photocurrent-time curve for  $\text{Ta}_3\text{N}_5/\text{Co(OH)}_2$  after EC treatment at 2 V for 10 min. The electrolyte (1M NaOH) and lighting condition (AM 1.5, 100  $\text{mW}/\text{cm}^2$ ) is the same from (a) to (d).

In addition, the possibility of photoelectrochemical activation for  $\text{Co(OH)}_2$  was examined by replacing  $\text{Ta}_3\text{N}_5$  with other photoanode materials. The first choice is  $\text{Fe}_2\text{O}_3$ , which is a well-studied photoelectrode material that does not exhibit photocharging effect. As shown in Figure 3.4a, the photocurrent of  $\text{Fe}_2\text{O}_3$  with  $\text{Co(OH)}_2$  did not increase as a result of PEC water oxidation. A small increase (<5%) for the photocurrent of bare  $\text{Fe}_2\text{O}_3$  sample was observed, but it is mostly likely induced by the formation of  $\text{FeOOH}$  on the surface as a more effective water oxidation catalyst than  $\text{Fe}_2\text{O}_3$ .<sup>31</sup> Similar conclusions (no performance enhancement upon PEC) were obtained on  $\text{TiO}_2$  as well (Figure 3.4b), indicating that the activation of  $\text{Co(OH)}_2$  was not responsible for the performance enhancement of  $\text{Ta}_3\text{N}_5/\text{Co(OH)}_2$ .

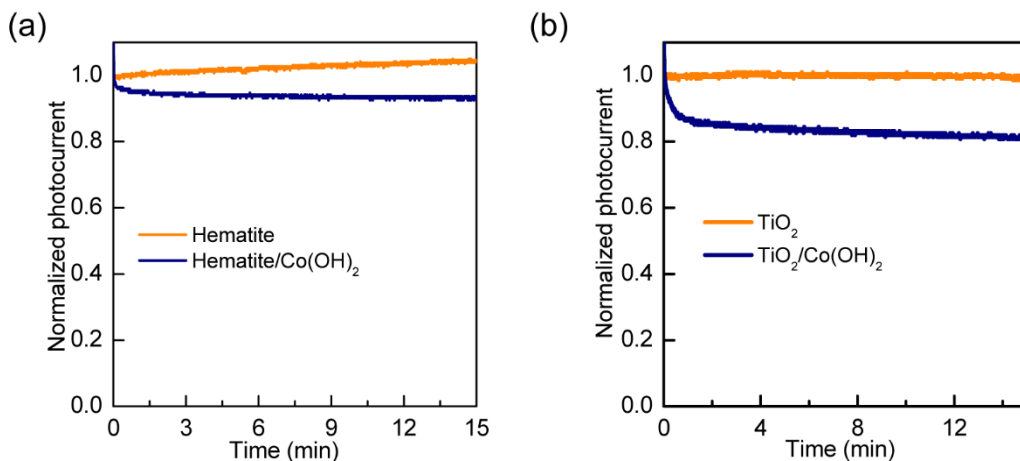


**Figure 3.4** Photocurrent density-time data for (a) hematite and (b)  $\text{TiO}_2$  with and without  $\text{Co(OH)}_2$  in 1 M NaOH at 1.23 V. The photocurrent was normalized to the value at the initial time.

### 3.3.2.2 $\text{Ta}_3\text{N}_5$ improvement

Next, experiments were conducted to understand whether  $\text{Ta}_3\text{N}_5$  was improved as a result of illumination under PEC conditions. Previously, the photocharging effect was observed on  $\text{BiVO}_4$ .<sup>23, 24</sup> For this portion of the work, photo-oxidation of  $\text{Fe(CN)}_6^{4-}$  instead of  $\text{H}_2\text{O}$

oxidation was employed. This is because as a hole scavenger  $\text{Fe}(\text{CN})_6^{4-}$  is expected to more effectively collect holes reaching the SCLI, thereby offering a reliable evaluation of the true properties of  $\text{Ta}_3\text{N}_5$ .<sup>32-34</sup> As shown in Figure 3.5, three different samples were compared, including as-made  $\text{Ta}_3\text{N}_5/\text{Co}(\text{OH})_2$  (**Sample 1**), bare  $\text{Ta}_3\text{N}_5$  prepared by dissolving  $\text{Co}(\text{OH})_2$  in as-made  $\text{Ta}_3\text{N}_5/\text{Co}(\text{OH})_2$  (**Sample 2**), and  $\text{Ta}_3\text{N}_5$  prepared by dissolving  $\text{Co}(\text{OH})_2$  in  $\text{Ta}_3\text{N}_5/\text{Co}(\text{OH})_2$  after PEC water oxidation (**Sample 3**). Two important observations were made. First, **Samples 1** and **2** exhibited similar performance. It indicates that the deposition and removal of  $\text{Co}(\text{OH})_2$  had little influence on  $\text{Ta}_3\text{N}_5$  itself. While careful examinations of the data may reveal slight differences in the onset characteristics (better performance for Sample 2), the difference is within the range of variations observed in different batches of samples. Second, **Sample 3** exhibited poorer performance than **Sample 2**. The result was surprising because  $\text{Ta}_3\text{N}_5/\text{Co}(\text{OH})_2$  after PEC test (but prior to the removal of  $\text{Co}(\text{OH})_2$ ) would exhibit better performance than **Sample 2** (see Figure 3.2). The results strongly support that  $\text{Co}(\text{OH})_2$  had to be present for the performance enhancement.

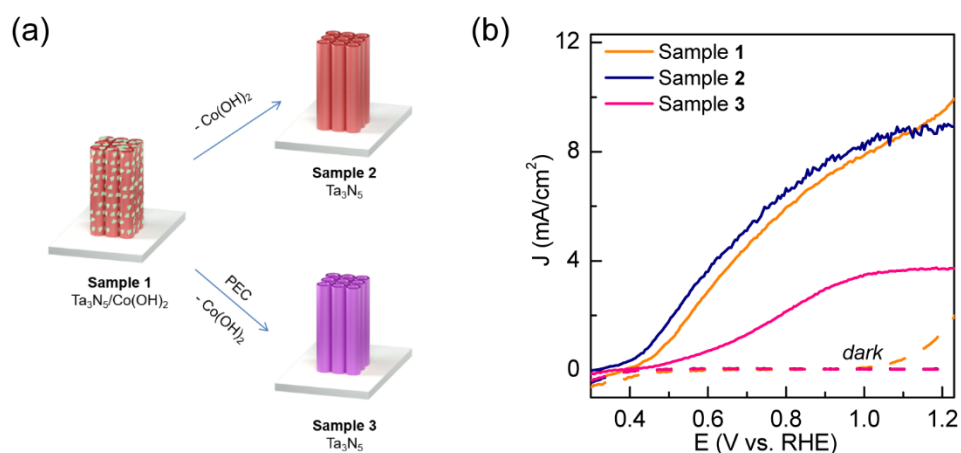


**Figure 3.5** (a) Schematic showed the compositions of sample 1 to 3. (b) J-V data of three different  $\text{Ta}_3\text{N}_5$  samples in 0.1 M phosphate buffer with 0.1 M  $\text{K}_4\text{Fe}(\text{CN})_6$  (pH 10). Sample 1, as-prepared  $\text{Ta}_3\text{N}_5/\text{Co}(\text{OH})_2$ ; sample 2,  $\text{Ta}_3\text{N}_5$  by

dissolving  $\text{Co(OH)}_2$  in  $\text{Ta}_3\text{N}_5/\text{Co(OH)}_2$ ; sample 3,  $\text{Ta}_3\text{N}_5$  by dissolving  $\text{Co(OH)}_2$  in  $\text{Ta}_3\text{N}_5/\text{Co(OH)}_2$  after PEC water oxidation. PEC water oxidation conditions: 20 consecutive CV scans from 0.4 to 1.43 V and 30 min photo-electrolysis at 1.23 V in 1 M NaOH.

### 3.3.2.3 Unique to the combination of $\text{Ta}_3\text{N}_5$ and $\text{Co(OH)}_2$

The last possibility was whether the effect is unique to the  $\text{Ta}_3\text{N}_5/\text{Co(OH)}_2$  combination. For this purpose,  $\text{Co(OH)}_2$  was replaced with other two popularly studied co-catalysts,  $\text{NiFeO}_x$  and Co-Pi.<sup>27, 35, 36</sup> Compared with  $\text{Ta}_3\text{N}_5/\text{Co(OH)}_2$ , both  $\text{Ta}_3\text{N}_5/\text{Co-Pi}$  and  $\text{Ta}_3\text{N}_5/\text{NiFeO}_x$  showed quick photocurrent decays during photoelectrolysis (Figure 3.6a). For instance, only 30% of the original photocurrent remained for  $\text{Ta}_3\text{N}_5/\text{Co-Pi}$  after 30 min photoelectrolysis. At this stage, it is still not fully understood what compositions in Co-Pi prevent it from reacting with  $\text{Ta}_3\text{N}_5$  the same way as  $\text{Co(OH)}_2$  under identical conditions, but the results are highly reproducible (observed on over 10 different batches of samples). The decay for  $\text{Ta}_3\text{N}_5/\text{NiFeO}_x$  was even more severe (12% of the original photocurrent remained). However, when  $\text{Co(OH)}_2$  was combined with  $\text{NiFeO}_x$ , similar phenomenon as in the  $\text{Co(OH)}_2$  case could be observed, but with 30% higher photocurrent density at 1.23 V and comparable stability (Figure 3.6b and c). Furthermore, when  $\text{Co(OH)}_2$  was combined with Co-Pi, the photocurrent density at 1.23 V could be improved to 6  $\text{mA/cm}^2$  (Figure 3.6d) with the adjustment of Co-Pi deposition time. The hybrid photoelectrode showed similar stability as  $\text{Ta}_3\text{N}_5/\text{Co(OH)}_2$ , which was much better than  $\text{Ta}_3\text{N}_5/\text{Co-Pi}$  alone (Figure 3.6e and f). In addition, although the stability of  $\text{Ta}_3\text{N}_5/\text{Co-Pi}$  in Figure 3.6e was better than that in Figure 3.6a with the deposition time increased, the trend of performance decay remained the same, which further revealed the important role of  $\text{Ta}_3\text{N}_5/\text{Co(OH)}_2$  interface to achieve good stability.

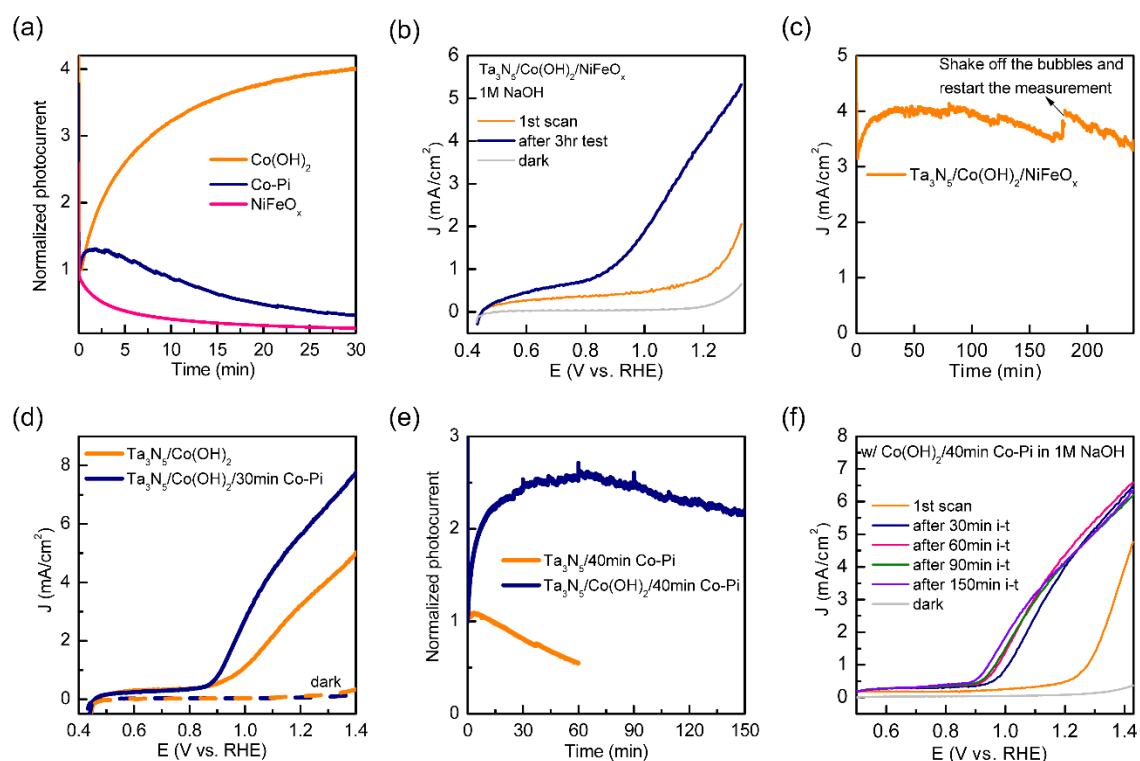


**Figure 3.6** (a) Photocurrent density-time data for  $\text{Ta}_3\text{N}_5$  with  $\text{Co}(\text{OH})_2$ ,  $\text{NiFeO}_x$ , and  $\text{Co-Pi}$  (10 min deposition time) catalyst in 1M NaOH at 1.23 V. The photocurrent density was normalized to the value at the initial time. (b) The negative to positive scan of the 1<sup>st</sup> CV and the one after 3hr potentiostatic test at 1.23 V for  $\text{Ta}_3\text{N}_5/\text{Co}(\text{OH})_2/\text{NiFeO}_x$ . (c) The photocurrent vs. time curve of  $\text{Ta}_3\text{N}_5/\text{Co}(\text{OH})_2/\text{NiFeO}_x$  at 1.23 V. 20 consecutive CV scans between 0.43 V and 1.33 V have been tested before the potentiostatic test. (d) J-V data of  $\text{Ta}_3\text{N}_5/\text{Co}(\text{OH})_2$  and  $\text{Ta}_3\text{N}_5/\text{Co}(\text{OH})_2/\text{Co-Pi}$  after photo-electrolysis at 1.23 V for 30 min in 1 M NaOH. The deposition time of Co-Pi was 30 min. (e) Photocurrent density-time data for  $\text{Ta}_3\text{N}_5/\text{Co-Pi}$  and  $\text{Ta}_3\text{N}_5/\text{Co}(\text{OH})_2/\text{Co-Pi}$  in 1 M NaOH at 1.23 V. The deposition time of Co-Pi was 40 min. (f) The J-V curves of  $\text{Ta}_3\text{N}_5/\text{Co}(\text{OH})_2/40$  min Co-Pi after different period of potentiostatic test at 1.23 V. The lighting conditions (AM 1.5 illumination at  $100 \text{ mW}/\text{cm}^2$ ) were the same from (a) to (f).

It has been previously reported that different degree of surface oxidation of  $\text{Ta}_3\text{N}_5$  would have different influence to the properties.<sup>37</sup> Because the extent of surface oxidation as a function of time was similar for  $\text{Ta}_3\text{N}_5/\text{Co}(\text{OH})_2$ ,  $\text{Ta}_3\text{N}_5/\text{NiFeO}_x$  and  $\text{Ta}_3\text{N}_5/\text{Co-Pi}$ , such an explanation is unlikely responsible for the observed performance enhancement (Figure 3.7a). Lastly we also studied whether the observed performance enhancement was a result of the reactions between  $\text{Ta}_3\text{N}_5$  and the precursor to  $\text{Co}(\text{OH})_2$ ,<sup>26</sup>

and it was found that the effect was not dependent on the type of precursors used (Figure 3.7b).

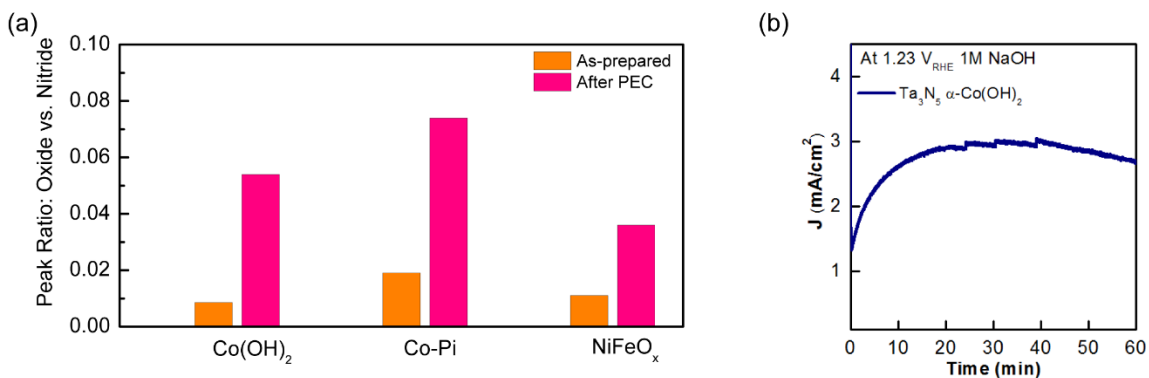


**Figure 3.7** (a) The peak ratio of surface tantalum oxide to tantalum nitride derived from XPS Ta 4f spectra. PEC test condition: 3 min photoelectrolysis at 1.23 V in 1 M NaOH under 100 mW/cm<sup>2</sup> illumination. (b) The photocurrent of Ta<sub>3</sub>N<sub>5</sub>/α-Co(OH)<sub>2</sub> at 1.23 V in 1 M NaOH as a function of PEC water oxidation time. Although the synthesis method of Co(OH)<sub>2</sub> has changed (details in the section 3.2.1), similar performance enhancement phenomenon can be observed.

### 3.3.3 Evolution of interfacial kinetics and energetics

To summarize the experimental observations to this point, a profound performance enhancement was obtained when Co(OH)<sub>2</sub>-coated Ta<sub>3</sub>N<sub>5</sub> was subjected to PEC reactions. The effect was unique to the Ta<sub>3</sub>N<sub>5</sub>/Co(OH)<sub>2</sub> combination, and light was critical. Inspired by the previous understanding in Chapter 2 that the rapid degradation of Ta<sub>3</sub>N<sub>5</sub> is due to surface Fermi level pinning as a result of displacement of N atoms by O, the surface energetics and kinetics were assessed by the open circuit potential (OCP) and intensity modulated photocurrent spectroscopy (IMPS) techniques, respectively. The goal was to observe whether the PEC treatment in the presence of Co(OH)<sub>2</sub> leads to reduced surface Fermi level pinning. Indeed, as shown in Figure 3.8a, the OCP of

Ta<sub>3</sub>N<sub>5</sub>/Co(OH)<sub>2</sub> as measured in light shifted negatively due to PEC reactions by 0.14 V, indicating that the surface Fermi level shifted toward the conduction band edge. The value was consistent with the change of V<sub>on</sub> (Figure 3.2a). In contrast, the OCP of bare Ta<sub>3</sub>N<sub>5</sub> showed positive shift after PEC water oxidation, indicating that the surface Fermi level has shifted toward the valence band edge due to surface oxidation.<sup>38</sup> In addition, the OCP of Ta<sub>3</sub>N<sub>5</sub>/Co(OH)<sub>2</sub> after EC treatment was more positive than the one after PEC treatment, further illustrating the unique effect of light on the surface energetics (Figure 3.8c). Taken as a whole, it was clearly observed that greater photovoltages by measuring the difference between the dark OCPs (Figure 3.8b) and light OCPs (Figure 3.8a) owing to the suppression of the Fermi level pinning effect.<sup>13</sup>

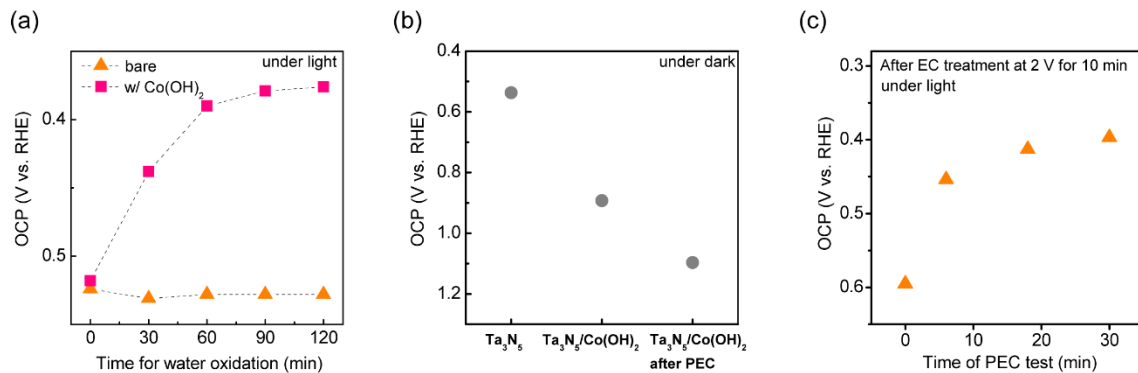


**Figure 3.8** (a) Light open-circuit potential of bare Ta<sub>3</sub>N<sub>5</sub> and Ta<sub>3</sub>N<sub>5</sub>/Co(OH)<sub>2</sub> with different photo-electrolysis times at 1.23 V in 1 M NaOH (AM 1.5 illumination at 100 mW/cm<sup>2</sup>). (b) The dark open-circuit potentials of bare Ta<sub>3</sub>N<sub>5</sub>, Ta<sub>3</sub>N<sub>5</sub>/Co(OH)<sub>2</sub> and Ta<sub>3</sub>N<sub>5</sub>/Co(OH)<sub>2</sub> after 30 min photoelectrolysis at 1.23 V in 1 M NaOH. (c) The light open-circuit potentials of Ta<sub>3</sub>N<sub>5</sub>/Co(OH)<sub>2</sub> after different PEC water oxidation time. Different from the as-prepared Ta<sub>3</sub>N<sub>5</sub>/Co(OH)<sub>2</sub> sample as shown in (a), the Ta<sub>3</sub>N<sub>5</sub>/Co(OH)<sub>2</sub> was first tested for electrochemical water oxidation at 2V for 10 min before the light open-circuit potential measurement.

The Nyquist plots obtained from IMPS was shown in Figure 3.9. Several assumptions are required to interpret the data (see section 1.7.1.3), which is supported by recent studies.<sup>39</sup> The data for Ta<sub>3</sub>N<sub>5</sub> and Ta<sub>3</sub>N<sub>5</sub>/Co(OH)<sub>2</sub> at different PEC test stages were

first normalized to the largest real photocurrent so that the highest intercept at the real photocurrent axis (x axis) is 1. The rate constant for hole transfer ( $k_{tran}$ ) as well as electron and hole recombination ( $k_{rec}$ ) on the photoelectrode surface can be obtained by the following equations:

$$TE = k_{tran}/(k_{tran} + k_{rec}) \quad (3.1)$$

$$\omega_{max} = k_{tran} + k_{rec} \quad (3.2)$$

In Equation (3.1), TE is the overall hole transfer efficiency. The value can be obtained from the intercept of low frequency end at the real photocurrent axis (in Figure 3.9). In some cases, where the low frequency end didn't intercept with the real photocurrent axis, the semicircle was fitted using the low frequency end and the highest intercept at the real photocurrent axis. In Equation (3.2),  $\omega_{max}$  is the frequency at the apex of the semicircle, in which the imaginary photocurrent reached the highest value. Together,  $k_{tran}$  and  $k_{rec}$  at each applied potential can be obtained.

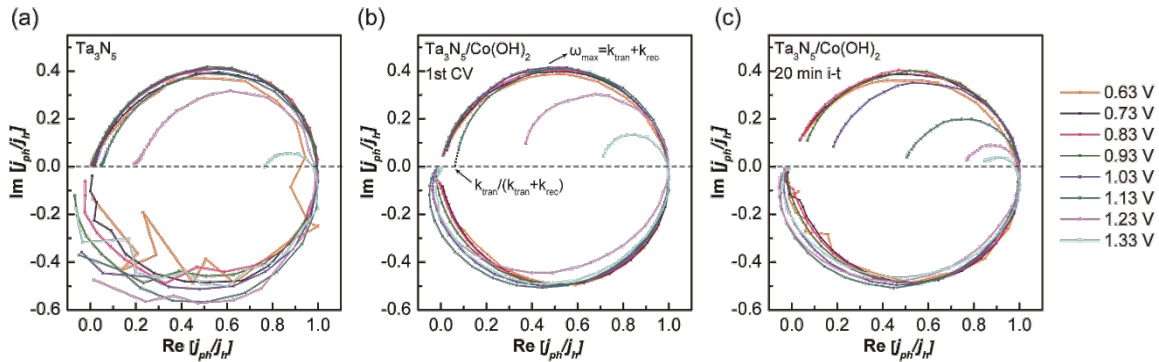


**Figure 3.9** Normalized IMPS response of (a) bare Ta<sub>3</sub>N<sub>5</sub>, (b) Ta<sub>3</sub>N<sub>5</sub>/Co(OH)<sub>2</sub> after one CV test, (c) Ta<sub>3</sub>N<sub>5</sub>/Co(OH)<sub>2</sub> after 20 min photoelectrolysis at 1.23 V. The low frequency intercept was determined by fitting the semicircle.

The IMPS data clearly confirmed that  $k_{rec}$  at 0.9 V decreased by a factor of 3 when the PEC treatment was extended from 1 CV scan to 20 min photoelectrolysis (Figure 3.10a). Bare Ta<sub>3</sub>N<sub>5</sub> featured  $k_{rec}$ 's 80 times higher than those of Ta<sub>3</sub>N<sub>5</sub>/Co(OH)<sub>2</sub>

after PEC treatment. Moreover, charge transfer kinetics was also improved after the PEC treatment, as supported by the increase of  $k_{tran}$  obtained from IMPS (Figure 3.10b) and the decrease of charge transfer resistance obtained from PEIS (Figure 3.10d). It should be noted that as an analytic tool designed to represent a simplified model with a simple photoelectrode|electrolyte interface, IMPS has inherent deficiencies in describing complex systems such as the one studied here. As such, the over-interpretation of the data in a quantitative fashion should be avoided. Taken as a whole, this set of data support that under PEC conditions, the presence of  $\text{Co(OH)}_2$  on  $\text{Ta}_3\text{N}_5$  leads to a better SCLI by not only decreasing surface recombination, but also increasing charge transfer.

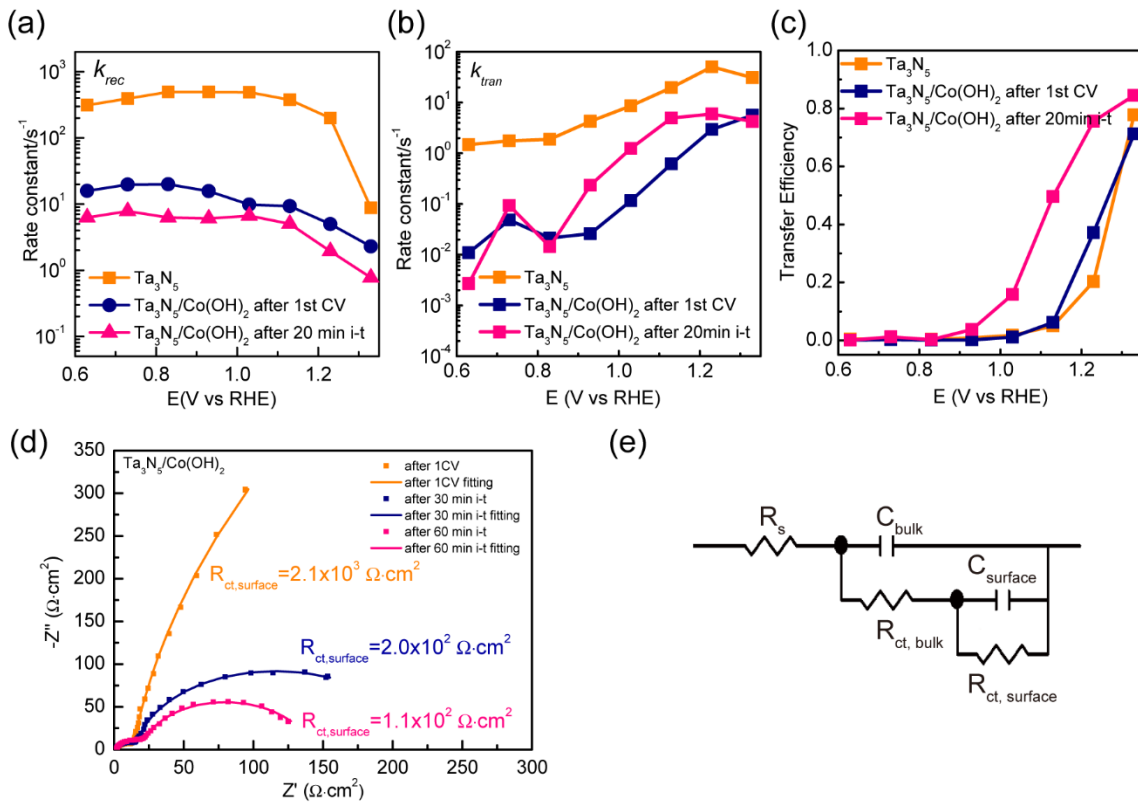


**Figure 3.10** (a) Charge recombination rate constants ( $k_{rec}$ ), (b) charge transfer rate constants ( $k_{tran}$ ) and (c) transfer efficiency (TE) of bare  $\text{Ta}_3\text{N}_5$ ,  $\text{Ta}_3\text{N}_5/\text{Co(OH)}_2$  after the first CV and after photoelectrolysis at 1.23 V in 1 M NaOH for 20 min. (d) The PEIS spectra of  $\text{Ta}_3\text{N}_5/\text{Co(OH)}_2$  after 1CV scan, 30 min and 60 min photoelectrolysis at 1.23 V in 1 M NaOH. The applied bias is 1 V. Lighting condition: AM 1.5 100 mW/cm<sup>2</sup>. (e) The equivalent circuit used to fit the

PEIS data. The equivalent circuit used for fitting is based on the study of hematite with Co-Pi catalyst.<sup>9</sup>  $R_s$  represents the series resistance of back electron transfer;  $C_{\text{bulk}}$  is the capacitance of the bulk  $\text{Ta}_3\text{N}_5$ ;  $R_{\text{ct, bulk}}$  is the charge transfer resistance within the depletion region;  $C_{\text{surface}}$  is the capacitance of  $\text{Ta}_3\text{N}_5/\text{Co}(\text{OH})_2$  surface;  $R_{\text{ct, surface}}$  is the charge transfer resistance on the surface. Clearly, the  $R_{\text{ct, surface}}$  decreased by one order of magnitude after 30 min photoelectrolysis, indicating the faster charge transfer from the photoelectrode to the electrolyte.

### 3.3.4 Probe the photo-induced interface

To further understand the origin of such an effect, XPS was used to probe the binding energies of Ta 4f electrons. The data for three samples with different histories (as-prepared, after PEC treatment and after EC treatment) are shown in Figure 3.11a. The peaks at 25.1 eV can be deconvoluted into three key components, including contributions from N-Ta-N, O-Ta-N and O-Ta-O bonding. For the as-prepared sample, the binding energies of each component was consistent with the literature reported values.<sup>40</sup> The position of each component remained the same after the EC treatment. However, after the PEC treatment, the peak representing O-Ta-O bonds shifted to the negative direction by 0.4 eV (red bar highlighted in the inset of the bottom panel in Figure 3.11a). The peak corresponding to O-Ta-N bonds showed a similar shift, but with a smaller magnitude (0.2 eV). By contrast, the peak assigned to N-Ta-N bonds shifted positively by ca. 0.1 eV, representing a shift of the surface Fermi level toward the conduction band edge. The result is consistent with the light OCP results as shown in Figure 3.8a. The negative shift of the O-Ta-O and O-Ta-N binding energies after PEC treatment may be explained by the interaction of Co with Ta in the form of Ta-O-Co bonding, in which case the introduction of Co weakened the neighboring Ta-O bonding, thus leading to smaller binding energies of Ta. Similar shifts of binding energies have been reported for Ti-O-Co bond

formation.<sup>41</sup> It is envisioned that highly surface sensitive spectroscopic techniques such as attenuated total reflectance IR (ATR) or synchrotron-enabled extended X-ray absorption fine structure spectroscopy (EXAFS) may be used in the future to provide more details of the bonding nature. It is noted that when  $\text{Co(OH)}_2$  was removed, the binding energies of all three components (N-Ta-N, O-Ta-N, and O-Ta-O bonds) were the same as the as-prepared sample (Figure 3.11b to e), providing further strong support that the  $\text{Ta}_3\text{N}_5/\text{Co(OH)}_2$  combination is unique to the unusual performance enhancement observed here.

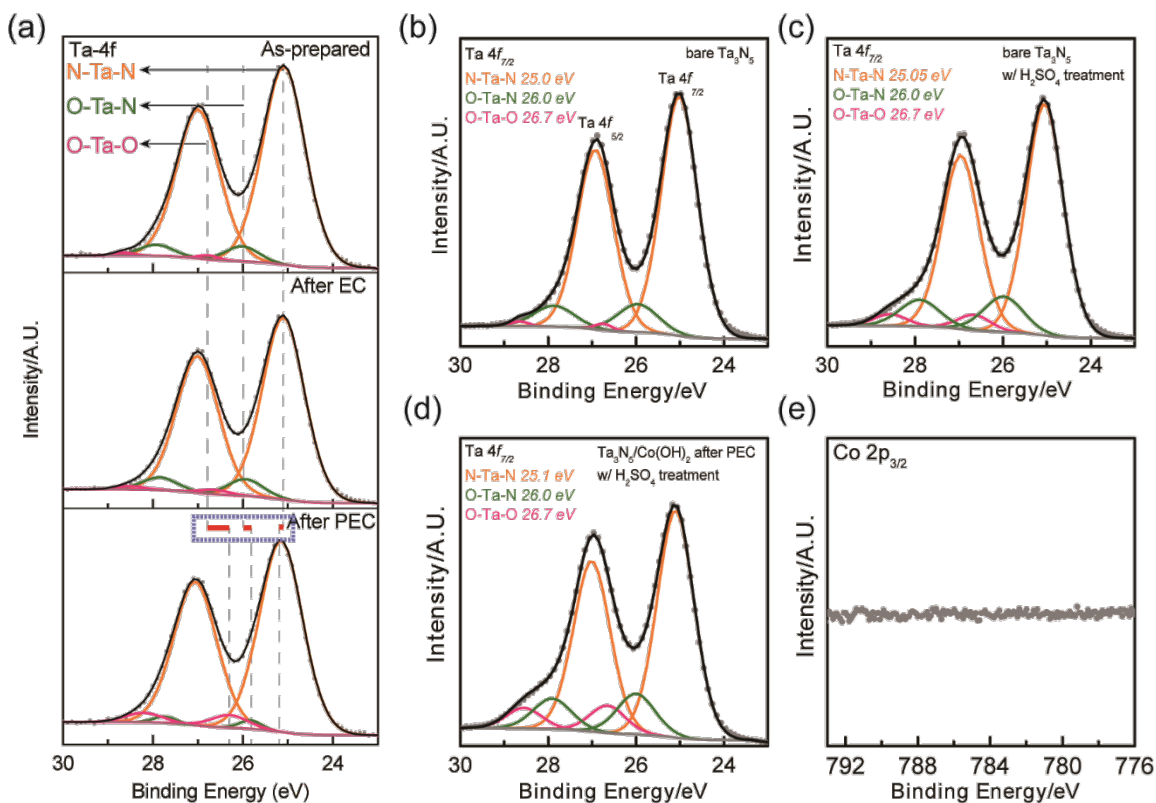


**Figure 3.11** (a) Ta 4f XPS spectra of  $\text{Ta}_3\text{N}_5/\text{Co(OH)}_2$  as-prepared, and after EC treatment and PEC treatment. The shifts of the individual components are highlighted in the bottom panel. EC treatment, 1.7 V in 1 M NaOH for 1 hr; PEC treatment, 1.23 V in 1 M NaOH for 30 min. The XPS Ta 4f peak for (b) bare  $\text{Ta}_3\text{N}_5$ , (c) bare  $\text{Ta}_3\text{N}_5$  after the  $\text{H}_2\text{SO}_4$  treatment and (d)  $\text{Ta}_3\text{N}_5/\text{Co(OH)}_2$  after 30 min photoelectrolysis at 1.23 V and after the  $\text{H}_2\text{SO}_4$  treatment.  $\text{H}_2\text{SO}_4$  treatment: immersing the electrode in 1M  $\text{H}_2\text{SO}_4$  under 90 °C for 10 min. (e) The XPS Co 2p spectra for sample in (d).

The peak positions of Ta  $4f_{7/2}$  for different components were also listed, which is almost the same as the as-prepared Ta<sub>3</sub>N<sub>5</sub>/Co(OH)<sub>2</sub> samples.

### 3.3.5 Mechanism for the photo-induced interface

To explain the unusual phenomenon as summarized above, a mechanism is proposed as shown in Figure 3.12a. Previous research and Chapter 2 has shown that surface oxidation of Ta<sub>3</sub>N<sub>5</sub> leads to severe surface Fermi level pinning and is the key reason for the rapid performance degradation under PEC or EC conditions (top route in Figure 3.12a).<sup>38, 42, 43</sup> It is understood that the presence of Co(OH)<sub>2</sub> promotes for the formation of Ta-O-Co bonds instead of Ta-O-Ta ones. It is nonetheless curious that such an effect was only observed when light was present. To illustrate the critical role of light, O• radical formation under PEC conditions is proposed to be the key. As shown in Figure 3.12a, the Ta-O-Co bonds are less likely to form under EC conditions due to the lack of O• radicals in the absence of light.<sup>44</sup> To support this hypothesis, control experiments were carried out in the electrolyte with hole scavengers. It has been shown previously that the formation of O• radical was an important step for photocatalytic water oxidation on semiconductors such as TiO<sub>2</sub> and TaON.<sup>44, 45</sup> When an efficient hole scavenger was present in the electrolyte, such as Fe(CN)<sub>6</sub><sup>4-</sup>, direct valence band hole transfer to solution would dominate under PEC conditions, bypassing water oxidation processes and possibly eliminating radical formation.<sup>46</sup> Based on this rationale, it is expected that if the formation of Ta-O-Co bond indeed requires O• radical as a water oxidation intermediate, the presence of hole scavenger would inhibit its formation. Indeed, as shown in Figure 3.12b and c, Ta<sub>3</sub>N<sub>5</sub>/Co(OH)<sub>2</sub> tested with hole scavengers showed much worse

performance compared to the one without hole scavengers (1M NaOH only) under otherwise identical PEC conditions. Nevertheless, it is noted that more direct evidence to support the radical mediated interface behavior still requires the detection of the  $O^\bullet$  radicals. For example, in-situ electron spin resonance (ESR) spectroscopy can be an effective method for this goal.<sup>47, 48</sup>

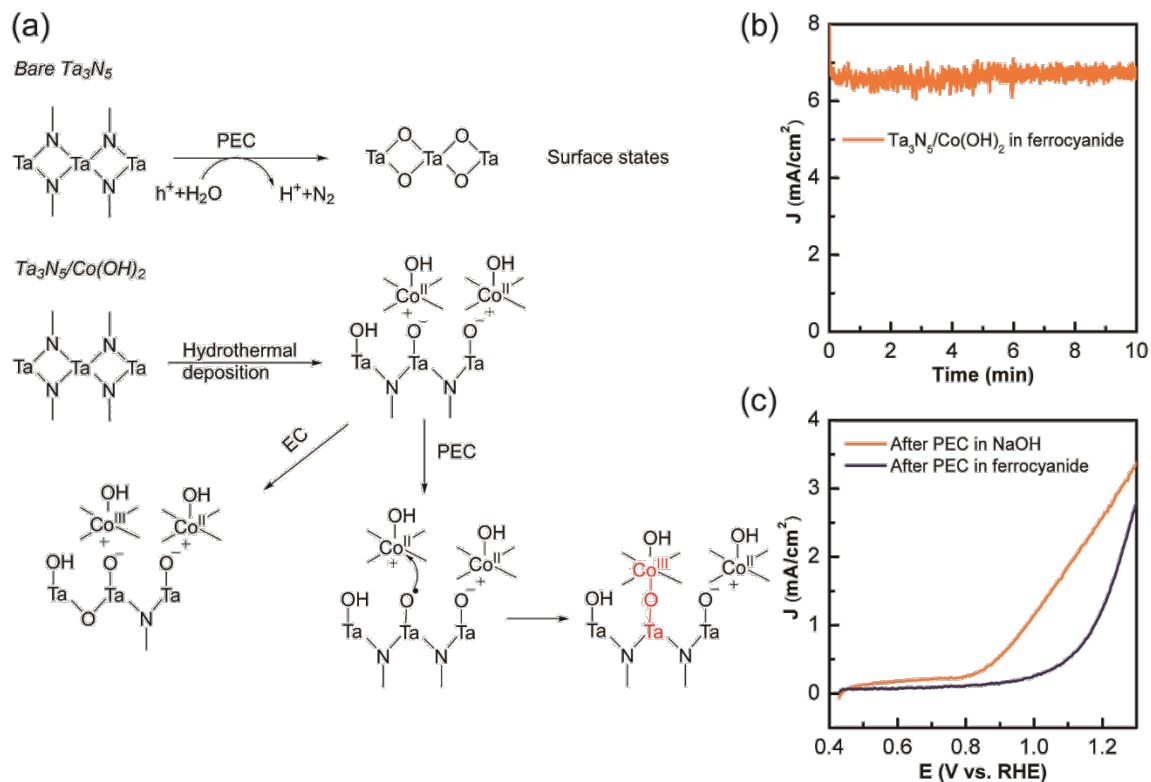


**Figure 3.12** (a) Proposed mechanism for the formation of the Ta-O-Co bond under PEC conditions. The surface oxidation of bare Ta<sub>3</sub>N<sub>5</sub> and the electrochemical oxidation of Ta<sub>3</sub>N<sub>5</sub>/Co(OH)<sub>2</sub> are included for comparison. (b) The photocurrent vs. time for Ta<sub>3</sub>N<sub>5</sub>/Co(OH)<sub>2</sub> at 1.23 V in 1 M NaOH with 0.1 M Fe(CN)<sub>6</sub><sup>4-</sup>; (c) The J-V of Ta<sub>3</sub>N<sub>5</sub>/Co(OH)<sub>2</sub> after potentiostatic test at 1.23 V in 1 M NaOH or 1 M NaOH with 0.1 M Fe(CN)<sub>6</sub><sup>4-</sup>. Illumination condition: AM 1.5 with 100 mW/cm<sup>2</sup>.

### 3.4 SUMMARY

In summary, a unique phenomenon has been observed that the water oxidation performance of Ta<sub>3</sub>N<sub>5</sub>/Co(OH)<sub>2</sub> photoanode is improved under PEC conditions. The result is highly different from bare Ta<sub>3</sub>N<sub>5</sub>, which would undergo rapid performance degradation. Experimental characterization confirmed that the effect is due to the unique chemical interactions between Ta<sub>3</sub>N<sub>5</sub> and Co(OH)<sub>2</sub> in the presence of light, which leads to reduced surface Fermi level pinning and the reduction of surface charge recombination as well as the increase of surface charge transfer. An O• radical-mediated Ta-O-Co formation is proposed to explain the unusual phenomenon. In addition, with the combination of Co(OH)<sub>2</sub> as the immediate contact layer to Ta<sub>3</sub>N<sub>5</sub> and another highly effective water oxidation catalyst (NiFeO<sub>x</sub> or Co-Pi) as the outer layer, both good stability and high photocurrent was achieved on Ta<sub>3</sub>N<sub>5</sub>.

### 3.5 REFERENCE

1. M. R. Hoffmann, S. T. Martin, W. Choi and D. W. Bahnemann, *Chem. Rev.*, 1995, **95**, 69-96.
2. T. Hisatomi, J. Kubota and K. Domen, *Chem. Soc. Rev.*, 2014, **43**, 7520-7535.
3. M. G. Walter, E. L. Warren, J. R. McKone, S. W. Boettcher, Q. Mi, E. A. Santori and N. S. Lewis, *Chem. Rev.*, 2010, **110**, 6446-6473.
4. C. Ding, J. Shi, Z. Wang and C. Li, *ACS Catal.*, 2017, **7**, 675-688.
5. T. A. Pham, Y. Ping and G. Galli, *Nat. Mater.*, 2017, **16**, 401-408.
6. C. Du, M. Zhang, J.-W. Jang, Y. Liu, G.-Y. Liu and D. Wang, *J. Phys. Chem. C*, 2014, **118**, 17054-17059.
7. W. Li, D. He, S. W. Sheehan, Y. He, J. E. Thorne, X. Yao, G. W. Brudvig and D. Wang, *Energy Environ. Sci.*, 2016, **9**, 1794-1802.
8. J. E. Thorne, J.-W. Jang, E. Y. Liu and D. Wang, *Chem. Sci.*, 2016, **7**, 3347-3354.

9. B. Klahr, S. Gimenez, F. Fabregat-Santiago, J. Bisquert and T. W. Hamann, *J. Am. Chem. Soc.*, 2012, **134**, 16693-16700.
10. B. Klahr, S. Gimenez, F. Fabregat-Santiago, T. Hamann and J. Bisquert, *J. Am. Chem. Soc.*, 2012, **134**, 4294-4302.
11. J.-W. Jang, C. Du, Y. Ye, Y. Lin, X. Yao, J. Thorne, E. Liu, G. McMahon, J. Zhu, A. Javey, J. Guo and D. Wang, *Nat. Commun.*, 2015, **6**, 7447.
12. W. Li, S. W. Sheehan, D. He, Y. He, X. Yao, R. L. Grimm, G. W. Brudvig and D. Wang, *Angew. Chem. Int. Ed.*, 2015, **54**, 11428-11432.
13. J. E. Thorne, S. Li, C. Du, G. Qin and D. Wang, *J. Phys. Chem. Lett.*, 2015, **6**, 4083-4088.
14. X. Yang, R. Liu, Y. He, J. Thorne, Z. Zheng and D. Wang, *Nano Res.*, 2015, **8**, 56-81.
15. J. L. White, M. F. Baruch, J. E. Pander, Y. Hu, I. C. Fortmeyer, J. E. Park, T. Zhang, K. Liao, J. Gu, Y. Yan, T. W. Shaw, E. Abelev and A. B. Bocarsly, *Chem. Rev.*, 2015, **115**, 12888-12935.
16. M. Liao, J. Feng, W. Luo, Z. Wang, J. Zhang, Z. Li, T. Yu and Z. Zou, *Adv. Funct. Mater.*, 2012, **22**, 3066-3074.
17. Y. Li, L. Zhang, A. Torres-Pardo, J. M. González-Calbet, Y. Ma, P. Oleynikov, O. Terasaki, S. Asahina, M. Shima, D. Cha, L. Zhao, K. Takane, J. Kubota and K. Domen, *Nat. Commun.*, 2013, **4**, 2566.
18. I. Narkeviciute, P. Chakthranont, A. J. M. Mackus, C. Hahn, B. A. Pinaud, S. F. Bent and T. F. Jaramillo, *Nano Lett.*, 2016, **16**, 7565-7572.
19. L. Wang, F. Dionigi, N. T. Nguyen, R. Kirchgeorg, M. Gliech, S. Grigorescu, P. Strasser and P. Schmuki, *Chem. Mater.*, 2015, **27**, 2360-2366.
20. G. Liu, J. Shi, F. Zhang, Z. Chen, J. Han, C. Ding, S. Chen, Z. Wang, H. Han and C. Li, *Angew. Chem. Int. Ed.*, 2014, **53**, 7295-7299.
21. G. Liu, P. Fu, L. Zhou, P. Yan, C. Ding, J. Shi and C. Li, *Chem. Eur. J.*, 2015, **21**, 9624-9628.
22. M. Zhong, T. Hisatomi, Y. Sasaki, S. Suzuki, K. Teshima, M. Nakabayashi, N. Shibata, H. Nishiyama, M. Katayama, T. Yamada and K. Domen, *Angew. Chem. Int. Ed.*, 2017, **56**, 4739-4743.
23. T. Li, J. He, B. Peña and C. P. Berlinguette, *Angew. Chem. Int. Ed.*, 2016, **55**, 1769-1772.
24. B. J. Trzesniewski and W. A. Smith, *J. Mater. Chem. A*, 2016, **4**, 2919-2926.
25. G. S. Hutchings, Y. Zhang, J. Li, B. T. Yonemoto, X. Zhou, K. Zhu and F. Jiao, *J. Am. Chem. Soc.*, 2015, **137**, 4223-4229.
26. Z. Liu, R. Ma, M. Osada, K. Takada and T. Sasaki, *J. Am. Chem. Soc.*, 2005, **127**, 13869-13874.
27. R. D. L. Smith, M. S. Prévot, R. D. Fagan, Z. Zhang, P. A. Sedach, M. K. J. Siu, S. Trudel and C. P. Berlinguette, *Science*, 2013, **340**, 60-63.
28. Y. Lin, S. Zhou, X. Liu, S. Sheehan and D. Wang, *J. Am. Chem. Soc.*, 2009, **131**, 2772-2773.
29. L. Trotochaud, S. L. Young, J. K. Ranney and S. W. Boettcher, *J. Am. Chem. Soc.*, 2014, **136**, 6744-6753.
30. M. S. Burke, M. G. Kast, L. Trotochaud, A. M. Smith and S. W. Boettcher, *J. Am. Chem. Soc.*, 2015, **137**, 3638-3648.

31. J. S. Kang, Y. Noh, J. Kim, H. Choi, T. H. Jeon, D. Ahn, J.-Y. Kim, S.-H. Yu, H. Park, J.-H. Yum, W. Choi, D. C. Dunand, H. Choe and Y.-E. Sung, *Angew. Chem. Int. Ed.*, 2017, **56**, 6583-6588.
32. A. Ishikawa, T. Takata, J. N. Kondo, M. Hara and K. Domen, *J. Phys. Chem. B*, 2004, **108**, 11049-11053.
33. D. K. Zhong, S. Choi and D. R. Gamelin, *J. Am. Chem. Soc.*, 2011, **133**, 18370-18377.
34. Q. Cheng, W. Fan, Y. He, P. Ma, S. Vanka, S. Fan, Z. Mi and D. Wang, *Adv. Mater.*, 2017, **29**, 1700312.
35. C. Du, X. Yang, M. T. Mayer, H. Hoyt, J. Xie, G. McMahon, G. Bischoping and D. Wang, *Angew. Chem. Int. Ed.*, 2013, **52**, 12692-12695.
36. M. W. Kanan and D. G. Nocera, *Science*, 2008, **321**, 1072.
37. G. Liu, S. Ye, P. Yan, F.-Q. Xiong, P. Fu, Z. Wang, Z. Chen, J. Shi and C. Li, *Energy Environ. Sci.*, 2016, **9**, 1327-1334.
38. Y. He, J. E. Thorne, C. H. Wu, P. Ma, C. Du, Q. Dong, J. Guo and D. Wang, *Chem*, 2016, **1**, 640-655.
39. F. Le Formal, E. Pastor, S. D. Tilley, C. A. Mesa, S. R. Pendlebury, M. Grätzel and J. R. Durrant, *J. Am. Chem. Soc.*, 2015, **137**, 6629-6637.
40. M. Hara, E. Chiba, A. Ishikawa, T. Takata, J. N. Kondo and K. Domen, *J. Phys. Chem. B*, 2003, **107**, 13441-13445.
41. B. Bharti, S. Kumar, H.-N. Lee and R. Kumar, *Sci. Rep.*, 2016, **6**, 32355.
42. E. Watanabe, H. Ushiyama and K. Yamashita, *ACS Appl. Mater. Interfaces*, 2017, **9**, 9559-9566.
43. H. X. Dang, N. T. Hahn, H. S. Park, A. J. Bard and C. B. Mullins, *J. Phys. Chem. C*, 2012, **116**, 19225-19232.
44. R. Nakamura, T. Tanaka and Y. Nakato, *J. Phys. Chem. B*, 2005, **109**, 8920-8927.
45. R. Nakamura and Y. Nakato, *J. Am. Chem. Soc.*, 2004, **126**, 1290-1298.
46. B. Klahr, S. Gimenez, F. Fabregat-Santiago, J. Bisquert and T. W. Hamann, *Energy Environ. Sci.*, 2012, **5**, 7626-7636.
47. Z. Li, C. Kong and G. Lu, *J. Phys. Chem. C*, 2016, **120**, 56-63.
48. V. Brezová, D. Dvoranová and A. Staško, *Res. Chem. Intermed.*, 2007, **33**, 251-268.

Chapter 3 is adapted with permission from “Y. He, P. Ma, S. Zhu, M. Liu, Q. Dong, J. Espano, X. Yao and D. Wang, *Joule*, 2017, **1**, 831-842.” Copyright 2017 Elsevier.

## **CHAPTER 4 DEPENDENCE OF INTERFACE ENERGETICS AND KINETICS ON CATALYST LOADING IN A PHOTOELECTROCHEMICAL SYSTEM**

### **4.1 INTERFACIAL STUDY IN A COMPLEX PEC SYSTEM**

In a “simplistic” form, a PEC system usually consists of one or more semiconductor(s) as the light absorber(s), catalysts to drive the water splitting reactions and, often than not, protection layers to slow down or, ideally, prevent (photo)corrosions.<sup>1,2</sup> It is increasingly recognized that a working system is likely one composed of multiple components. The interface between the various components, including that at photoelectrode|electrolyte, is of paramount importance to the proper function of the integrated system. Such an insight has inspired significant research activities to understand the interface behaviors of a PEC system, as mentioned in section 1.7.1 in Chapter 1. These studies have led to a general consensus that the application of co-catalysts either reduces surface recombination on the photoelectrode or facilitates charge transfer or both. However, few prior studies have shown a fundamental difference between low and high catalyst loadings. Here an intriguing observation was found where the surface energetics appears to depend on the catalyst loading amount, with high catalyst loading not only affecting interface kinetics but also energetics. Most interestingly, such a dependence was only observed when a protection layer was present.

The prototypical study platform employed by this study was a Si photocathode. Earlier research has shown that GaN nanowires, grown by molecular beam epitaxy (MBE), could serve as an effective protection layer to permit highly stable operations for up to 113 hours under hydrogen evolution conditions in acidic solutions (0.5 M H<sub>2</sub>SO<sub>4</sub>)<sup>3</sup>. Notably, the study platform features a buried n<sup>+</sup>/p junction, which represents one of the best developed in terms of technology readiness levels (TRL) for practical solar hydrogen generation. Canonical semiconductor physics would predict that the energetics of such a buried junction should be insensitive to environments beyond the semiconductor/protection layer. However, the results in this Chapter prove otherwise. At low loading amount of Pt (e.g., 0.01 μg/cm<sup>2</sup>), a low photovoltage (0.41 V) was measured; at high loading amount of Pt (e.g., 4 μg/cm<sup>2</sup>), a higher photovoltage (0.57 V) was measured. The surprising discovery sheds new lights on how the energetics is defined by recombination at the Si/GaN interface and reveals that careful optimization would be critical for systems even with buried junctions. Control experiments where the GaN protection layer was absent showed no such dependence on catalyst loading amount, which helps see why the phenomenon was not reported previously.

## 4.2 MATERIALS AND METHODS

### 4.2.1 Material synthesis

The synthesis method for GaN/n<sup>+</sup>p-Si photocathodes has been reported previously<sup>3-7</sup>. Briefly, it consists of planar n<sup>+</sup>p-Si substrate and n<sup>+</sup>-GaN nanowire arrays. The n<sup>+</sup>p-Si

was prepared from p-Si (100) substrate using a standard thermal diffusion process. The n<sup>+</sup>-GaN nanowires were grown on n<sup>+</sup>p-Si substrates via plasma-assisted molecular beam epitaxy (PAMBE) under growth temperatures between 700 – 750 °C for 120 min. The plasma power was maintained at 350 W, with a Ga beam equivalent pressure of  $6 \times 10^{-8}$  Torr and a nitrogen flow rate of 1 sccm (standard cubic centimeter per minute).

The Si nanowires (NWs) without GaN as a control were prepared by electroless etching method reported previously <sup>8-10</sup>. Typically, the p-Si (100) wafer was cleaned sequentially in acetone, methanol, isopropanol and then oxidized in H<sub>2</sub>O<sub>2</sub>/H<sub>2</sub>SO<sub>4</sub> (v/v 1:3) at 90 °C for 15 min to remove heavy metals and organic species. Then the Si wafer was immersed into an HF/AgNO<sub>3</sub> solution (4.6 M HF and 0.02 M AgNO<sub>3</sub>) for 30 min at 50 °C. The Ag residue was removed using HNO<sub>3</sub> (70 % w/w) for 20 min. Once prepared, the Si NWs were etched in HF (aqueous, 5%) for 2 min and dried in a stream of N<sub>2</sub>. To make ohmic contact, Al (300 nm) was sputtered onto the backside of Si substrates by radio frequency magnetron sputtering. Finally, the samples were annealed in flowing Ar (5000 sccm) at 450 °C for 5 min.

For GaN/n<sup>+</sup>p-Si, one drop of Ga-In eutectic ( $\geq 99.99\%$ ; Sigma-Aldrich) was spread on the backside of the Si substrate, with a tinned Cu wire secured to it using Ag epoxy (M.G. Chemicals). Non-conductive hysol epoxy (Loctite 615) was used to seal the sample, with exposed surface area of ca. 0.1 cm<sup>2</sup>. The fabrication of Si NWs photoelectrode followed a similar procedure without using the Ga-In eutectic.

For Pt on GaN/n<sup>+</sup>p-Si photocathodes, a photoelectrochemical deposition method was used. It was carried out with a potentiostat (Modulab<sup>®</sup> XM coupled with Modulab<sup>®</sup> XM ECS software) in a three-electrode configuration, with GaN/n<sup>+</sup>p-Si as the working

electrode, Ag/AgCl as the reference electrode and glass coated with fluorine-doped tin oxide (FTO) as the counter electrode. During the deposition, the working electrode was kept at 0 V vs. RHE (all potentials henceforth in this Chapter are vs. RHE unless noted) in 0.5 M H<sub>2</sub>SO<sub>4</sub> with varying concentrations of H<sub>2</sub>PtCl<sub>6</sub> (5 – 500 μM) for different periods of time (10 – 600 s). During the deposition, the electrode was illuminated by an AM 1.5 solar simulator (100 mW/cm<sup>2</sup>, Solarlight Model 16S-300-M Air Mass Solar Simulator). After deposition, the electrode was rinsed with DI water and dried with N<sub>2</sub>.

For Pt on Si NWs without GaN, an electroless deposition method was utilized <sup>11</sup>. First, the Si NWs electrode was etched in 5% HF aqueous solution for 2 min to remove surface oxides. It was then immediately immersed into 0.4 M HF solutions with different concentrations of H<sub>2</sub>PtCl<sub>6</sub> (1 – 1000 μM) for 30 s. Afterwards, the electrode was rinsed with DI water and dried with N<sub>2</sub>.

#### **4.2.2 PEC measurement**

IMPS and LSV were conducted in a two-chamber glass cell separated by a Nafion membrane (Nafion 211; Fuel Cell Store) in a three-electrode configuration. In one chamber, the photocathode was exposed to illumination with saturated calomel electrode (SCE) on the side as the reference electrode. In the other chamber, a Pt mesh was used as the counter electrode. The electrolyte, 0.5 M H<sub>2</sub>SO<sub>4</sub>, was purged by N<sub>2</sub> (99.999%; Airgas) for 30 min before and continuously during the measurement to remove dissolved oxygen. The electrolyte was stirred during all measurements. For IMPS, a ModuLab<sup>®</sup> XM potentiostat (with the ModuLab<sup>®</sup> XM DSSC software) including a frequency response analyzer (FRA) and a 405 nm LED (ThorLabs, with a power of 26 mW/cm<sup>2</sup>)

was used. The spectra were collected using a 10% light intensity modulation, and the frequency of modulation was varied from 10 kHz to 0.1 Hz. For LSV, the light source was changed to simulated solar light (Solarlight Model 16S-300-M Air Mass Solar Simulator) at 100 mW/cm<sup>2</sup>. The potential was swept from negative to positive, at a rate of 10 mV/s. The OCP was recorded using a potentiostat (CH Instruments CHI604C) in the fume hood. The electrolyte was continuously stirred and purged with H<sub>2</sub> to maintain a reversible HER condition at or near the standard conditions. The light source was an AM 1.5 solar simulator (100 mW/cm<sup>2</sup>, Newport Oriel 96000).

For IMPS and OCP measurements, each data point was the average of at least three different electrodes, the error bars being the variations between the maximum/minimum measured values.

### **4.2.3 Material characterization**

A field-emission scanning electron microscope (SEM, JEOL 6340F) at 10 kV and a transmission electron microscope (TEM, JEOL 2010F) at 200 kV were used for sample imaging. The surface species were measured by X-ray photoelectron spectroscopy (K-alpha<sup>+</sup> XPS, Thermo Scientific, Al K $\alpha$  = 1486.7 eV). The loading amount of Pt was determined by inductively coupled plasma optical emission spectrometry (ICP-OES, Agilent 5100 ICP-OES). Before each measurement, the photocathodes with Pt were soaked in 0.5 mL aqua regia (70 wt% HNO<sub>3</sub>:37 wt% HCl=1:4 v/v) for 24 h to dissolve Pt. Then 6 mL of DI water was added to dilute the aqua regia.

## 4.3 RESULTS AND DISCUSSIONS

### 4.3.1 Controlling Pt loading amount and the corresponding PEC performance

PEC deposition was carried out to deposit Pt on GaN/n<sup>+</sup>p-Si. The TEM images (Figure 4.1) showed that Pt nanoparticles (NPs) were distributed along the GaN nanowires with diameters of 2 to 4 nm, indicating the efficient charge transfer from Si to GaN during Pt deposition. As reported recently on a similar material platform, it is important to note that Pt was only deposited on GaN, which completely covered the surface of Si prior to forming nanowires<sup>3</sup>. Based on the TEM data, the number of Pt NPs increased with higher H<sub>2</sub>PtCl<sub>6</sub> concentrations and longer deposition times. Furthermore, Pt 4f<sub>7/2</sub> XPS spectrum for GaN/n<sup>+</sup>p-Si after Pt deposition showed the peak position at the binding energy of 70.5 eV, indicating the metallic nature of Pt NPs. To quantitatively determine the Pt loading amount, ICP-OES was applied. As shown in Figure 4.1k, the Pt loading amount could be tuned from 0.01 to 4 μg/cm<sup>2</sup> on GaN/n<sup>+</sup>p-Si by varying the deposition conditions. Note that the loading amount was normalized to the geometric area of the photoelectrode.

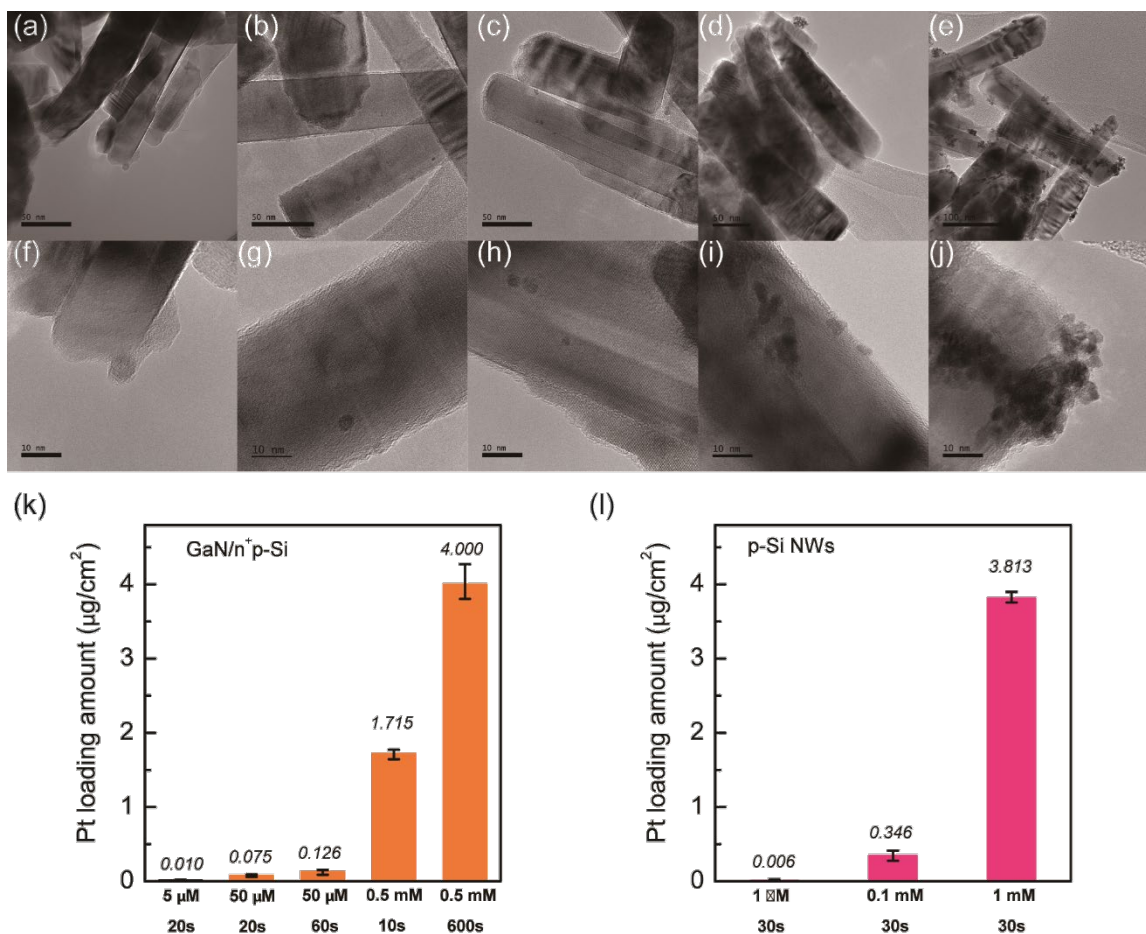


**Figure 4.1** The TEM images of GaN nanowires peeled off from GaN/n<sup>+</sup>p-Si with different Pt deposition conditions. (a, f) 5 µM H<sub>2</sub>PtCl<sub>6</sub> for 20 s; (b, g) 50 µM H<sub>2</sub>PtCl<sub>6</sub> for 20 s; (c, h) 50 µM H<sub>2</sub>PtCl<sub>6</sub> for 60 s; (d, i) 0.5 mM H<sub>2</sub>PtCl<sub>6</sub> for 10 s; (e, j) 0.5 mM H<sub>2</sub>PtCl<sub>6</sub> for 600 s. Scale bar: 50 nm (a-e) and 10 nm (f-j). Pt loading amount determined by ICP-OES for (k) GaN/n<sup>+</sup>p-Si and (l) p-Si NWs photocathodes under different H<sub>2</sub>PtCl<sub>6</sub> concentrations and deposition times. The error bars represent the difference among three separate measurements.

To understand how the Pt loading amount impacts the performance of photocathodes, LSV was used to investigate the PEC behaviors. The photocurrent densities vs. applied potentials (*J*-*V*) for GaN/n<sup>+</sup>p-Si with different Pt loading amount were plotted in Figure 4.2a. Two parameters, the turn-on potential (*V*<sub>on</sub>) and the fill factor (*FF*), were extracted from the *J*-*V* curves, and the results were summarized in Table 4.1. Here *V*<sub>on</sub> was defined as the potential where reduction photocurrent showed up (Figure

4.2c). The photovoltage ( $V_{ph}$ ) was defined as the difference between the  $V_{on}$  and the equilibrium HER potential, which was 0 V vs. RHE. The calculation method for  $FF$  was based on equation (4.1).

$$FF = P_{max}/(J_{sc} \times V_{on}) \quad (4.1)$$

$P_{max}$  is the maximum power point, which is the highest absolute value of photocurrent density multiplied with the applied potential.  $J_{sc}$  is the photocurrent density at the equilibrium hydrogen evolution potential (0 V).

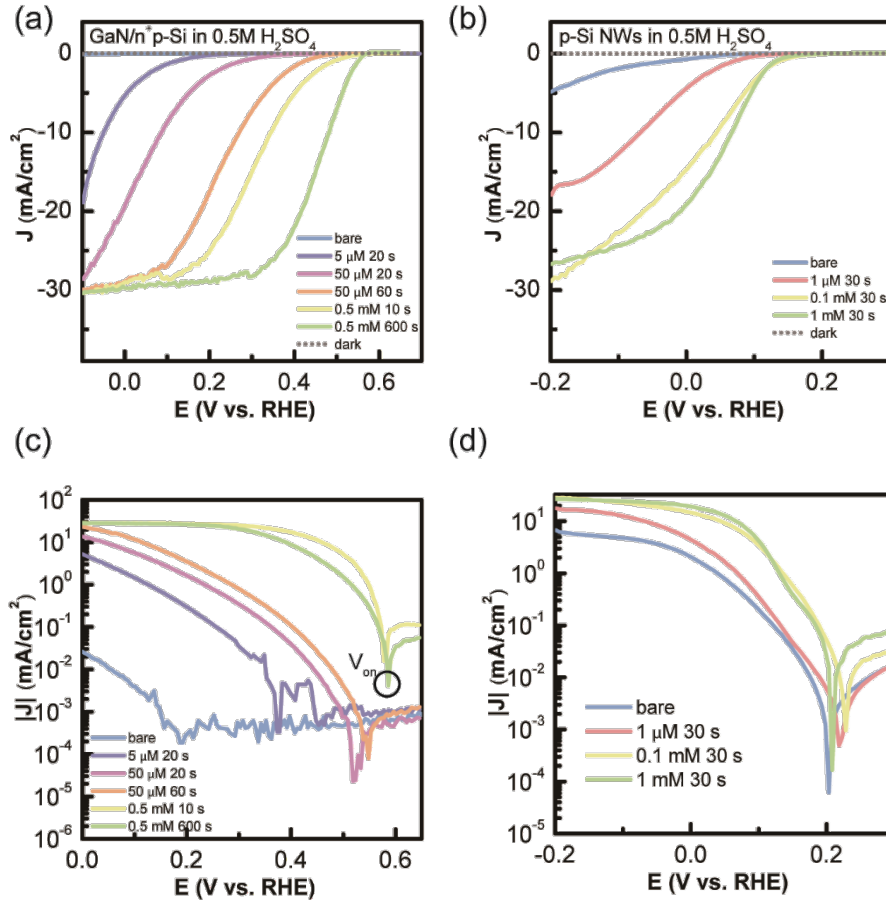


**Figure 4.2** J-V curves of (a) GaN/n<sup>+</sup>p-Si and (b) p-Si NWs under different H<sub>2</sub>PtCl<sub>6</sub> concentrations and deposition times. Testing electrolyte: 0.5 M H<sub>2</sub>SO<sub>4</sub>; Scan rate: 10 mV/s; Light intensity: 100 mW/cm<sup>2</sup>. Representative J-V curves to determine the  $V_{on}$  of GaN/n<sup>+</sup>p-Si (c) and p-Si NWs (d). The absolute values of photocurrent densities were in logarithmic scale. The lowest point in the curve is the corresponded  $V_{on}$ .

For GaN/n<sup>+</sup>p-Si photocathodes, increased  $V_{ph}$  was observed with higher Pt loading amount, with a maximum increase of 170 mV. At the same time, the fill factor increased from 0.067 to 0.534. It has been reported previously by Kemppainen *et al.* that decreasing Pt loading amount on TiO<sub>2</sub>-protected Si buried junction from 1  $\mu\text{g}/\text{cm}^2$  to 10  $\text{ng}/\text{cm}^2$  led to similar  $V_{on}$  but worse  $FF$ , mainly due to the limitation of water reduction kinetics<sup>12</sup>. The change of  $V_{ph}$  observed here, however, is new. It suggests that in addition to improving the water reduction kinetics, which is manifested as better  $FF$  with higher loading, the presence of Pt also affected the interface energetics, leading to the change of  $V_{on}$ 's.

**Table 4.1** Summary of Pt loading amount, turn-on potentials and fill factors for GaN/n<sup>+</sup>p-Si and p-Si NWs under different Pt deposition conditions.

Photocathodes	H <sub>2</sub> PtCl <sub>6</sub> concentration ( $\mu\text{M}$ )	Deposition time (s)	Loading ( $\mu\text{g}/\text{cm}^2$ )	$V_{on}$ (V vs. RHE) <sup>a</sup>	$FF$ <sup>b</sup>
GaN/n <sup>+</sup> p-Si	5	20	$0.010 \pm 0.008$	$0.416 \pm 0.033$	$0.067 \pm 0.011$
	50	20	$0.075 \pm 0.016$	$0.530 \pm 0.020$	$0.077 \pm 0.006$
	50	60	$0.126 \pm 0.033$	$0.571 \pm 0.014$	$0.159 \pm 0.040$
	500	10	$1.72 \pm 0.07$	$0.582 \pm 0.022$	$0.307 \pm 0.130$
	500	600	$4.00 \pm 0.24$	$0.574 \pm 0.010$	$0.534 \pm 0.044$
p-Si NWs	1	30	$0.006 \pm 0.01$	$0.240 \pm 0.015$	$0.086 \pm 0.007$
	100	30	$0.34 \pm 0.07$	$0.241 \pm 0.013$	$0.135 \pm 0.019$
	1000	30	$3.81 \pm 0.08$	$0.198 \pm 0.009$	$0.174 \pm 0.003$

<sup>a, b</sup>The values are averaged from at least three different photoelectrodes

### 4.3.2 Dependence of interface kinetics and energetics on Pt loading amount

To probe whether the charge transfer kinetics was impacted by the Pt loading amount, the kinetic parameters were quantified using IMPS. The theoretical basis of IMPS and experimental data interpretation have been reported previously<sup>13-15</sup>. Briefly, the IMPS measures the phase shift in the photocurrent under a sinusoidal modulation of the light intensities. With the assumption that the change of light intensity only changes the surface charge concentrations (electron concentration in photocathodes), the reaction rates changes under different light intensity can be used to extract the kinetic parameters such as the charge transfer rate constant ( $k_{\text{tran}}$ ), recombination rate constant ( $k_{\text{rec}}$ ) and transfer efficiency (TE). The data interpretation can be found in Equation (3.1) and (3.2) as well as Figure 4.3.

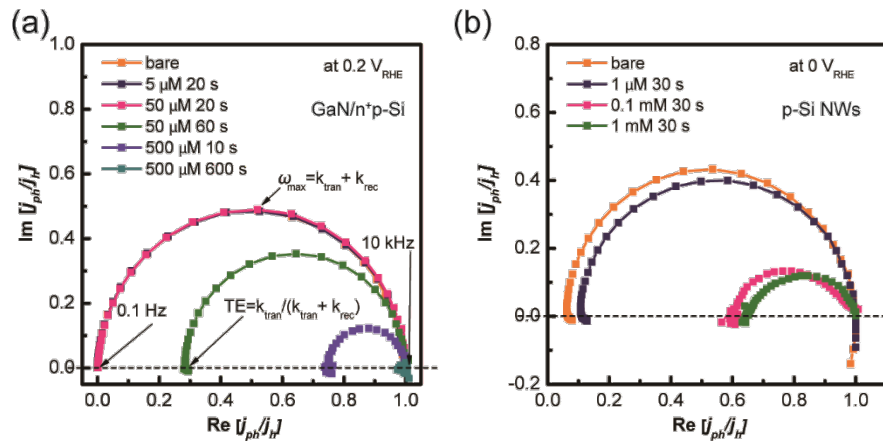


**Figure 4.3** Representative Nyquist plots obtained from IMPS for GaN/n<sup>+</sup>p-Si (a) and p-Si NWs (b) under different H<sub>2</sub>PtCl<sub>6</sub> concentrations and deposition times.

The calculated kinetics parameters including  $k_{\text{tran}}$  and  $k_{\text{rec}}$  at different applied potentials for GaN/n<sup>+</sup>p-Si with different Pt loading amount were shown in Figure 4.4a

and d, where increasing  $k_{\text{tran}}$ 's with higher Pt loading amount was observed. While  $k_{\text{rec}}$  followed an opposite trend, decreasing with more Pt loading, there appeared to be a threshold loading ( $0.1 \mu\text{g}/\text{cm}^2$ ), below which the changes were insignificant. The trend of how  $k_{\text{tran}}$  and  $k_{\text{rec}}$  changed with Pt loading was more clearly observed in Figure 4.4c and f, where the values at 0.2 V were plotted vs. the Pt loading amount. The  $k_{\text{tran}}$  increased by 10,000 times when Pt loading amount increased from  $10^{-2}$  to over  $1 \mu\text{g}/\text{cm}^2$ , whereas  $k_{\text{rec}}$  remained similar with Pt loading amount  $< 0.1 \mu\text{g}/\text{cm}^2$  but started to decrease dramatically with higher Pt loading. The values at other applied potentials more negative than  $V_{\text{on}}$  shared a similar trend. As reported by Thorne *et al.* previously, using IMPS to study complex systems such as catalysts/GaN/n<sup>+</sup>p-Si faces challenges<sup>15</sup>. However, since the time scales of the different processes in different parts of the system are well separated, we interpret the IMPS data as mainly revealing the kinetics at the Si/GaN interface. It is noted that due to unfavorable alignment between the valence band maximums ( $E_{\text{VB}}$ ) between Si and GaN, holes are unlikely to reach the GaN|H<sub>2</sub>O interface. As such, the influence by surface states on GaN to the charge behaviors is considered to be minimum. Taken as a whole, the increase of  $k_{\text{tran}}$  with higher Pt loading amount is likely a result of faster water reduction kinetics, which leads to more facile charge transfer from the photoactive component (Si) to the surface, through the GaN protection layer. Similarly, increased Pt loading reduces electrons trapped at the Si/GaN interface, minimizing recombination as measured by lower  $k_{\text{rec}}$ . In a way, Pt catalysts may be regarded as a storage medium to facilitate electron transfer from GaN to the electrolyte. More details of this understanding and how it can be used to explain the experimental observations will be discussed next.

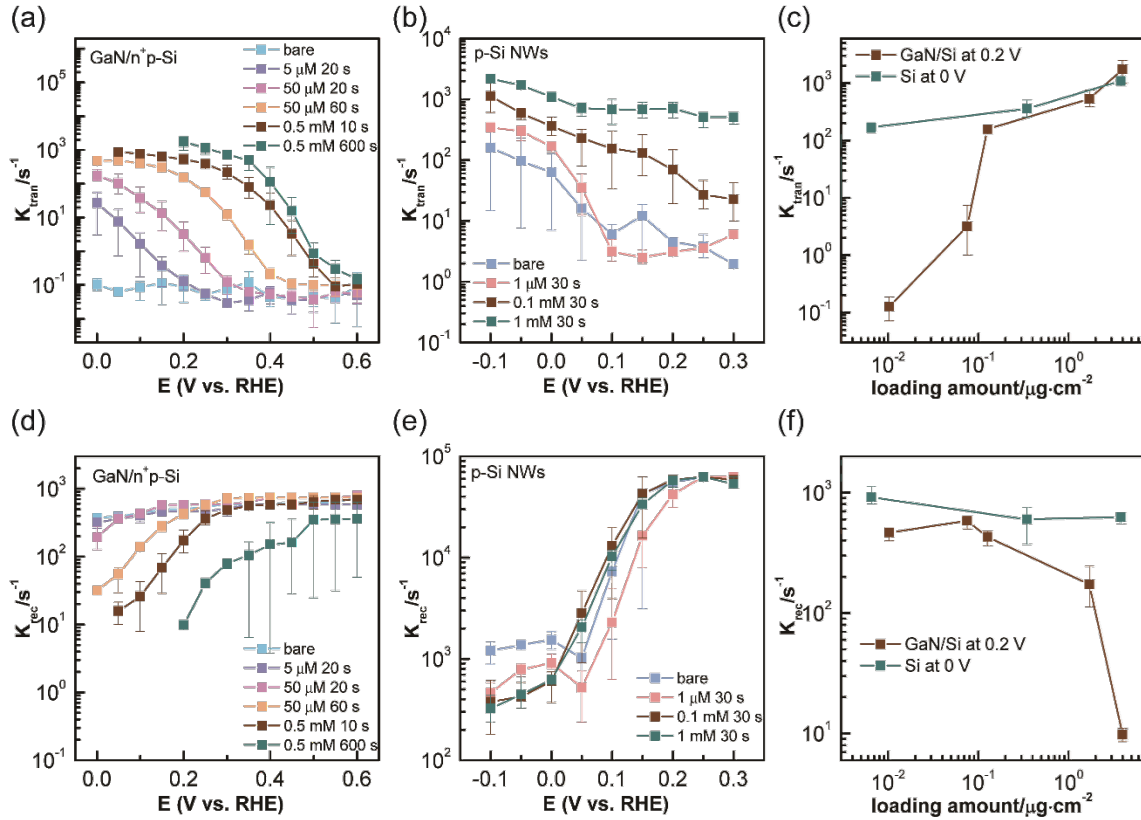


**Figure 4.4** The calculated kinetic parameters including  $k_{\text{tran}}$  and  $k_{\text{rec}}$  from the IMPS Nyquist plots for GaN/n<sup>+</sup>p-Si (a, d) and p-Si NWs (b, e) with different Pt loading amount. The concentration of H<sub>2</sub>PtCl<sub>6</sub> and deposition time for Pt were described in the figure legends. The  $k_{\text{tran}}$  (c) and  $k_{\text{rec}}$  (f) versus Pt loading amount for GaN/n<sup>+</sup>p-Si at 0.2 V and p-Si NWs at 0 V.

While how the Pt loading amount affects the kinetics was indeed expected, the dependence of  $V_{\text{ph}}$  on the loading amount was new and surprising. It implies that the catalyst loading actually also impacts the surface energetics of a buried junction, through the GaN protection layer. To further test this understanding, open-circuit potential (OCP) measurements under dark and light were carried out. The premise of these experiments was that the measured OCPs report the Fermi (or quasi-Fermi) levels of the photoelectrodes under equilibrium (or quasi-equilibrium) conditions. Under ideal conditions, the dark OCP should be at the water reduction potential, whereas the light

OCP should be close to the flat-band potential ( $V_{fb}$ ) of the photoelectrode due to band flattening effect by photogenerated charges. The difference between them reports the  $V_{ph}$ . In order to measure the OCPs accurately,  $H_2$  was continuously bubbled to maintain the reversible HER at or near the standard conditions, which has been proven essential by previous reports<sup>16</sup> and this work (Figure 4.5d). The OCPs under dark and light conditions for GaN/n<sup>+</sup>p-Si with different Pt loading amount were shown in Figure 4.5a. That the light OCPs were similar for different samples were expected because they report the  $V_{fb}$  of the Si substrate, which was identical. The dark OCPs, however, decreased dramatically from 0.55 V to 0 V when the loading was changed from 0.01 to 4  $\mu\text{g}/\text{cm}^2$ , with an obvious change at the loading density of 0.1  $\mu\text{g}/\text{cm}^2$  (Figure 4.5c). The results strongly suggest that at no or low Pt loading ( $<0.1 \mu\text{g}/\text{cm}^2$ ), the photoelectrode would be in equilibrium with an electronic potential away from the reversible HER potential (as shown in the inset of Figure 4.5a). Most likely, the electronic potential indicates the existence of interface states between Si and GaN. The addition of Pt competes with the electronic states in receiving electrons, effectively reducing the influence on the buried junction energetics by these interface electronic states. As a result, a greater degree of band bending was achieved, leading to increased  $V_{ph}$ . It should be noted that cautions must be taken when one attempts to quantitatively compare the data obtained here and those by LSV (Figure 4.2). This is because the data were obtained under different conditions. While OCP measurements were conducted under equilibrium conditions with no current flowing, the LSV experiments were performed under steady-state conditions. More studies would be needed to fully make sense of the difference. Notwithstanding, the trends observed in these two different measurements are qualitatively consistent.

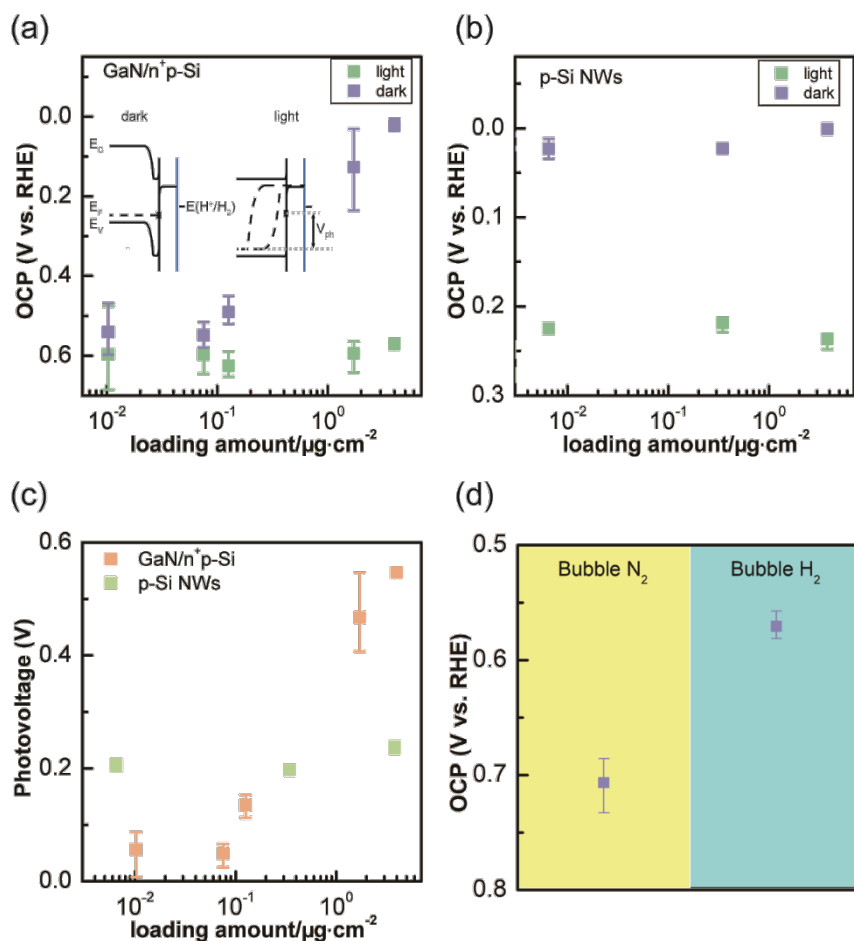


**Figure 4.5** The dark and light OCPs of GaN/n<sup>+</sup>p-Si (a) and p-Si NWs (b) with different Pt loading amount. (c) The photovoltages of GaN/n<sup>+</sup>p-Si and p-Si NWs with different Pt loading amount. The inset band diagrams in (a) showed the equilibrium conditions under dark and light without Pt. (d) The difference between light open-circuit potentials (OCP) when the testing electrolyte was bubbled with N<sub>2</sub> or H<sub>2</sub>. The photocathodes were GaN/n<sup>+</sup>p-Si with the Pt deposited from 0.5 mM H<sub>2</sub>PtCl<sub>6</sub> for 600 s. When the electrolyte was bubbled with N<sub>2</sub>, the obtained OCP was much more positive than  $V_{\text{on}}$ . When the electrolyte was bubbled with H<sub>2</sub>, the obtained OCP was close to  $V_{\text{on}}$ .

### 4.3.3 Discussions of the photoelectrode|electrolyte interface in a PEC system

Under ideal conditions, in a photoelectrode consisting of buried junctions, the  $V_{\text{ph}}$  should be defined by the difference of the Fermi levels on each side of the junction<sup>17</sup>. In a conventional solid-state device, the Fermi levels tend to be well-defined on both sides. In

a PEC device, however, the side in contact with the electrolyte is often difficult to describe or study. In model systems where a redox system featuring fast charge transfer kinetics with the photoelectrode is present, the Fermi level of the photoelectrode on the electrolyte side is expected to equilibrate with the redox potential of this redox system<sup>18</sup>. In practical systems where the redox system is less well defined, such as water reduction or oxidation reactions that involve multiple steps whose charge transfer kinetics is often sluggish, what the equilibrium potential is can be extremely difficult to determine. Sometimes, the addition of an effective catalyst could partially solve the problem, with the catalyst serving as a charge storage medium so as to help define the equilibrium potentials of the electrolyte<sup>19-21</sup>. The addition of protection layers, which are often necessary, however, further complicates the understanding of the interface greatly. New research questions emerge. For instance, *how does the electrolyte (with or without effective catalysts) affect the photoelectrode through the protection layer?* It has been shown previously that the existence of effective catalysts may be critical. For example, Hu *et al.* reported that Ni catalysts were essential for the amorphous-TiO<sub>2</sub>-protected photoanodes with buried junctions<sup>22</sup>. The critical role played by the catalyst is understood as being to effectively extract charges from the buried junction; otherwise electronic states between the buried junction and the protection layer or within or on the protection layer would dominate the energetics of the photoelectrode. This understanding is schematically illustrated in Figure 4.6. An important premise of this understanding is that non-ideal factors would always create electronic states at the various parts of an integrated complex system<sup>20</sup>. One way around the caveat could be to form a truly buried junction, complete with metallic contacts on both sides. That is, a metallic contact with a

well-defined, desired workfunction introduced between the photoelectrode and the protection layer may help better define the  $V_{ph}$  of the buried junction<sup>23</sup>. In such a case, it would be expected the energetics of the system to be less sensitive to the catalyst loading. Nevertheless, such a system would introduce new concerns. For example, how is it different from a photovoltaic plus electrolyzer configuration, in which case cost of fabrication would become an overwhelming concern?

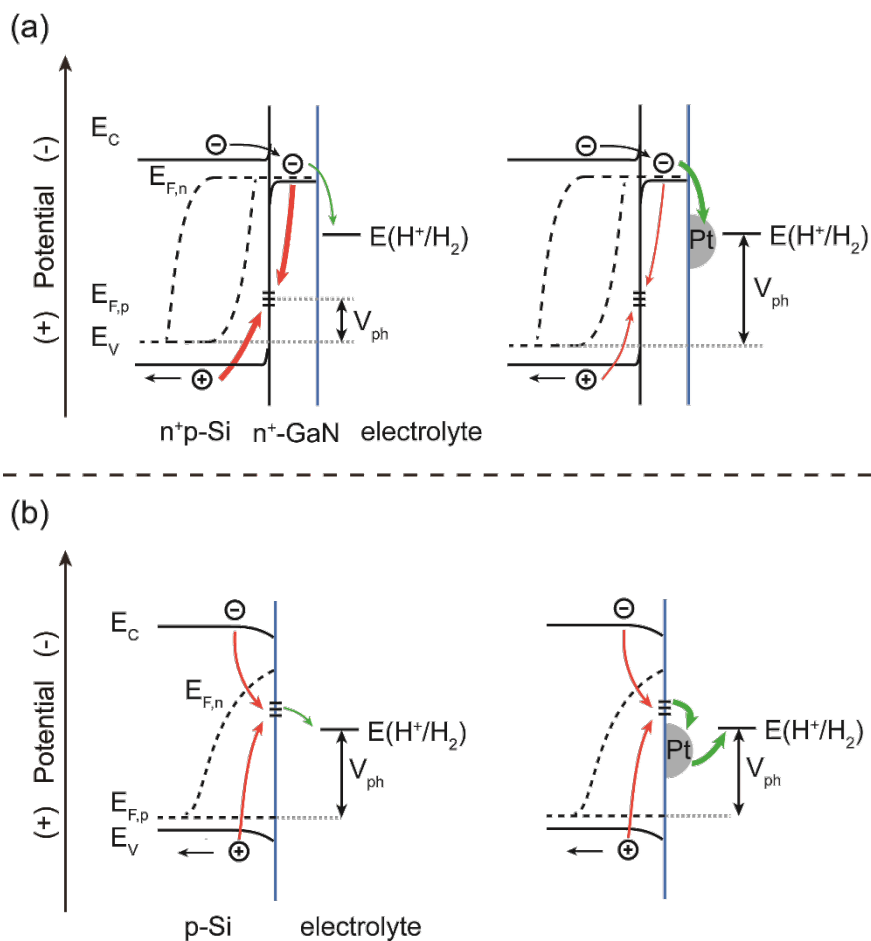


**Figure 4.6** Schematics showing how the addition of Pt affected the charge transfer kinetics and surface energetics for GaN/n<sup>+</sup>p-Si (a) and p-Si NWs (b). The green arrows represent the forward charge transfer pathway and the red arrows represent the charge recombination. The weights of the arrows represent the relative rates of these processes.

#### 4.3.4 Control experiments on Si photocathode without GaN

To further verify the influence of Pt loading amount on the interface kinetics and energetics when a protection layer was present, p-Si NWs without GaN were utilized as control samples. An ideal control sample for this portion of our study should be planar  $n^+p$ -Si sample without GaN. However, attempts to obtain stable operations during catalyst deposition on these samples failed. Similar to the  $n^+p$ -Si sample, p-Si NWs were not stable under PEC Pt deposition, but they permitted Pt deposition by an electroless procedure. As shown in Figure 4.7, Pt NPs (20 to 120 nm) were deposited on the surface of Si NWs. The Pt loading amount on p-Si NWs was controlled within 3 orders of magnitude when the  $H_2PtCl_6$  concentrations increased 1000-fold (Figure 4.11). Compared with GaN/ $n^+p$ -Si, p-Si NWs showed similar  $V_{on}$  with increased Pt loading amount, and only the  $FF$  was improved (Figure 4.2b and Table 4.1). IMPS and OCP measurements were carried out to quantify the interface kinetics and energetics. As shown in Figure 4.4, higher Pt loading amount resulted in increased  $k_{tran}$ . However, the  $k_{rec}$  remained within the same order of magnitude even though the Pt loading amount has been changed by 100 times. The OCP measurements under different Pt loading amount indicated that for p-Si NWs the  $V_{ph}$  remained similar (Figure 4.5).

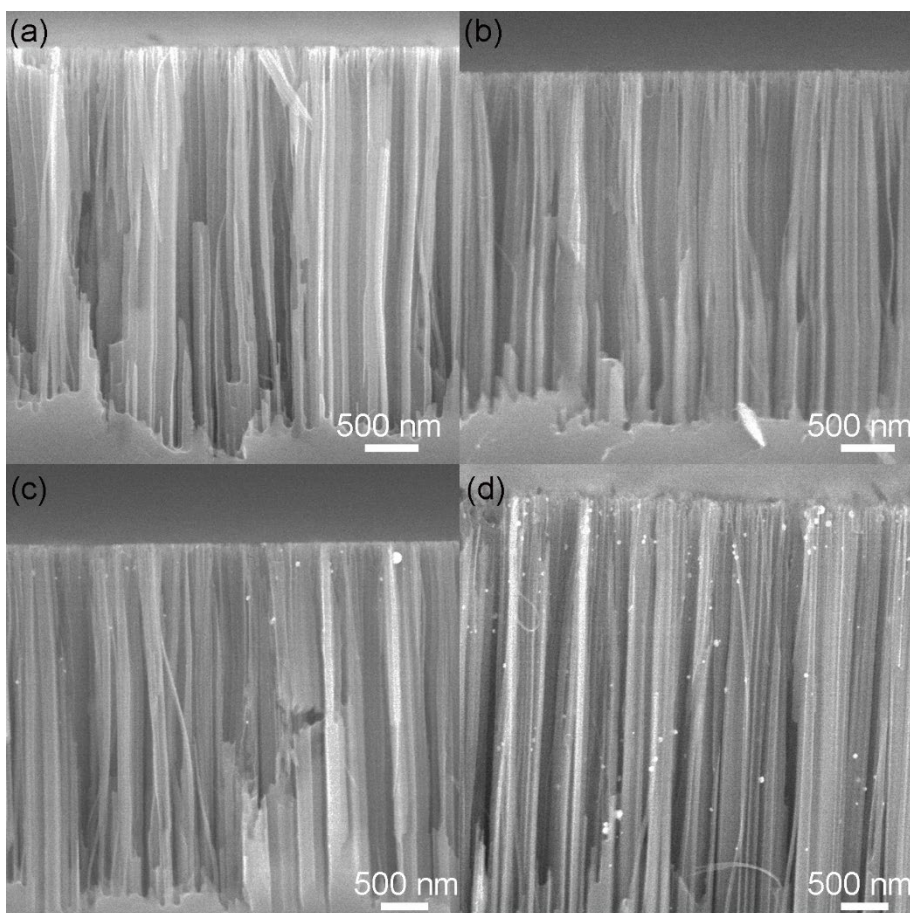


**Figure 4.7** The SEM images of Si nanowires with different Pt deposition conditions. (a) bare; (b) 1  $\mu\text{M}$   $\text{H}_2\text{PtCl}_6$  for 30 s; (c) 0.1 mM  $\text{H}_2\text{PtCl}_6$  for 30 s; (d) 1 mM  $\text{H}_2\text{PtCl}_6$  for 30 s.

For p-Si NWs in solutions, it featured Si/H<sub>2</sub>O, Si/Pt and Pt/H<sub>2</sub>O interfaces. Since Pt was dispersed as nanoparticles on the Si surface and most of the Si surface was still in contact with the electrolyte, it was likely that the Si/H<sub>2</sub>O interface dominated the interface energetics, as supported by the OCP results. Therefore, charge recombination was likely to happen at the electronic states at the Si/H<sub>2</sub>O interface. This was consistent with the observation that similar  $k_{\text{rec}}$  was measured for p-Si NWs even with different Pt loading amount. The improved performance for p-Si NWs after Pt deposition was mainly due to enhanced water reduction kinetics, as evidenced by the increased  $k_{\text{tran}}$  with higher Pt loading amount. The charge transfer process on p-Si NWs with different Pt loading

was summarized in Figure 4.6b. The contrast between the control samples and that with GaN protection highlights the importance to understand the details at the photoelectrode|electrolyte interface. While the protection layer is expected to improve the performance of the buried junction, non-ideal factors still introduce significant electronic states, whose influence cannot be ignored in practical systems. This is where co-catalyst could play critical roles to further improve the system, beyond the simple expectations of faster kinetics.

#### 4.4 SUMMARY

In summary, the PEC performance of two typical Si-based photocathodes with different Pt loading amount was compared. One was a Si buried junction with GaN as the protection layer, and the other one was p-Si NWs without the buried junction or the protection layer. The surface kinetics and energetics were systematically investigated by methods such as IMPS and OCP. It was found that the addition of Pt affected both the interfacial kinetics and energetics for GaN/n<sup>+</sup>p-Si. That the energetics of a photoelectrode with buried junctions could be influenced by co-catalysts beyond the protection layer is new and significant. Future efforts should be guided to further optimize the photoelectrode|protection layer, as well as the co-catalysts, in an integrated fashion. By contrast, only surface kinetics was influenced for bare photoelectrodes (i.e., p-Si NWs) without protection layer, and this is because the interface energetics is already dominated by the semiconductor|electrolyte interface. Such a system (without buried junction and protection layer) is far more difficult to optimize for practical applications.

## 4.5 REFERENCE

1. Y. He and D. Wang, *Chem*, 2018, **4**, 405-408.
2. Y. He, T. Hamann and D. Wang, *Chem. Soc. Rev.*, 2019, **48**, 2182-2215.
3. S. Vanka, E. Arca, S. Cheng, K. Sun, G. A. Botton, G. Teeter and Z. Mi, *Nano Lett.*, 2018, **18**, 6530-6537.
4. S. Fan, B. AlOtaibi, S. Y. Woo, Y. Wang, G. A. Botton and Z. Mi, *Nano Lett.*, 2015, **15**, 2721-2726.
5. Y. Wang, S. Fan, B. AlOtaibi, Y. Wang, L. Li and Z. Mi, *Chemistry - A European Journal*, 2016, **22**, 8809-8813.
6. Q. Cheng, W. Fan, Y. He, P. Ma, S. Vanka, S. Fan, Z. Mi and D. Wang, *Adv. Mater.*, 2017, **29**, 1700312.
7. S. Chu, P. Ou, P. Ghamari, S. Vanka, B. Zhou, I. Shih, J. Song and Z. Mi, *J. Am. Chem. Soc.*, 2018, **140**, 7869-7877.
8. G. Yuan, K. Aruda, S. Zhou, A. Levine, J. Xie and D. Wang, *Angew. Chem. Int. Ed.*, 2011, **50**, 2334-2338.
9. R. Liu, G. Yuan, C. L. Joe, T. E. Lightburn, K. L. Tan and D. Wang, *Angew. Chem. Int. Ed.*, 2012, **51**, 6709-6712.
10. R. Liu, C. Stephani, J. J. Han, K. L. Tan and D. Wang, *Angew. Chem. Int. Ed.*, 2013, **52**, 4225-4228.
11. P. Dai, J. Xie, M. T. Mayer, X. Yang, J. Zhan and D. Wang, *Angew. Chem. Int. Ed.*, 2013, **52**, 11119-11123.
12. E. Kemppainen, A. Bodin, B. Sebok, T. Pedersen, B. Seger, B. Mei, D. Bae, P. C. K. Vesborg, J. Halme, O. Hansen, P. D. Lund and I. Chorkendorff, *Energy Environ. Sci.*, 2015, **8**, 2991-2999.
13. E. A. Ponomarev and L. M. Peter, *J. Electroanal. Chem.*, 1995, **396**, 219-226.
14. L. M. Peter, E. A. Ponomarev and D. J. Fermín, *J. Electroanal. Chem.*, 1997, **427**, 79-96.
15. J. E. Thorne, Y. Zhao, D. He, S. Fan, S. Vanka, Z. Mi and D. Wang, *Phys. Chem. Chem. Phys.*, 2017, **19**, 29653-29659.
16. P. Dai, W. Li, J. Xie, Y. He, J. Thorne, G. McMahon, J. Zhan and D. Wang, *Angew. Chem. Int. Ed.*, 2014, **53**, 13493-13497.
17. A. C. Nielander, M. R. Shaner, K. M. Papadantonakis, S. A. Francis and N. S. Lewis, *Energy Environ. Sci.*, 2015, **8**, 16-25.
18. N. S. Lewis, *Inorg. Chem.*, 2005, **44**, 6900-6911.
19. G. Liu, J. Shi, F. Zhang, Z. Chen, J. Han, C. Ding, S. Chen, Z. Wang, H. Han and C. Li, *Angew. Chem. Int. Ed.*, 2014, **53**, 7295-7299.
20. C. Ding, J. Shi, Z. Wang and C. Li, *ACS Catal.*, 2017, **7**, 675-688.
21. C. Du, M. Zhang, J.-W. Jang, Y. Liu, G.-Y. Liu and D. Wang, *J. Phys. Chem. C*, 2014, **118**, 17054-17059.
22. S. Hu, M. R. Shaner, J. A. Beardslee, M. Lichterman, B. S. Brunschwig and N. S. Lewis, *Science*, 2014, **344**, 1005-1009.
23. D. Kang, J. L. Young, H. Lim, W. E. Klein, H. Chen, Y. Xi, B. Gai, T. G. Deutsch and J. Yoon, *Nat. Energy*, 2017, **2**, 17043.

Chapter 4 is adapted with permission from “Y. He, S. Vanka, T. Gao, D. He, J. Espano, Y. Zhao, Q. Dong, C. Lang, Y. Wang, T. W. Hamann, Z. Mi and D. Wang, *Nano Res.*, 2019, <https://doi.org/10.1007/s12274-019-2346-3>.” Copyright 2019 Springer Nature.

## PUBLICATION LIST

1. **Y. He**, S. Vanka, T. Gao, D. He, J. Espano, Y. Zhao, Q. Dong, C. Lang, Y. Wang, T. Hamann, Z. Mi, D. Wang, "Dependence of Interface Energetics and Kinetics on Catalyst Loading in a Photoelectrochemical System," *Nano Res.* **2019**, <https://doi.org/10.1007/s12274-019-2346-3>
2. **Y. He**, T. Hamann, D. Wang, "Thin Film Photoelectrodes for Solar Water Splitting," *Chem. Soc. Rev.* **2019**, *48*, 2182-2215
3. S. Zhu, Y. Zhao, **Y. He**, D. Wang, "Selectivity of H<sub>2</sub>O<sub>2</sub> and O<sub>2</sub> on Metal Oxide Surfaces by Water Oxidation," *J. Chem. Phys.* **2018**, *150*, 04172
4. W. Li, K. Yang, X. Yao, **Y. He**, Q. Dong, G. Brudvig, V. Batista, D. Wang, "Facet-dependent Kinetics and Energetics of Hematite for Solar Water Oxidation Reactions," *ACS Appl. Mater. Interfaces* **2019**, *11*, 5616-5622
5. **Y. He**, D. Wang, "Toward Practical Solar Hydrogen Production," *Chem* **2018**, *4*, 405-408
6. Q. Dong, X. Yao, Y. Zhao, M. Qi, X. Zhang, H. Sun, **Y. He**, D. Wang, "Cathodically Stable Li-O<sub>2</sub> Battery Operations Using Water-in-Salt Electrolyte," *Chem* **2018**, *4*, 1345-1358

7. **Y. He**, P. Ma, S. Zhu, M. Liu, Q. Dong, J. Espano, X. Yao, D. Wang, "Photo-induced Performance Enhancement of Tantalum Nitride for Solar Water Oxidation," *Joule*, **2017**, *1*, 290-305
8. E. Liu, J. Thorne, **Y. He**, D. Wang, "Understanding Photocharging Effects on Bismuth Vanadate," *ACS Appl. Mater. Interfaces* **2017**, *9*, 22083-22087
9. Q. Cheng, W. Fan, **Y. He**, P. Ma, S. Vanka, Z. Fan, Z. Mi, D. Wang, "Photorechargeable High Voltage Redox Battery Enabled by Ta<sub>3</sub>N<sub>5</sub> and GaN/Si Dual-Photoelectrode," *Adv. Mater.*, **2017**, *29*, 1700312
10. **Y. He**<sup>#</sup>, J. Thorne<sup>#</sup>, C. Wu<sup>#</sup>, P. Ma, C. Du, Q. Dong, J. Guo, D. Wang, "What Limits the Performance of Ta<sub>3</sub>N<sub>5</sub> for Solar Water Splitting?" *Chem* **2016**, *1*, 640-655 (# co-first author)
11. W. Li, D. He, S. Sheehan, **Y. He**, J. Thorne, X. Yao, G. Brudvig, D. Wang, "Comparison of Heterogenized Molecular and Heterogeneous Oxide Catalysts for Photoelectrochemical Water Oxidation," *Energy Environ. Sci* **2016**, *9*, 1794-1802
12. J. Thorne, Y. He, D. Wang, Nanostructured Materials. In: Giménez S., Bisquert J. (eds) Photoelectrochemical Solar Fuel Production. Springer, Cham, 2016, 463-492
13. W. Li, S. Sheehan, D. He, **Y. He**, X. Yao, R. Grimm, G. Brudvig, D. Wang, "Hematite-Based Solar Water Splitting in Acidic Solutions: Functionalization by Mono- and Multi-layers of Ir Oxygen-evolution Catalysts," *Angew. Chem. Int. Ed.* **2015**, *54*, 11428-11432
14. X. Yang, R. Liu, **Y. He**, J. Thorne, Z. Zheng, D. Wang, "Enabling Practical Electrocatalysts-Assisted Photoelectrochemical Water Splitting with Earth Abundant Materials," *Nano Res.* **2015**, *8*, 56-81

15. P. Dai, W. Li, J. Xie, **Y. He**, J. Thorne, G. McMahon, J. Zhan, D. Wang, "Forming Buried Junctions to Enhance Photovoltage by Cuprous Oxide in Aqueous Solutions," *Angew. Chem. Int. Ed.* **2014**, 53, 13493-13497